Title
Applications of Breathing Motion Dynamics Derived from Fast-Helical Free-Breathing CT

Author
Lauria, Michael Vincent

Publication Date
2022

Peer reviewed|Thesis/dissertation

UNIVERSITY OF CALIFORNIA

Los Angeles

Applications of Breathing Motion Dynamics Derived from Fast-Helical Free-Breathing CT

A dissertation submitted in partial satisfaction of the requirements for the degree Doctor of Philosophy in Physics and Biology in Medicine

by

Michael Vincent Lauria

2022

ABSTRACT OF THE DISSERTATION

Applying Breathing Motion Dynamics

Captured by Fast Helical Free-Breathing CT

by

Michael Vincent Lauria

Doctor of Philosophy in Physics and Biology in Medicine

University of California, Los Angeles, 2022

Professor Daniel Abraham Low, Co-Chair

Professor Anand Prasad Santhanam, Co-Chair

Diseases affecting the respiratory system are among the most common and deadliest worldwide. The ability to characterize the patient-specific, physical properties of the respiratory system could improve treatments and interventions that aim to combat these diseases. With the unique capabilities of modern CT technology, we can formulate novel approaches to capture and characterize breathing motion. The development of fast-helical free-breathing CT (FHFBCT), along with the 5DCT motion modeling protocol, have allowed us to acquire CT images with dynamic information, free of the artifacts typically observed in 4DCT approaches. Though this protocol was developed for radiation oncology, its value stems far beyond.

The goal of this dissertation is to use FHFBCT in several applications that provide guidance or improvement to technologies involved in the treatment of patients with respiratory diseases such

as lung cancer and chronic obstructive pulmonary disease (COPD). First, we applied FHFBCT and motion modeling within its primary area of CT simulation for radiotherapy. We studied the use of the respiratory bellows and the entire patient skin surface as respiratory surrogates for CT simulation using FHFBCT data and found that the center abdomen would be a reliable skin surface-based surrogate for diaphragm motion. We then investigated an application of FHFBCT in the radiotherapy workflow outside of CT simulation. We demonstrated the feasibility of using FHFBCT and 5DCT motion modeling in cone-beam CT (CBCT) reconstruction to provide accurate motion compensation. Finally, we proposed the use of dynamic breathing information from FHFBCT beyond radiotherapy altogether, into areas such as surgical planning, pulmonology, and diagnostics. We developed an automatic, triangulation meshing technique for airway segmentations extracted from FHFBCT data to enable computational fluid dynamics (CFD) simulations with free-breathing data. We also calculated ventilation from FHFBCTs and characterized its heterogeneity across lobes of patients with COPD of varying severities. We performed a similar study using elasticity, a measure of tissue stiffness obtained through a CT-based elastography approach, instead of ventilation, to propose an additional biomarker for lung function.

The work in this dissertation provides a demonstration of the unique advantages of breathing dynamics derived from FHFBCT. We hope that this work encourages others to research the studied topics as well as continue to implement FHFBCT and motion modeling to other areas of medicine to improve diagnostics and treatments for patients suffering from respiratory illnesses.

The dissertation of Michael Vincent Lauria is approved.

Michael McNitt-Gray

James Michael Lamb

Anand Prasad Santhanam, Committee Co-Chair

Daniel Abraham Low, Committee Co-Chair

University of California, Los Angeles

2022

To Grandpa Vinny

Table of Contents

LIST OF TABLES

LIST OF FIGURES

LIST OF ABBREVIATIONS

4DCT……....4-Dimensional CT

5DCT……5-Dimensional CT

AP……Anterior-Posterior

BPA……Ball-Pivoting Algorithm

CBCT……Cone-Beam CT

CFD……..Computational Fluid Dynamics

COPD……Chronic Obstructive Pulmonary Disease

CT……Computed Tomography

DVF……..Deformation Vector Field

EFHI……Emphysema and fSAD Heterogeneity Index

EHI……Elasticity Heterogeneity Index

FHFBCT……...Fast-Helical Free Breathing CT

FSI……Fluid Structure Interaction

HU……Hounsfield Unit

IGRT……Image-Guided Radiotherapy

LLL……Left Lower Lobe

LML……...Left Middle Lobe

LUL……Left Upper Lobe

LVRS……Lung Volume Reduction Surgery

MBCT……Model-Based CT

MC……...Marching Cubes

MC-SART……Motion-Compensated SART

PRM……..Parametric Response Mapping

PTK……..Pulmonary Toolkit

RLL……...Right Lower Lobe

RML…….Right Middle Lobe

RPM…….Real-Time Positioning Management

RTK……...Reconstruction Toolkit

RUL……...Right Upper Lobe

RV……..Residual Volume

SART……Simultaneous Algebraic Reconstruction Technique

SI…….Superior-Inferior

SMEIR……Simultaneous Motion Estimation and Image Reconstruction

SPH…….Smoothed Particle Hydrodynamics

TLC……...Total Lung Capacity

VHI…….Ventilation Heterogeneity Index

YM……Young's Modulus

ACKNOWLEDGEMENTS

I would first like to thank my parents, Michael and Michele Lauria, for gifting me with a strong work ethic, curious nature, and motivation to achieve that have helped me reach this point in my scientific career. I would also like to thank my sister, Bianca Lauria, as well as my entire family for their love and support, and the lessons they have each taught me to help me be a better person. I would also like to thank Camila for her unwavering support, patience, and love. She has been by my side every step of this journey. I strive every day to make each of these people proud of me, and that is part of what drove me to earn my PhD.

I would also like to acknowledge my first research advisor, Dr. Allen Garner from Purdue University, for preparing me for this academic milestone. I had not planned on any kind of research career until I met Dr. Garner and the BEEP lab at Purdue. They got me excited about research and gave me my first opportunity to be a researcher, which has defined my career thus far. They were incredibly supportive, motivating, and caring. I would never have been in this position without them, and I am forever thankful to them.

I would like to acknowledge the impact that Bradley Stiehl has had on both my thesis work and my life while at UCLA. He has contributed greatly to my work, and I to his. I was incredibly fortunate to have someone in the same class and lab as me during graduate school, but even more fortunate that it was Brad. He has also been an incredible friend, colleague, and source of support through the past five years. I would also like to thank my other lab mates, Kamal Singhrao, Louise Naumann, Peter Boyle, and Claudia Miller, as well as fellow classmate Caffi Meyer, for their help in completing this dissertation and their friendship which I greatly cherish. I would also like to acknowledge my fellow GPB student, Juan De La Hoz. He was the first person in graduate school

that I made a strong connection with and has been a massive part of my graduate school experience ever since.

I would like to thank my committee members, Dr. Lamb and Dr. McNitt-Gray, for supporting me during my PhD. Both have taught me invaluable skills early on that I was able to carry through my work, and they both have helped me feel confident and motivated to learn. Dr. McNitt-Gray has also been an amazing program director who shows passion, concern, and support for all students in the PBM program. I'd like to thank PBM staff, Reth and Alondra, for all their hard work in supporting us students. I would also like to thank my fellow PBM students for the innumerable fun times spent to help each other work through this experience together.

Finally, I would like to thank and acknowledge my committee co-chairs, Dr. Low and Dr. Santhanam. They have shaped me into the researcher that I am today. Dr. Santhanam has instilled in me a passion for research, an open mind to the many questions we can answer, and a constant drive to achieve more. Dr. Low has consistently been a source of comfort when research became stressful, confidence when I needed to prove myself, and guidance when the answers seemed unclear. I could not thank them enough for helping me reach this stage in my life and my career.

I acknowledge that versions of the following manuscripts, either published, submitted, or in preparation, formed the basis of each chapter of this dissertation.

Chapter 2 is a version of Lauria M, Navaratna R, O'Connell D, Santhanam A, Lee P, Low DA. Investigating internal–external motion correlation using fast helical CT. *Med Phys*. 2021;48(4):1823-31.

Chapter 3 is a version of Lauria M, Singhrao K, Lewis J, O'Connell D, Naumann L, Stiehl B, Santhanam A, Boyle P, Raldow A, Goldin J, Barjaktarevic I, Low D. Feasibility of non-iterative

motion compensated cone-beam CT reconstruction using an a priori model from 5DCT. [Manuscript in Preparation].

Chapter 4 is a version of Lauria M, Singhrao K, Stiehl B, Low D, Goldin J, Barjaktarevic I, Santhanam A. Automatic triangulated mesh generation of pulmonary airways from segmented lung 3DCTs for computational fluid dynamics. *Int J of Comput Assist Radiol Surg*. 2021;1-13.

Chapter 5 is a version of Lauria MV, Stiehl BJ, O'Connell DP, Santhanam AP, McNitt-Gray MF, Naumann, LM, Barjaktarevic IZ, Goldin JG, Raldow AC, Low DA. Lobar heterogeneity of CT-based ventilation in lung cancer patients with and without COPD. [Manuscript in Preparation].

Chapter 6 is a version of Lauria M, Stiehl B, Santhanam A, O'Connell D, Naumann, L, Raldow A, Goldin J, Barjaktarevic I, Low D. A systematic analysis of the regional heterogeneity in tissue elasticity distributions and parametric response mapping in lung cancer patients with COPD. [Manuscript in Preparation].

VITA

Education

M.S. in Physics and Biology in Medicine – Dec. 2019
University of California, Los Angeles, Los Angeles, CA, USA

B.S. in Nuclear Engineering – May 2017
Purdue University, West Lafayette, IN, USA

Certifications

Therapeutic Medical Physics Part I, The American Board of Radiology

Peer-Reviewed Publications

Savjani R, **Lauria M,** Supratik B, Deng J, Yuan Y, Andrearczyk V. Automated tumor segmentation in radiotherapy. *Semin Radiat Oncol*. In Press.

Low D, O'Connell D, **Lauria M**, Stiehl B, Naumann L, Lee P, Hegde J, Barjaktarevic I, Goldin J, Santhanam A. Ventilation measurements using fast-helical free-breathing CT. *Med Phys*. 2021;48(10):6094:6105.

Islam A, Rouhollahi A, **Lauria M,** Santhanam A, Ilegbusi O. Modeling air flow in pathological human airway with patient specific CT-data. *ASME Int Mech Eng Cong and Exposition*. 2021;85598:V005T05A036.

Stiehl B, **Lauria M**, Singhrao K, Goldin J, Barjaktarevic I, Low DA, Santhanam A. Scalable quorum-based deep neural networks with adversarial learning for automated lung lobe segmentation in fast helical free-breathing CTs. *Int J of Comput Assist Radiol Surg*. 2021;1-10.

Lauria M, Singhrao K, Stiehl B, Low D, Goldin J, Barjaktarevic I, Santhanam A. Automatic triangulated mesh generation of pulmonary airways from segmented lung 3DCTs for computational fluid dynamics. *Int J of Comput Assist Radiol Surg*. 2021;1-13.

Lauria M, Navaratna R, O'Connell D, Santhanam A, Lee P, Low DA. Investigating internal–external motion correlation using fast helical CT. *Med Phys*. 2021;48(4):1823-31.

Santhanam AP, Stiehl B, **Lauria M,** Barjaktarevic I, Goldin J, Yanagawa J, Low D. A quantitative prediction of the post-operative lobectomy lung physiology using a GPU-based linear elastic lung biomechanics model and a constrained generative adversarial learning approach. *SPIE 11598, Med Imaging 2021: Image-Guided Proced, Rob Interventions, and Model.* 2021;11598:115980S.

Santhanam AP, Stiehl B, **Lauria M,** Hasse K, Barjaktarevic I, Goldin J, Low DA. An adversarial machine learning framework and biomechanical model-guided approach for computing 3D lung tissue elasticity from end-expiration 3DCT. *Med Phys*. 2021;48(2):667-75.

Stiehl B, **Lauria M,** O'Connell D, Hasse K, Barjaktarevic I, Lee P, Low DA, Santhanam AP. A quantitative analysis of biomechanical lung model consistency using 5DCT datasets. *Med Phys*. 2020;47(11):5555-67.

Santhanam AP, **Lauria M,** Stiehl B, Elliott D, Seshan S, Hsieh S, Cao M, Low D. An adversarial machine-learning-based approach and biomechanically guided validation for improving deformable image registration accuracy between a planning CT and cone-beam CT for adaptive prostate radiotherapy applications. *SPIE 11313, Med Imaging 2020: Image Process.* 2020;11313:113130P.

Selected Conference Presentations

Lauria M, Stiehl B, Naumann L, Santhanam A, O'Connell D, Singhrao K, Goldin J, Barjaktarevic I, Low D. Feasibility of Diagnostic Dose Fast-Helical Free Breathing CT Scan Protocol for Ventilation Measurement. Abstract presented at: AAPM Lung Function Imaging Workshop; August 19, 2021; Virtual.

Lauria M, Stiehl B, Naumann L, Santhanam A, O'Connell D, Singhrao K, Goldin J, Barjaktarevic I, Low D. Feasibility of Diagnostic Dose Fast-Helical Free Breathing CT Scan Protocol for Ventilation Measurement. Abstract presented at: AAPM Annual Meeting; July 25-29, 2021; Virtual.

Lauria M, Stiehl B, Naumann L, Santhanam A, O'Connell D, Singhrao K, Goldin J, Barjaktarevic I, Low D. Characterization of Lobe-Wise Ventilation and Elasticity in Patients with Chronic Obstructive Pulmonary Disease. Abstract presented at: AAPM Annual Meeting; July 25-29, 2021; Virtual.

Lauria M, Singhrao K, Stiehl B, Low D, Goldin J, Barjaktarevic I, Santhanam A. Automatic Triangulated Mesh Generation of Pulmonary Airways from Segmented Lung 3DCTs for Computational Fluid Dynamics. Paper presented at: International Conference on Information Processing in Computer-Assisted Interventions; June 22-23, 2021; Virtual.

Lauria M, Stiehl B, O'Connell D, Hsieh S, Barjaktarevic I, Santhanam A, Low D. 5DCT Reconstruction Accuracy and Elasticity Estimation Performance for Low Dose Fast-Helical Free Breathing CT. Abstract presented at: AAPM Annual Meeting; July 12-16, 2020; Virtual.

Lauria M, Navaratna R, O'Connell D, Lee P, Low D. Investigating Internal-External Motion Correlation Using Fast Helical Free-Breathing CT and Simultaneous Respiratory Bellows. Abstract presented at: AAPM Annual Meeting; July 12-16, 2020; Virtual.

Lauria M, O'Connell D, Agazaryan N, Lewis J, Lamb J, Thomas D, Lee P, Low D. Clinical Introduction of 5DCT Simulation for Lung Cancer. Abstract presented at: AAPM Annual Meeting; July 14-18, 2019; San Antonio, TX.

Professional and Leadership Roles

American Association of Physicists in Medicine – Member – March 2021-Present

UCLA Biosciences Council – Program Representative – September 2019-September 2021

UCLA Physics and Biology in Medicine Student Representative – Ambassador – September 2018-Present

CHAPTER 1: INTRODUCTION TO THE DISSERTATION

1.1 Motivation

The lungs work to oxygenate blood by facilitating the transport of air to and from sites of gas exchange[1]. The lungs reel in oxygen via changes in pressure caused by contraction of the diaphragm. They then expel carbon dioxide during exhalation as the diaphragm relaxes. Both processes are driven by changes in transpulmonary pressure, which has most recently been defined as the pressure difference between the alveolar pressure and the pleural pressure[2]. During inhalation, the diaphragm primarily moves in the inferior direction, causing an increase in volume, and hence a decrease in alveolar pressure that drives air into the lungs[3]. During exhalation the lung volume is larger at the same transpulmonary pressure than during inhalation as the lungs are passively deflated[4]. This cycle involves the work of the diaphragm along with the intercostal muscles, scalene muscles, pressure dynamics, biomechanical factors like tissue elasticity, differences in breathing modes (quiet vs. forced respiration), and other contributing factors[5-8]. These factors culminate to form a complex respiratory system.

Diseases that affect the respiratory system are among the most prevalent diseases worldwide. Lung cancer is a disease that affects 1 in 15 men and 1 in 17 women[9]. It is the second most common form of cancer in men and women and is by far the leading cause of cancer death, accounting for 25% of all cancer deaths. Chronic obstructive pulmonary disease (COPD) includes several pulmonary diseases, all of which have in common that they limit airflow, are progressive, and are not fully reversible[10]. COPD is the fourth leading cause of death in the United States[11] and the third leading cause of death worldwide[12].

The ability to better characterize the physics of the respiratory system could help combat fundamental problems currently faced in medical treatments or procedures and enable better care for patients with diseases like lung cancer or COPD. These procedures include, but are not limited to, radiation therapy[13], lung volume reduction surgery (LVRS)[14], and bronchoscopic lung volume reduction (BLVR)[15]. Each of these could be improved by incorporating known information about patient-specific breathing dynamics into the planning stage. Strong medical imaging capabilities are necessary to enable such developments.

With improvements in computed tomography (CT), we can now use the unique advantages of fast-helical free-breathing CT (FHFBCT) to capture and characterize breathing motion dynamics. The motivation of this work is to take advantage of these capabilities and apply them to several areas of medicine within and beyond radiation oncology. This work will hopefully serve as a starting point for future investigations in each studied application, as well as inspire the use of breathing dynamics in addressing other fundamental problems in medicine.

1.2 Background

At its advent, CT did not offer the vast amount of information that it does today. In 1972, the first CT scanner was introduced by Godfrey Hounsfield[16,17]. This first-generation scanner used a single x-ray tube with pencil beam geometry and a single detector, which were moved synchronously in a linear fashion. This was repeated for a set of projection angles to acquire images. These scanners required 4 to 5 minutes[18] to image a single axial slice, which limited them from providing any measurable breathing information. The next generation of scanners utilized a fan beam geometry with a detector array. Since the detector array was small, the system still needed to be linearly translated as in the first generation. Though the scanning time

was reduced, it was still not sufficient for imaging organs that move out of the imaging plane. Finally, the linear translation of the x-ray tube and detector array was removed with third generation CT scanners as the fan beam angle and detector size were increased enough to cover the entire torso. This development led to the construct of most CT scanners used today, and those employed in this dissertation. A fourth generation of CT scanners kept the fan beam geometry of the x-ray tube but applied a fixed ring of detectors. A schematic of these scanner generations from Buzug, et al. is shown in Figure 1-1.

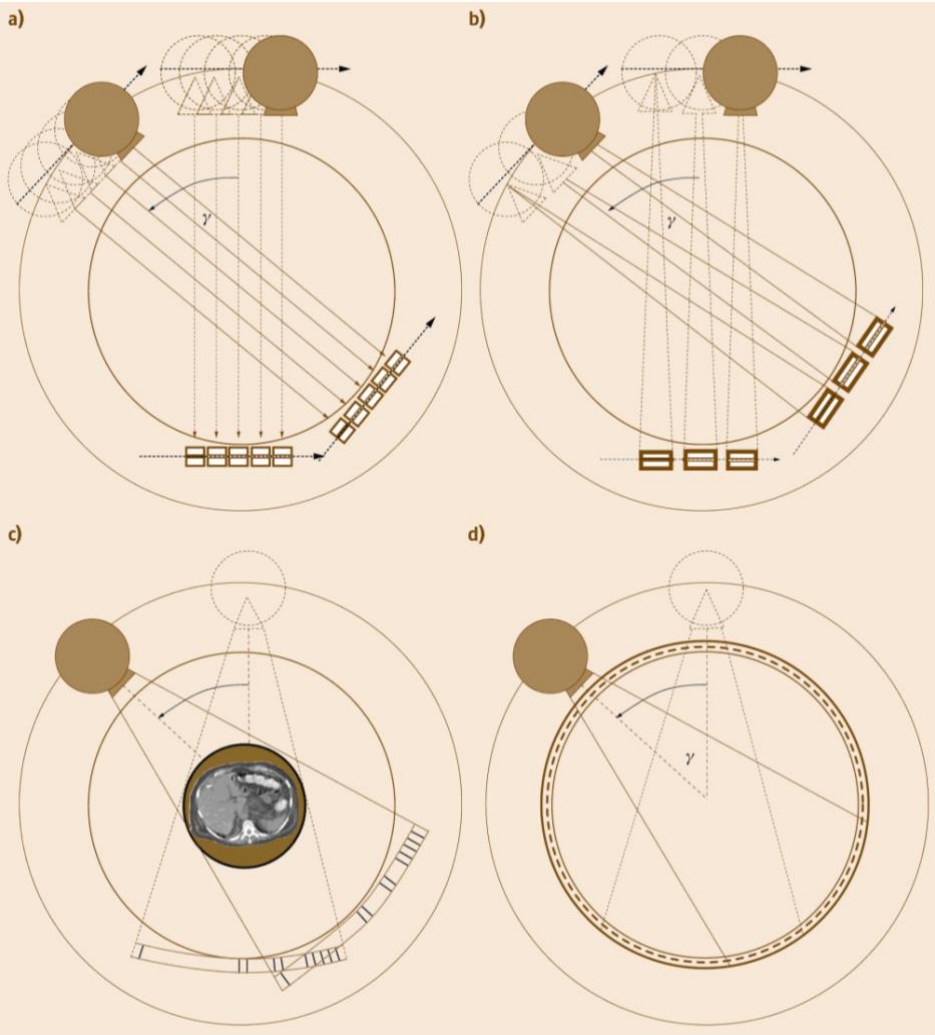

Fig. 1-1: Schematic of CT generations from Buzug, et al.[16] showing (a) first generation CT, (b) second generation CT, (c) third generation CT, and (d) fourth generation CT.

The most important development in CT technology for this work was the introduction of the slip ring, which enabled helical CT, first demonstrated by Kalender in the 1980s[19]. The slip ring transferred electrical energy to the gantry while returning measured data to the computer[19]. With the gantry able to rotate more than 360° without the limitations of electrical cables, the source and detector array of third-generation scanners could rotate continuously and at higher velocities for faster sampling rates. With the combination of helical CT and acquisition during free breathing in the FHFBCT scanning protocol, we can now obtain far more information about the breathing dynamics at play, which can be used to characterize respiratory motion during the scanning session.

Three primary techniques allow us to measure and characterize human breathing to enable the studies in this proposal. Each technique is described below, and Table 1-1 summarizes the relevant aims for each.

A capable imaging technique is required to capture dynamic breathing in human lungs from free-breathing CT. One way to obtain temporal information in CT is with 4DCT, which involves CT acquisition with simultaneous monitoring of patient breathing via a respiratory surrogate so that images or projections can be sorted into breathing phase bins[20]. However, 4DCT can often experience sorting artifacts in the case of irregular breathing[21], such as the artifact shown in the clinical 4DCT from Low et al.[22] in Figure 1-2.

Fig. 1-2: Example of sorting artifacts from clinical 4DCT from Low et al.[22]

The presence of sorting artifacts has been shown to impact the accuracy of functional measurements from CT such as ventilation[23]. Breath-hold images can also be used to calculate biomechanical parameters, but having a single pair of images and deep inspiration limits the ability to measure subtle biomechanics that could be obtained from free, dynamic breathing[24]. Therefore, the technique that serves as the foundation to all proposed studies is FHFBCT. Utilizing the fast-helical scanning protocol, we can acquire data spanning multiple breaths and separate them from the sorting process for accurate measurements and motion characterization[22].

The next technique required to complete this work is model-based CT (MBCT). In our group, we utilize an example of MBCT called the 5DCT motion model. In 2005, Low et al. hypothesized that lung motion could accurately be modeled with five degrees of freedom: 3-dimensional position of the tissues, tidal volume, and airflow[25]. In 2014, another publication described the 5DCT motion model based on these principles with the aim to replace 4DCT with a more robust technique for irregular breathing[26]. The protocol utilized 25 FHFBCTs with

simultaneous monitoring of the breathing amplitude and rate acquired using a respiratory bellows. An average scan was chosen to be the reference scan, to which the other 24 scans were deformably registered to obtain deformation vector fields (DVFs). Voxel-specific motion characterization parameters, α and β, could then be obtained by solving the following motion modeling equation[26].

$$\vec{X}(v, f: \overrightarrow{X_0}) = \overrightarrow{X_0} + \vec{\alpha}(\overrightarrow{X_0})v + \vec{\beta}(\overrightarrow{X_0})f \quad (1\text{-}1)$$

In Equation 1-1, X is the tissue position at amplitude (tidal volume), v, and rate (flow), f, and X_0 is the tissue position at zero tidal volume and flow rate. With these parameters, pseudo-breath-hold images at any user-defined breathing phase could be obtained by deforming the reference scan. Figure 1-3 shows a flowchart of the 5DCT modeling process from Dou, et al.[27]

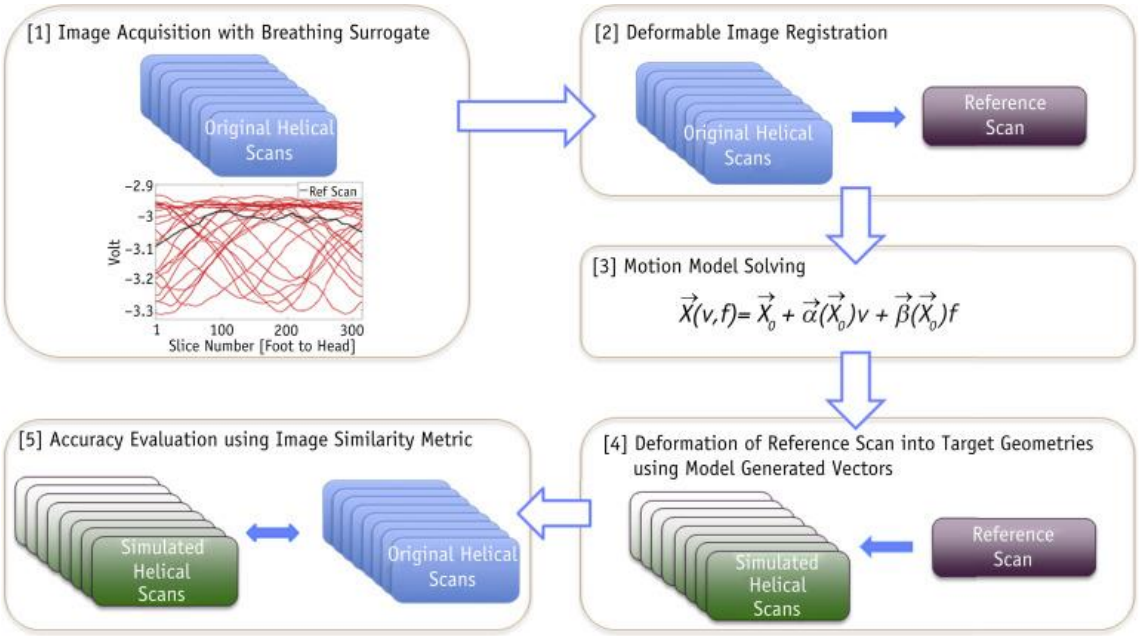

Fig. 1-3: Flowchart of the 5DCT workflow from Dou, et al.[27]

Since the initial publication, much research has been dedicated to integrating 5DCT for clinical use in the radiotherapy workflow during CT simulation[28]. Efforts have included establishing a ground truth-based accuracy analysis[27], evaluating 5DCT against a clinical 4DCT protocol[29,30], investigating FHFBCT scan parameters that eliminate artifacts[31], and

studying other aspects of the imaging or reconstruction processes[32-34]. This well-developed and validated technique for characterizing tissue motion is used in this proposal to enable biomechanical modeling and physiological property measurements.

Finally, registration is the third key technique in the proposed studies because it enables the tracking of motion at the voxel level across different scans. It is therefore at the core of motion characterization. In this proposal, we use two registration techniques to deformably map one image to another. The first is deeds, which uses a multilevel B-spline algorithm and is known to preserve the sliding motion at the lung boundary[35-37]. Deeds has been used in previous studies registering FHFBCT scans and is the standard registration in previous 5DCT studies as well as the 5DCT clinical protocol[27,32]. The other registration technique is pTVreg, which uses isotropic total variation regularization to accurately register sliding interfaces and avoid physically implausible DVFs[38]. This method has been applied specifically when registering larger deformations, such as from end-exhalation images to end-inhalation images[39].

Table 1-1: Summary of relevant chapters for each primary lung dynamics technique

Tool	Relevant Chapters	Description
FHFBCT	2-6	Chapter 2: FHFBCT scans are used to track the diaphragm and skin surface position. Chapter 3: FHFBCT will be used to calculate a prior model to inform CBCT. Chapter 4: Airway segmentations from FHFBCT are meshed using our algorithm. Chapters 5 & 6: FHFBCT scans are used to build 5DCT models to calculate ventilation and elasticity.
5DCT/deeds	3, 5, 6	All Chapters: The 5DCT model is used in each aim to characterize tissue motion and simulate deformations at user-defined breathing phases.
pTVreg	5-6	Chapters 5 & 6: pTVreg is used to register end-exhalation and end-inhalation scans.

1.3 Specific Aims

Breathing induces motion in patient anatomy that complicates imaging and consequently image-derived models, measurements, and treatment planning decisions. There is a need to manage motion in these technologies, and the use of FHFBCT can address this need in several specific applications by utilizing the 5DCT imaging protocol to capture breathing dynamics. Therefore, the overarching objective of this work is to investigate ways that free-breathing dynamics captured by FHFBCT can impact various scientific applications in radiation oncology and beyond. The following specific aims address four applications.

Specific Aim 1 (SA1): Quantify the correlation of surface motion to diaphragm motion to inform surface imaging in CT simulation.

Specific Aim 2 (SA2): Develop an improved free-breathing cone-beam CT (CBCT) workflow for radiotherapy using an *a priori* model.

Specific Aim 3 (SA3): Design a computational fluid dynamics (CFD)-compliant airway meshing algorithm to enable downstream CFD airflow modeling for surgical planning.

Specific Aim 4 (SA4): Characterize the regional and lobar heterogeneity of patients with COPD using parametric response mapping (PRM) and functional, CT-based property calculations including ventilation and elasticity.

Broader Implications: The breathing motion information captured by free-breathing CT scans can enable techniques in daily therapy setup, surgical planning, diagnostics, and more. The work in SA1 can be used to enable more advanced surrogates for internal breathing motion during CT simulation. The work in SA2 can improve CBCT reconstruction to improve the

accuracy of radiotherapy dose delivery and open the door to improved adaptive radiotherapy techniques. The work in SA3 can lead to airflow modeling to plan surgical interventions and simulate surgical outcomes. The work in SA4 can be used to inform surgical planning by highlighting key regional patterns of biomechanical properties in patients with COPD. It could also lead to novel diagnostic approaches to identify high and low functioning lung in diseased patients. This dissertation work serves to advance the scientific approaches to each application through our understanding of human breathing. Altogether, this work will offer a starting point for future researchers to further investigate and apply these concepts in their own research and eventually clinical practices through the methods described in each chapter.

1.4 Overview

Each of Chapters 2-6 address one of the specific aims. These chapters contain versions of manuscripts that are either published, in submission, or in preparation for submission. Chapter 2 describes the work towards SA1 in which we used FHFBCT data in combination with simultaneous respiratory surrogate acquisition to relate the diaphragm motion to the anterior skin surface motion. Chapter 3 includes the work done to address SA2, describing our work to use FHFBCT to inform a respiratory motion model in CBCT. In Chapter 4, we describe our pulmonary airway meshing algorithm pertaining to SA3. Chapter 5 includes the lobe-wise analysis of ventilation in patients with and without COPD to address SA4 using FHFBCT data to characterize the lobe function. Finally, Chapter 6 addresses the regional heterogeneity of elasticity and PRM and discusses their potential in advancing disease indication.

CHAPTER 2: QUANTIFY THE CORRELATION OF SURFACE MOTION TO DIAPHRAGM MOTION TO INFORM SURFACE IMAGING IN CT SIMULATION

Investigating internal-external motion correlation using fast helical CT

A version of this chapter has been published as a manuscript: Med Phys, Vol. 48, No. 4, 2021. doi: 10.1002/mp.14759

2.1 Introduction

Respiratory motion in radiation therapy treatment planning is most commonly managed using 4DCT to characterize the respiratory-induced tumor motion[21,25]. In commercial 4DCT, images or projections[20], depending on the commercial application, are acquired as the respiratory cycle is simultaneously monitored and characterized using a breathing surrogate device. In contrast to the sorting-based method used in commercial protocols, MBCT techniques aim to describe the correspondence between the breathing surrogate signal and internal tissue motion using respiratory motion models[22,40,41]. In both commercial 4DCT and MBCT, it is essential that the breathing surrogate signal is strongly correlated with internal tissue motion[22,41].

There are two different types of breathing surrogates used in radiation therapy – an external surrogate, such as a non-invasive abdominal surrogate[42], or an internal surrogate such as an implanted fiducial marker. Although implanted fiducial markers directly track internal tissue motion[43], they require an invasive procedure[44].

Two techniques exist for an external breathing surrogate to measure breathing motion – point/surface-based and torso circumference-based. The point/surface-based surrogates measure the motion of the torso skin caused by breathing-induced internal tissue displacement[43,45-49]. Circumference-based surrogates are based on the expansion of the

abdomen or chest cross section due to the same tissue displacement[50,51]. The effectiveness of these techniques relies on a strong correlation to the internal anatomy.

Numerous studies have been conducted on internal-external surrogate correlation[43,45-49]. Ionascu et al. measured the correlation between internal and external surrogates: fiducial markers visualized with stereoscopic x-ray fluoroscopy on lung tumors and abdominal surface motion, respectively. They found high correlations between the internal and external surrogate motions[43]. Vedam et al.[46] and Mageras et al.[47] found strong correlations between diaphragm motion, tracked using fluoroscopic movies of the chest to measure diaphragm motion, and skin surface motion, tracked with reflective markers placed on the skin. In both fluoroscopy studies, the only evaluated external surrogate was the abdominal surface motion at a single position on the patient skin surface. Chi et al. examined the relationship of the signal from the real-time positioning management (RPM) system (Varian Medical Systems, Palo Alto, CA) to the internal tumor motion and chest wall motion measured using ciné CT[49]. The RPM system used an infrared reflector block to measure chest or abdomen height, depending on the location of the block. Their study found a good correlation between the RPM block, placed on the abdomen, and the superior-inferior (SI) tumor motion, while a significant phase shift was found between the RPM and tumor motion when the RPM was placed on the chest wall. Due to the employed ciné protocol, the images acquired at a given couch location were acquired over a time span that was approximately equal to one breathing period, and therefore the potential effects of breathing irregularity were not studied.

Some groups have investigated using optical surface imaging as a non-radiographic, noninvasive method of monitoring respiratory motion during radiotherapy[52]. For example, Schaerer et al. demonstrated the ability to characterize breathing motion using surface imaging

with the AlignRT system (VisionRT Ltd, London, UK) and a deformable registration algorithm by showing accurate registration of surface image points across three different breathing phases: maximum inhale, maximum exhale, and an arbitrary intermediate phase[53]. The group highlighted the potential extension of their method with internal/external correlation models to improve motion management in radiation therapy, and thus laid some initial framework for this line of research, demonstrating that surface motion is a feasible surrogate. Li et al. used optical surface imaging to measure tidal volume, calculate airflow, and estimate breathing patterns[54]. These measurements were extracted from surface tracking and describe general changes of internal anatomy, but the direct relationship between internal and external motion was not directly investigated. The ability to relate the external surface detected to the actual internal motion would offer an additional advantage to support use of this technology. 4DMR has been used to study respiratory motion relationships, but existing studies have focused on direct internal lung tissue motion imaging and characterization[55-57]. Our work focused on testing the skin surface as a surrogate. Direct MR-based measurements provide insights as to internal tissue motion but have not aided in the characterization of external breathing surrogates.

Lu et al. compared breathing metrics, including tidal volume from spirometry and abdomen height, using internal air content to evaluate them[58]. Their work found both metrics to correlate well, but results for the abdomen height, which was measured with a video of a block placed on the patient, were less precise than the tidal volume. This study provided important insights as to the relative accuracy of different types of surrogates but did not examine multiple locations on the chest and abdomen.

One goal of this work was to use the dynamic data acquired with FHFBCT to compare the bellows-based surrogate to the diaphragm dome, selected as a reference surrogate, because the diaphragm is one of the muscles driving breathing. The relationship between the bellows signal and the diaphragm was used to evaluate how well the bellows acted as a continuous representation of the diaphragm position. The bellows was then used to accomplish our second goal, which was to use the same reference surrogate to evaluate the use of different abdomen and chest surface positions as surrogates, for example if employing surface imaging. This work was intended to provide guidance for future surrogate design and provide a benchmark for the bellows-based approach[59].

2.2 Methods

2.2.1 Image Acquisition

Fourteen lung cancer patients were imaged under an IRB-approved study using a FHFBCT protocol. For each patient, we acquired 25 FHFBCTs through an IRB approved study, also used in previous studies[26,59]. Three multi detector row CT scanners were used in this study (Definition Flash, Biograph 64, Definition AS 64; Siemens Healthcare, Erlangen, Germany). The scanner-specific parameters are summarized in Table 2-1. All scanners used 120 kVp and 40 mAs. All images were also acquired with a field of view of 500 mm, in-plane pixel resolution of 0.976 x 0.976 mm^2, and slice thickness of 1.0 mm, and we resampled the images to 1 mm isotropic voxels.

Table 2-1: Summary of scanners used to acquire patient data

Scanner	Rotation Period (s)	Pitch	Irradiation Time (s)	Table Speed (mm/s)	Scan Time (s)	Delay between Scans (s)	Total Acquisition Time (s)
Definition Flash	0.285	1.2	0.238	161.4	2.5	2	140
Biograph 64	0.330	1.5	0.220	87.02	4.5	6	275

Definition AS 64	0.330	1.5	0.220	87.02	4.5	3	200

Since neither images nor projections were sorted such as in 4DCT, sorting artifacts were absent. Motion artifacts such as blurring were still present but were reduced because of the relatively fast scanning protocol employed.

A pneumatic bellows (Lafayette Instrument Company, Lafayette, IN) wrapped around the abdomen was used as a noninvasive, external, circumference-based surrogate. The bellows signal was acquired as part of the 5DCT protocol, but neither 4DCT nor 5DCT reconstructions were performed for this study. The bellows was only used to monitor the breathing amplitude during scan acquisition. The bellows was positioned at the abdomen since the abdomen typically expanded sufficiently to provide a useful surrogate signal. The air pressure inside the bellows changed in response to abdominal distention. A pressure transducer converted the change in pressure to a voltage amplitude. The bellows voltage signal was recorded before and during the scans, sampled at 100 Hz. Since scan acquisition required about 2.5–4.5 s, the entire imaged volume could not be assigned a single amplitude. Instead, the amplitudes were assigned per slice. To convert the amplitudes from voltages to a more meaningful quantity, they were normalized using a histogram of the amplitudes as measured between the beginning and end of CT acquisition. End exhalation and inhalation were defined to be the 5th and 95th percentile amplitudes, respectively.

2.2.2 Diaphragm Motion vs. Bellows Signal

The diaphragm position was selected as the reference surrogate and characterized by the superior diaphragm dome position and its SI motion. The nature of the FHFBCT protocol

imaged the diaphragm dome in 25 distinct locations corresponding to the 25 CT scans, and the dome position was quantified at each scan. The measured diaphragm positions were correlated with the bellows signals acquired at those times, and the relationship was used to determine the precision with which the bellows signal reflected the diaphragm position.

In each scan dataset, the lungs were isolated using semi-automatic region-growing segmentation (MIM Vista; MIM Software, Cleveland OH). To obtain the locations of the diaphragm, and thus its motion, for each lung, the most superior point on the diaphragm dome was found on all 25 scans. For increased accuracy, the precise location of the diaphragm point was calculated with sub-voxel precision.

A method similar to Low, et al.[33] was used to precisely measure the craniocaudal position of this diaphragm point in the first and subsequent scans. For each point, the craniocaudal Hounsfield unit (HU) profile was extracted and fit to a sigmoid, representing the change in HU value across the diaphragm–lung boundary. The inflection point characterized the position of the boundary for that scan. Because nonparenchymal tissue often existed directly superior to the diaphragm, a 7 × 7 transverse plane of voxels surrounding the most superior point on the diaphragm was selected. HU profiles that passed directly between the diaphragm and parenchymal tissue were identified by selecting the profiles with the maximum difference in the asymptotic profile fit values, since a larger asymptotic difference would indicate less interference on nonparenchymal tissue. The profile with the largest maximum asymptotic difference was used to define the diaphragm position surrogate. This position was found to be stable in the anteroposterior (AP) and lateral directions. For example, for one patient, the average motion in the AP direction at the selected diaphragm point was −0.14 mm, and the

average lateral motion was 0.60 mm, compared to an average 16 mm of motion in the craniocaudal direction.

The craniocaudal diaphragm surface position was recorded for each of the 25 scans. The corresponding abdominal bellows signal measured at the time of the corresponding slice image acquisition was also recorded for each of the 25 scans. The relationship between the bellows signal and diaphragm surface position was assessed by measuring the root-mean-square of the residual errors in a linear fit of the two quantities, normalized to the 5th to 95th percentile breathing amplitude range. We termed this measurement the residual error, which is reported as a percent of the 5th to 95th percentile breathing amplitude range.

The abdominal bellows signal had a slow linear drift.[26] Without correcting for drift, the range of bellows amplitudes would change during the scanning procedure, yielding incorrect amplitude measurements. To correct the signal for this drift, the correlation between the diaphragm position and the corresponding bellows signal was calculated. A linear drift correction was applied and optimized to maximize the correlation coefficient between the diaphragm surface position and the drift-corrected bellows signal.

The bellows signal was synchronized to the CT scans using the CT-on signal acquired from the scanner during scan acquisition. The relative system times between the two computers were determined to within 1s. To improve synchronization accuracy, the residual time shift was determined by again maximizing the correlation coefficient between the diaphragm position and the bellows signal. Since both the left and right diaphragms could be used to optimize the time shift, we performed the optimization with each and used the average time for subsequent analysis.

To determine how well the bellows surrogate signal reflected the diaphragm motion, the measured diaphragm positions were compared against the corrected bellows signal with a linear fit. The residual error was used to evaluate the precision of the bellows as a surrogate.

2.2.3 Patient Skin Surface Position vs Bellows Signal

Because the bellows was our only continuously measured quantity, we used it to correlate against the skin surface positions. With the measured precision of the bellows-to-diaphragm position, we were able to determine the precision with which each skin surface patch could have been used as a surrogate, at least within the 25 measurements at each skin patch.

The drift-corrected and percentile-normalized bellows signal was subsequently used as the time-dependent amplitude signal. Having demonstrated that the bellows was an accurate surrogate for the diaphragm motion, the skin surface was then related to the bellows to study the correlation of external skin motion to internal motion. A full-body mask was created by segmenting the patient skin. The skin surface positions were determined by fitting each AP voxel line to a sigmoid and defining the skin as the sigmoid inflection point, as in the diaphragm detection approach.

The patient skin surface was divided into a series of abutting 10 × 10 voxel patches. Since the acquisition time between neighboring slices differed by only 5 ms, the time at the middle slice (termed effective time) was used to determine the bellows-based amplitude, and the skin heights were assumed to be simultaneously imaged. Therefore, the average AP point positions of the patch were compared against the simultaneously measured abdominal bellows signal for the effective time of the patch, and the residual error of the linear fit between skin motion and bellows signal was used to define the precision of using that particular skin patch as a motion surrogate. This linear fit was called the skin-bellows fit. Figure 2-1 summarizes our approach,

ultimately assessing the relationship of the bellows to the diaphragm motion and that of the AP surface motion to the bellows.

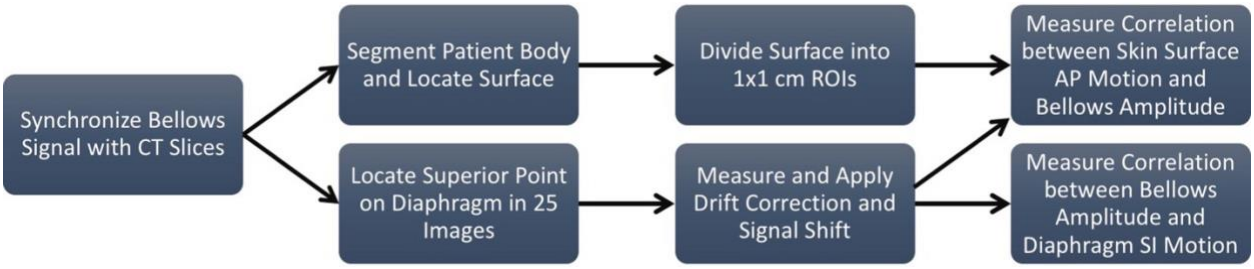

Fig. 2-1: Flowchart of the methodology. Beginning with 25 fast-helical scans, the diaphragm and patient skin surface are located and correlated with the bellows signal.

2.2.4 Error Propagation

In addition to the residual error, the error in the linear fits was also propagated from the diaphragm fit to the skin-bellows fit. This gave a numerical assessment of the accuracy of bridging the two surrogates. To measure the error contributed by inaccuracy in each linear model, the standard deviation of the relative residuals from the bellows-diaphragm linear fit was propagated with that of the skin-bellows fit. This yielded the expression in Eq. (1), which was taken to be the error in the combined linear models.

$$\sigma_{prop} = \sqrt{\sigma_{resid1}^2 + \sigma_{resid2}^2} \tag{2-1}$$

In Eq. (2-1), σ_{prop} is the propagated error, σ_{resid1} is the standard deviation of the relative residuals in the surface height linear model, and σ_{resid2} is the standard deviation of the relative residuals from the diaphragm linear model. This value provides information regarding the residual error that was due to the use of the bellows to represent the diaphragm in relating the surface motion to interior motion.

2.3 Results

2.3.1 Diaphragm Motion vs. Bellows Signal

To demonstrate the range of intercycle variability in our study, examples of breathing traces from each of the three scanners are shown in Fig. 2-2. The time shift in all bellows voltage signals was very small (mean time shift was − 0.04 s +/−0.05 s).

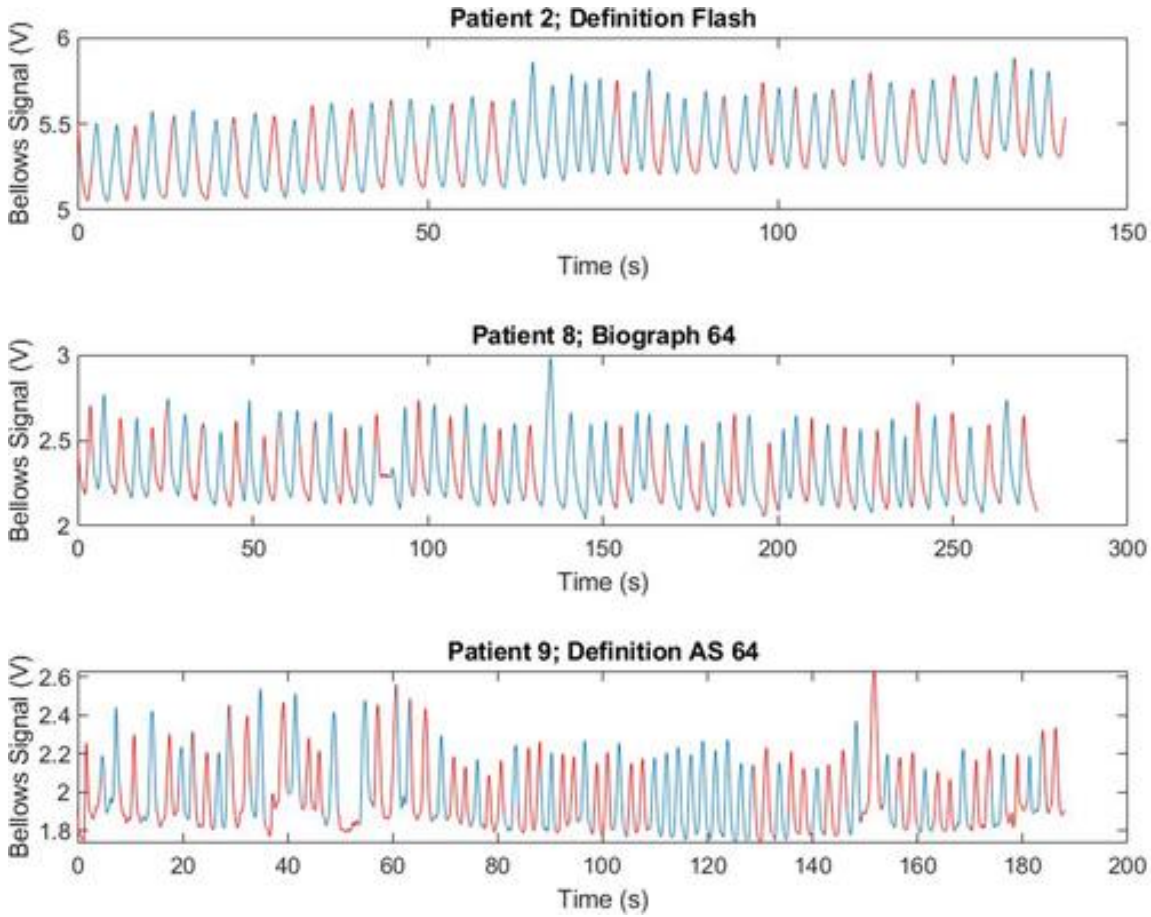

Fig. 2-2: Examples of breathing traces recorded with the bellows for patients 2, 8, and 9. The red sections of the line denote the scan-on time.

Figure 2-3 shows examples of two diaphragm HU profiles and their corresponding sigmoid fits. Figure 2-3(a) is an example of a voxel column where only parenchymal tissue lay superior to the diaphragm, while Fig. 2-3(b) is an example of a column where a blood vessel lay immediately superior to the diaphragm. The asymptotic difference, the value used to assess diaphragm position measurement quality, and the inflection point, used to denote the precise location of the diaphragm point, are also shown.

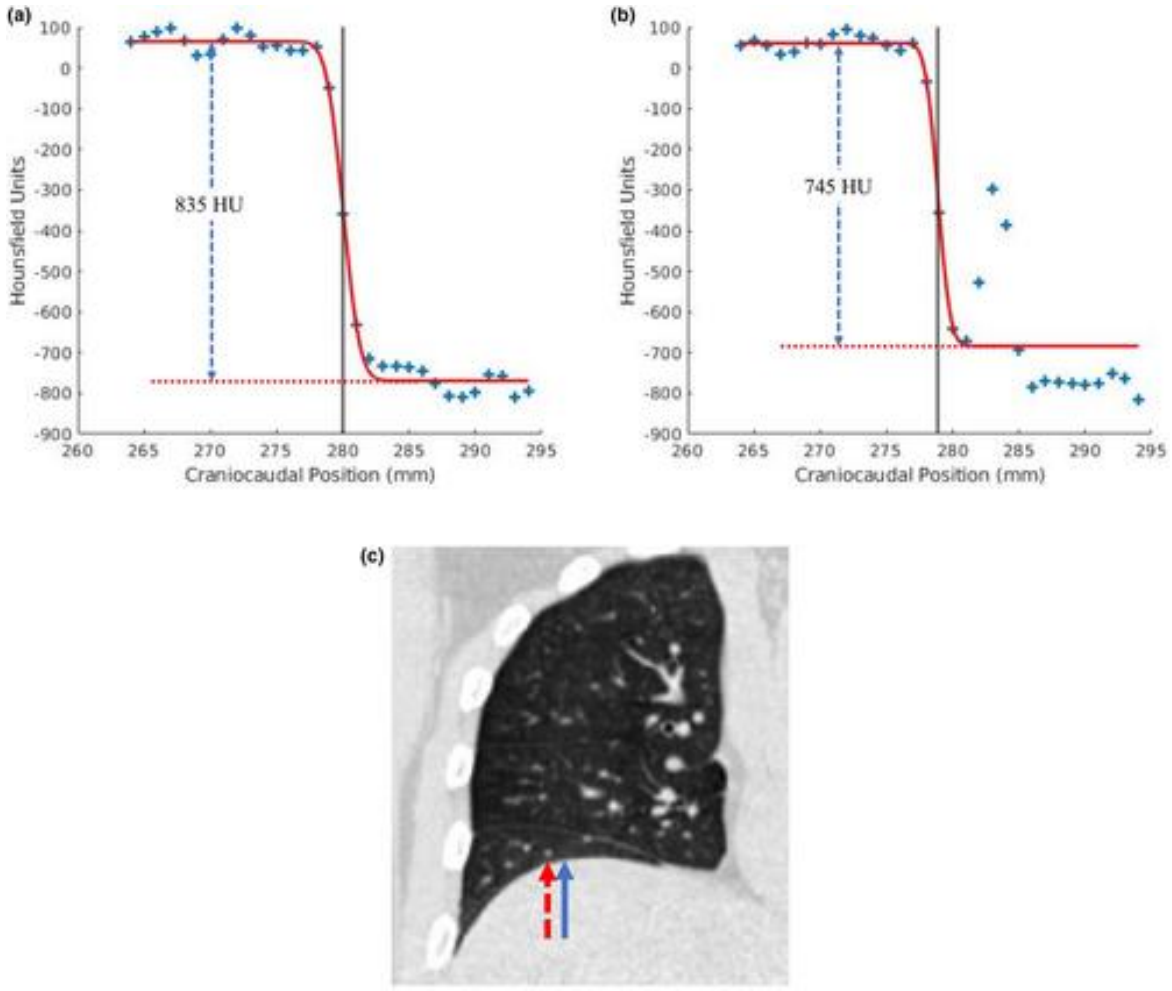

Fig. 2-3: Hounsfield unit profiles and error function fits for a point on the diaphragm of patient 11 at a selected scan. (a) Profile without unit-density tissue directly superior to the point with an asymptotic difference of approximately 835 HU. The gray, vertical line denotes the point in the fit where the inflection occurs, which is chosen as the boundary point. (b) Profile with vessels directly superior to the diaphragm point with an asymptotic difference of approximately 745 HU. (c) Positions of the profiles on the lung. The dashed arrow corresponds to the profile in (b). The lung tissue directly superior to the diaphragm is evident. The solid arrow corresponds to the profile in (a). There is no lung tissue visible directly superior to the diaphragm in this region.

Figure 2-4(a) shows the 25 craniocaudal diaphragm positions for patient 1 as a function of the corresponding drift-corrected bellows signals. The associated linear fit is superimposed on the data.

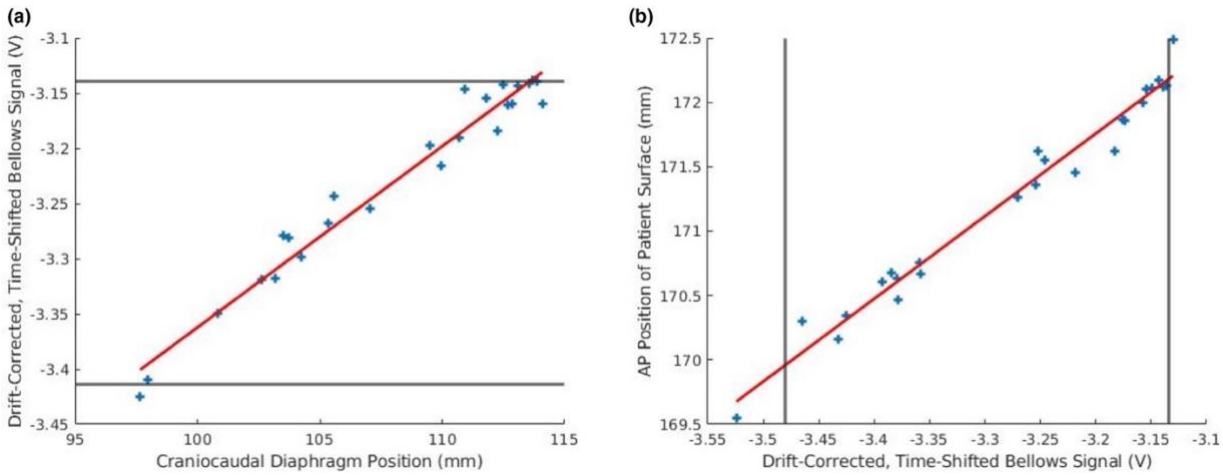

Fig. 2-4: (a) The corrected bellows signal as a function of the corresponding craniocaudal diaphragm position for patient 1 (residual error 5.87%). (b) The AP position of the patient surface for the best correlating ROI as a function of the corresponding bellows signal for the same patient (residual error 5.49%). AP position increases with exhalation. Solid, straight lines on the plots represent the 5th and 95th percentile values bellows voltage signal.

The results of studying the correlation between diaphragm motion and the abdominal bellows signal were calculated for both lungs of each patient. Patient 10 had an immobile right lung, so the residual error was not calculated for this lung. The mean relative error for all patients was 9.21% +/- 3.77% with values ranging from 3.97% to 17.7%.

2.3.2 Patient Skin Surface Position vs. Bellows Signal

Figure 2-5 shows an example of a HU profile for a point on the surface above the sternum of a patient. One profile was taken per surface point. For most points on the patient anterior surface, the HU profiles showed a clear body–air boundary. There were some points in most patients, however, that superimposed objects lying on the skin, including EKG sensors, the bellows, and breathing tubes. In these cases, the body-to-air boundaries were difficult to distinguish, resulting in missing values.

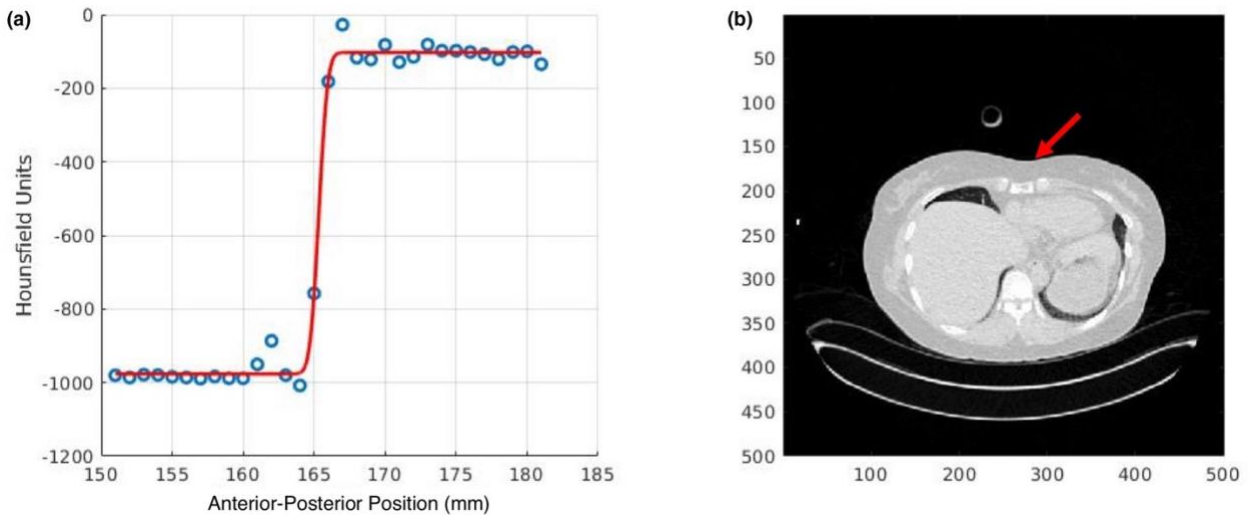

Fig. 2-5: (a) Hounsfield unit profile and error function fit for a point anterior to the sternum on a selected patient. (b) Position on the body (arrow) where the profile in (a) was taken.

An example of a patch skin-bellows fit from patient 1 is displayed in Fig. 2-4(b). Strong correlation is apparent and supported by a low residual error of 5.49%. The results of the patient surface to bellows voltage correlation show regional differences in surrogate capability of the patient surface, as well as consistent patterns among patients. Residual errors superimposed with the coronal slice midway through the AP direction of the patient for three patients are shown in Fig. 2-6.

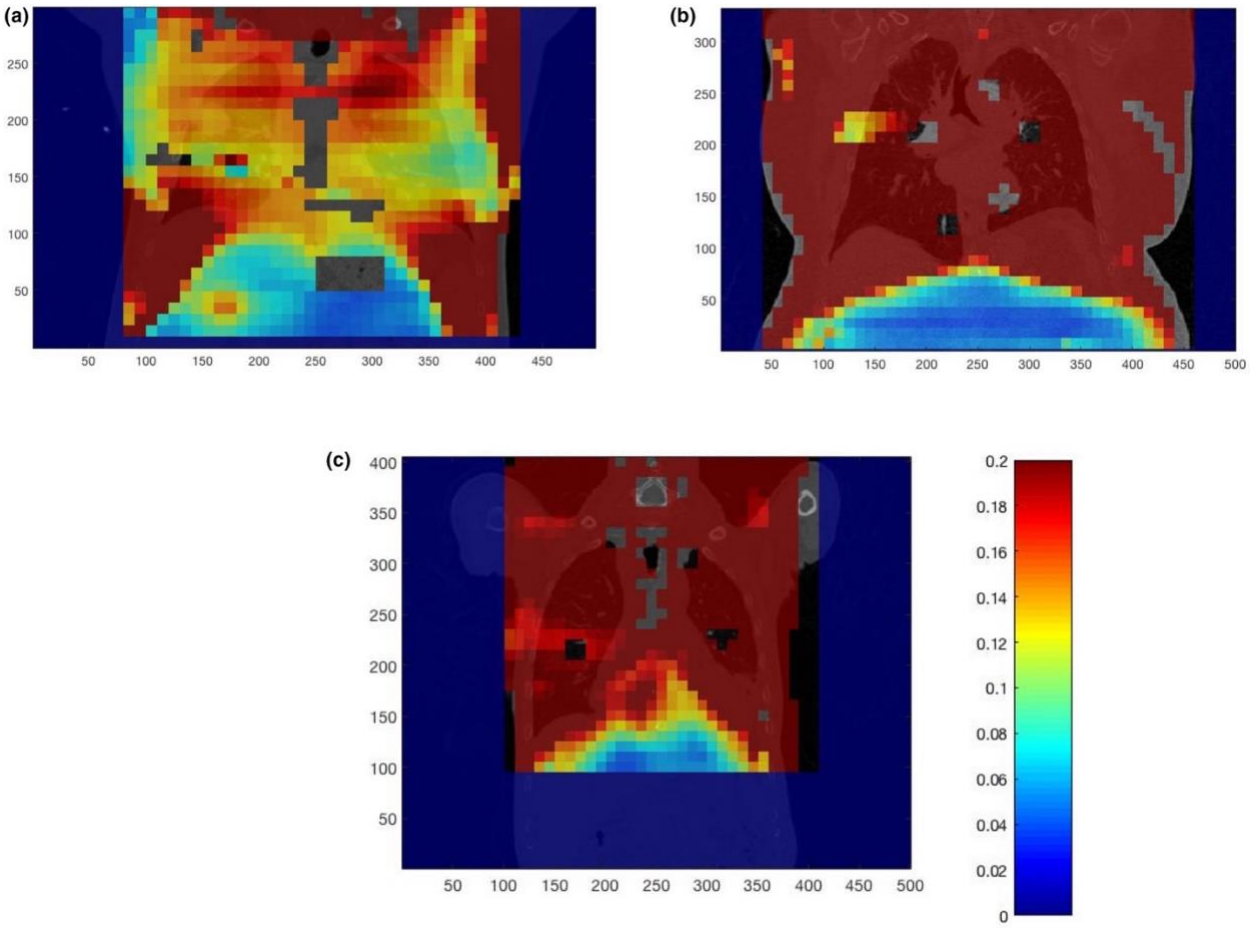

Fig. 2-6: RMS of residuals (as fractions of the 5th to 95th percentile amplitudes) of skin-bellows fits for patients (a) 5, (b) 8, and (c) 14. Values greater than 0.2 are truncated. The color bar applies to (a-c). The bellows is not imaged for these patients but lies just inferior to the imaged anatomy.

In Fig. 2-6, the three patients exhibited greater surface height to breathing amplitude correlations near the centers of their abdomens than in other areas. Patient 5 (Fig. 2-6(a)) is representative of the pattern of most patients, showing moderate to high correlation throughout the thorax with the greatest correlation at the abdomen. Patients 8 and 14 show another common pattern, where the only precise fit is found at the abdomen and residual errors are high in the thorax. The strongest positive correlation is at the abdomen as in all cases, with residual errors quickly ascending superior and lateral to the positive correlation region.

The smallest residual error from the set of skin surface patches was calculated as well as the minimum propagated error that includes the bellows-diaphragm error. The latter demonstrates the error propagated from the diaphragm position to the skin position to provide a measure of how accurately the surface motion related to the diaphragm motion. The average minimum residual error was 7.73% +/− 4.41% ranging from 2.96% to 19.4%. The average minimum propagated error was 11.8% +/− 4.61% with a range of 6.17% to 20.7%. These results suggest that there is at least one patch on each patient that could have been used as a surrogate of the diaphragm position and, consequently, as a surrogate for breathing motion modeling.

2.4 Discussion and Conclusions

In current commercial 4DCT, images are sorted according to breathing amplitude or phase, which is measured using a surrogate[21]. It is important that the external surrogate is carefully and correctly implemented to reduce breathing sorting artifacts. For accurate target volumes and conformal dose delivery, minimizing these artifacts is essential. Likewise, MBCT relies on an accurate surrogate measurement for model accuracy. Using the breathing motion model presented by Low et al.[25], breathing amplitude and rate are measured using the breathing surrogate. Tissue motion is then related to these measured quantities. A working surrogate is essential in the accurate calculation of tissue motion.

The use of FHFBCT scans enables us to measure these correlations spanning across different breaths, thus considering their variation. They also free us from commercial 4DCT sorting artifacts caused by irregular breathing. With this unique dataset, we were able to provide a comprehensive analysis of surface motion to internal motion correlation. Since the diaphragm position was not measured during the acquisition of other slices, the abdominal

bellows was used to bridge the diaphragm position in these CT images to the surface positions throughout the anterior skin surface to test the efficacy of using the skin surface as a breathing surrogate.

The bellows was placed at the abdomen to reflect clinical practice, since one aim of this work was to evaluate the use of the abdominal bellows. Since the bellows correlated well with the diaphragm, it was found to be an accurate reflection of the diaphragm position to be used in the next experiment, confirming that the increased residual error at the thorax was due to the diaphragm motion rather than a non-physical bias. However, it may be interesting to investigate how the correlation at the thorax may change if the bellows were placed there, and if the bellows would still be an accurate surrogate for the diaphragm. This could potentially expose any bias, or even result in an alternative clinical setup. Future work will examine the effect of moving the bellows superior on the torso to investigate these aspects which were outside of the scope for this study. Though this has yet to be explored, the demonstrated accuracy of the bellows as a diaphragm surrogate supports the conclusions found in this study. The drift of the abdominal bellows was quantified and corrected, so there was no issue in obtaining a useful surrogate signal for this study. However, it would be very interesting to examine what causes the drift. It has been hypothesized that heating from the patient's body causes the gas to expand and thus the signal to drift, but this has not been tested. Future work will examine potential causes of the drift since it would be informational when evaluating the usefulness of the bellows.

We provided a unique look at the entire patient surface as it correlated to the abdominal bellows, which was shown to be an accurate diaphragm surrogate. The correlation between the skin motion and corrected bellows signal depended on the surface location and was patient

specific. Generally, the best correlation was on the abdomen and near the bellows. For all patients, the correlation degraded away from the abdomen, so for surface imaging, the abdomen would be the best location for tracking diaphragm position. In addition, the flexibility of surface tracking would enable the selection of the optimal location, the avoidance of bellows drift, and the ability to investigate the separation of thorax and abdominal breathing.

More data are necessary to study the efficacy of surface mapping as a surrogate. In this study, we examined small patches throughout the patient surface, but simultaneously examining the entire chest would provide insight to how well surface mapping could perform as a surrogate, for what types of patient surface mapping would be best suitable, and other details about surrogate usefulness. Further studies will include surface imaging of patients to study correlation against the bellows and internal motion.

Having investigated the accuracy of the bellows in representing the diaphragm, the work in this chapter provides important confidence in the other chapters of this dissertation. Much of the work is based on the use of the bellows with FHFBCTs to monitor breathing amplitude. Completing this study was paramount in supporting the work in these other chapters. This chapter also investigated a topic within CT simulation, which is where the FHFBCT and 5DCT protocol are currently utilized. The next chapter extends the use of these imaging protocols to the CBCT stage of the radiotherapy workflow.

CHAPTER 3: DEVELOP AN IMPROVED FREE-BREATHING CBCT WORKFLOW FOR RADIOTHERAPY USING AN *A PRIORI* MODEL

Feasibility of Non-Iterative Motion Compensated Cone-Beam CT Reconstruction Using an a Priori Model from 5DCT

A version of this chapter is in preparation to be submitted as a manuscript to Medical Physics

3.1 Introduction

In radiation oncology, image guided radiotherapy (IGRT) describes the integration of imaging modalities with the treatment machine to enable monitoring of patient and tumor positions as well as daily changes to patient anatomy[60]. With IGRT, the patient can be re-positioned if necessary, and changes to the radiotherapy plan can be made during the course of treatment in a process known as adaptive radiotherapy (AR)[61]. IGRT and AR have given a path to reduce toxicity, escalate dose, implement hypofractionation, and improve the therapeutic ratio of treatments[62,63].

CBCT is one implementation of IGRT. CBCT is a rotating system of a cone-shaped beam, rather than the typical fan-beam used in CT, with a flat panel detector[64]. In radiotherapy, a CBCT system is attached to a linear accelerator (linac) to allow monitoring of bone and tissue position in the geometry of the linac[65]. CBCT in radiotherapy provides high spatial resolution at low imaging doses to enable excellent patient alignment[66]. Specifically in lung cancer cases, CBCT has been advantageous since tumors have such high contrast from the surrounding low-density lung parenchyma[67,68]. However, among other technical limitations, artifacts driven by respiratory motion with slow gantry rotation can disturb relevant patient anatomy by causing blur or double images[69-71].

Other groups have developed methods to try to overcome the motion artifacts in CBCT. One such effort, 4D-CBCT, is a technique that involves sorting the projections into phase bins[71,72], similar to the 4DCT approach used for CT simulation[41]. However, unlike typical 4DCT, due to a lack of sufficient projections in each phase bin, 4D-CBCT images can suffer from view aliasing artifacts[73,74] or streaking artifacts[75]. These limitations of 4D-CBCT demand more sophisticated motion management approaches.

To develop CBCT reconstruction beyond 4D-CBCT, many groups have implemented motion modeling to reconstruct CBCTs with motion compensation. One important development in motion compensated CBCT reconstruction came with Simultaneous Motion Estimation and Image Reconstruction (SMEIR) developed by Wang, et al[76]. This study sought to solve the issue of view aliasing artifacts in 4D-CBCT and their effect on subsequent motion modeling by simultaneously establishing the motion model while reconstructing the images. An initial motion model was established with reconstructed 4D-CBCT phases, then updated during image reconstruction. While this study provided a great improvement to CBCT reconstruction, its limitations included those imposed by its sensitivity to the accuracy of the initial motion model and to breathing irregularities. Several studies were published afterwards using biomechanical modeling[77] or deep learning[78,79] to improve the registration accuracy in SMEIR-based approaches. Additionally, many other groups have developed similar approaches with various implementations of simultaneous modeling and reconstruction[80-82]. However, these approaches suffer from the same limitations.

Another simultaneous reconstruction approach known as the Motion-Compensated Simultaneous Algebraic Reconstruction Technique (MC-SART) was developed by Guo, et al[83]. This approach utilized an iterative approach of reconstructing binned CBCT images with

a motion model while simultaneously refining the model. This group showed that their reconstructions outperformed two more conventional approaches: the Feldkamp, Davis, and Kress algorithm (FDK)[84] and 4D-SART[85], as well as SMEIR in terms of voxel intensity and registration error between each approach and the ground truth data. However, the motion model used in the MC-SART approach still suffered from the limitations of the CBCT reconstruction, including the lack of sufficient projections in each bin. Another limitation of MC-SART and other iterative reconstructions like it is the computation time. Since CBCT is used for on-board imaging, ensuring that the computation time is minimized is crucial to clinical translation. Additionally, the previous MC-SART study called for further analysis using patient data since only one clinical patient was tested.

As specifically addressed by Wang, et al., the use of a prior motion model could replace the need to construct models from poorly reconstructed 4D-CBCTs[76]. Previous studies have begun to investigate this approach. These have largely consisted of motion models constructed from 4DCTs[86,87]. However, 4DCT provides an unreliable method to calculating the *a priori* motion model due to artifacts, especially in cases of irregular breathing[21,88,89].

In this study, we propose an amendment to the MC-SART approach by using an *a priori* motion model constructed from 5DCT simulation data, introducing an *a priori* model based on FHFBCTs rather than 4DCTs or 4D-CBCTs. These data should improve the MC-SART approach by providing motion models based on much higher quality, dynamic images free of sorting artifacts with only one iteration. We also perform the MC-SART reconstruction on more clinical data to expand on the previous study. There was no ground truth when using clinical patient data to show that our reconstruction of free-breathing CBCTs reflected the exact positions of the anatomy. Therefore, we hypothesized that if our model was accurate, we

could control the diaphragm sharpness by altering the gating bin window used to define the amplitudes of projections. This would show that including more information from the motion model resulted in more accurate reconstruction of the diaphragm. In this study, we demonstrated this ability, thus showing accurate reconstruction of the primary moving organ in the lungs.

3.2 Materials and Methods

The overall workflow outlining the methods of this study are shown in Figure 3-1. Each of the following sections describe the processes shown in the chart.

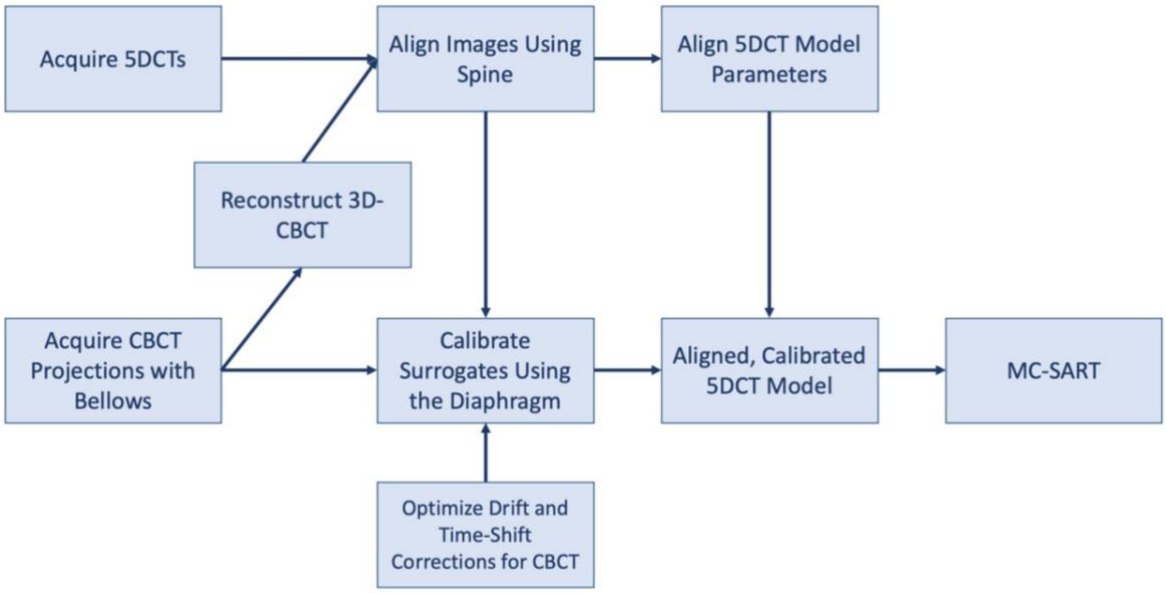

Fig. 3-1: Flowchart of our approach to apply 5DCT modeling to CBCT reconstruction

3.2.1 5DCT Data Acquisition

We employed the 5DCT patients from Chapter 2 that were scanned with the Somatom Definition AS. For each patient, 5DCT models were constructed using the formulation in Equation 1-1, as explained in Chapter 1. However, in this feasibility study, we only used the $\overrightarrow{\alpha}$ and $\overrightarrow{X_0}$ parameters for simplicity since we assumed that hysteresis motion would be negligible for this purpose. The breathing amplitude signal was drift-corrected and time-shift-

corrected as in Chapter 2. However, instead of using the correlation of the signal to the diaphragm to optimize the drift correction, we used the skin surface, following the clinical protocol. In Chapter 2, the skin surface was also proven to be a good surrogate at the center of the abdomen.

3.2.2 CBCT Data Acquisition

For each patient in this study, we also acquired CBCT images on the Novalis Tx system (Varian Medical Systems, Palo Alto, CA, USA). We acquired 668 evenly spaced projections over one 360° rotation in half-fan mode. Each projection was acquired with 110 kVp and 0.4 mAs. The total scanning time for each CBCT acquisition was 1 min. We reconstructed each CBCT with 1.33 x 1.33 mm pixel size and a slice thickness of 2 mm, yielding images that had a voxel resolution of 384 x 384 x 128. During scan acquisition, we acquired the bellows trace in the same fashion as 5DCT simulation. However, amplitudes were assigned to projections rather than slices.

3.2.3 5DCT Surrogate Calibration

To use the 5DCT model parameters during CBCT reconstruction, the surrogate signals needed to be calibrated so that the 5DCT parameters could scale the CBCT breathing waveform to obtain the correct deformations. This was largely due to the arbitrary nature of the voltage unit as well as differences in image resolution and orientation. To perform this step, we first resampled the 5DCT reference scan to match the CBCT image resolution. We then aligned the CT scans with a rigid registration using the spine as a key landmark. Then, the diaphragm positions were used as a common surrogate to obtain a relationship between the amplitude waveforms. Finally, we applied a drift correction to the CBCT waveform to maximize the

relationship between 5DCT and CBCT amplitudes at given diaphragm positions. The details of each process are explained in the following sections.

CT Alignment: To ensure that the voxel-specific, 5DCT model parameters corresponded to the correct voxels in the CBCT images, the 5DCT reference geometry had to be properly aligned to the CBCT geometry. To do this, we rigidly registered the reference scan to the 3D-CBCT reconstructed with the SART implementation from the Reconstruction Toolkit (RTK)[90] using all projections. We then resampled the 5DCT reference scan to 1.3 x 1.3 mm resolution with 2 mm slice thickness to match the CBCT and used simulated markers in the CBCT spine to rigidly align the images. The spine was our key alignment structure because it was motionless during each acquisition, so there were no changes across imaging sessions, and its reconstruction in the CBCT was of sufficient quality for alignment thanks to its lack of motion between projections.

Calibration Curves: We considered the diaphragm to be a gold standard surrogate of breathing amplitude, as we did in Chapter 2. For each projection angle, the amplitude of the CBCT was known from the CBCT surrogate signal. Therefore, finding the 5DCT amplitude that deformed the diaphragm position to align with that of the CBCT projection would identify the amplitude correspondence between images. To do this, we used a set of 200 amplitudes between the -150th and 150th percentile amplitudes of the 5DCT signal. For each amplitude, we deformed the 5DCT reference scan to that amplitude state, yielding a set of images across the amplitude range. Then, we forward projected the deformed images using the geometry of the CBCT scan. This yielded a set of simulated 5DCT projections at different amplitudes. The projection with the best alignment of the diaphragm to the CBCT projection diaphragm was

chosen by manual inspection. Once selected, the amplitude correlation for that projection was determined.

Repeating this process for a set of at least 20 aligned projections, a linear calibration was established to convert the CBCT amplitudes to the corresponding 5DCT amplitudes. With this calibration, the CBCT signal could be converted and scaled to obtain user-defined DVFs using the 5DCT model from CT simulation. Since the CBCTs were acquired with the tumors at isocenter, we chose the diaphragm of the lung that contained the tumor to perform the calibration.

CBCT Bellows Drift Correction: Because there may have been a systematic drift in the CBCT surrogate signal and we could not use the projections alone to correct it, we used the surrogate calibration as a method of drift correction. This was performed by applying a set of drift corrections between -0.0025 and +0.0025 V/s, repeating the calibration with the drift-corrected CBCT amplitudes, and re-computing the R^2 correlation coefficient of the new linear calibrations curve. The drift correction that maximized the correlation coefficient was chosen to finally correct the CBCT signal. Additionally, a small time-shift between -1 and 1 s was simultaneously optimized in the same manor to account for errors in time synchronization between the amplitude signals and the projections. The drift and time-shift correction combination that yielded the highest R^2 value was ultimately chosen to correct the signals.

3.2.4 MC-SART Implementation

The goal of the study was to improve motion compensated CBCT reconstruction with the *a priori* model from 5DCT simulation. This was realized by using the previously studied MC-SART approach and substituting the iterative motion modeling process with the fixed 5DCT model. The iterative MC-SART equation is shown in Equation 3-1[83].

$$f_{k+1}^{0} = f_{k}^{0} + \alpha \sum_{t=1}^{n} \Psi^{-t} \frac{A^{T}(p^{t} - A\Psi^{t} f_{k}^{0})}{w^{T} w} \tag{3-1}$$

In Equation 3-1, f_k^0 represents a reference CBCT image for iteration, k. Ψ^t and Ψ^{-t} represent DVFs and inverse DVFs, respectively, mapping the reference image f_k^0 to and from the patient amplitude acquired at time, t. A and A^T are forward and back projection operations, respectively. The weighting parameters, w and w^T are used to account for inhomogeneities during forward and backprojection. α is a relaxation factor that adjusts the contribution of the summation term. The summation is calculated for the acquisition times of n projections.

In this study, the DVFs Ψ^t and Ψ^{-t} were calculated using the 5DCT model. We used the amplitudes at the time of each projection, t, to scale the model to obtain the appropriate DVFs. Additionally, we performed one iteration of Equation 3-1 using an α of 160,000, which was empirically determined to yield the highest quality images in the lowest number of iterations. This approach replaced the previous technique of fitting binned 4D-CBCT reconstructions to obtain a motion model and improving the model through an iterative process. Using a single iteration greatly reduced the computation time, which is advantageous in a clinical setting. A schematic of the general, iterative approach applying Equation 3-1 is shown in Figure 3-2.

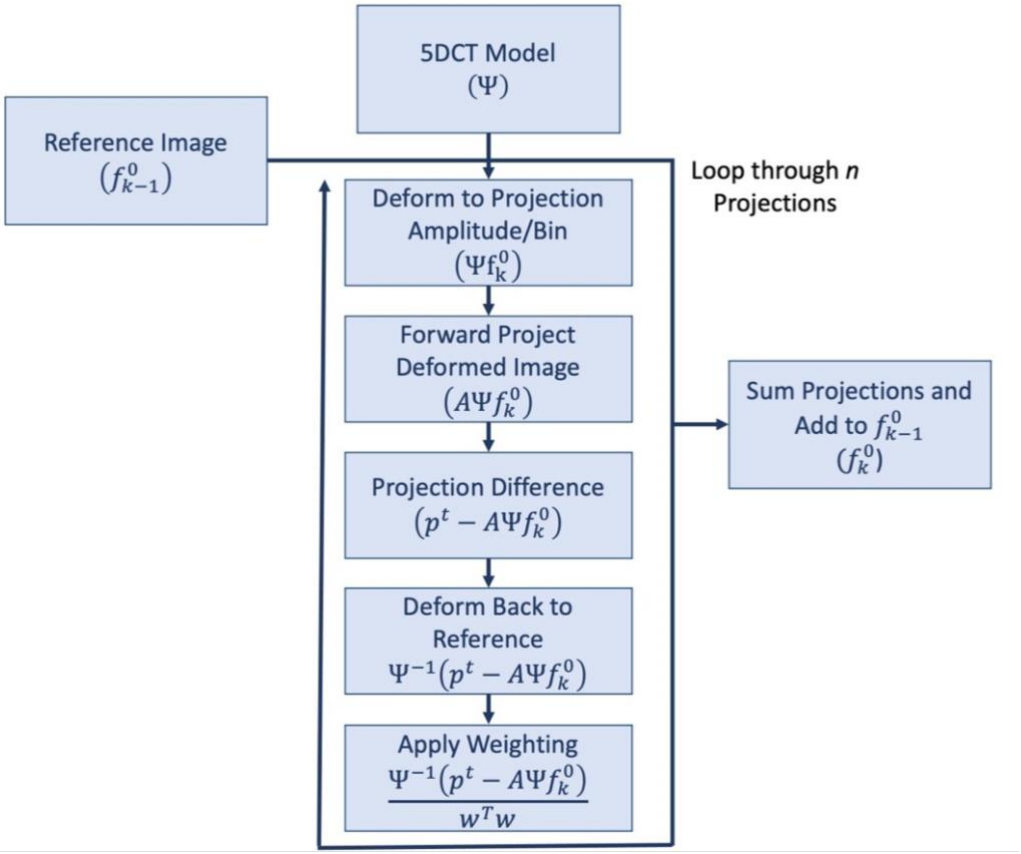

Fig. 3-2: Flowchart of the MC-SART reconstruction approach using 5DCT

3.2.5 Binning Strategy

To study the effect of amplitude gating on the diaphragm sharpness as an indicator of modeling accuracy, we reconstructed a set of images using several amplitude binning techniques. For each patient, we reconstructed CBCTs using the SART implementation from RTK for a comparison to a conventional technique. We then reconstructed MC-SART images using our approach with different bin sizes.

We divided the amplitude range into 2, 3, 4, and 8 bins and assigned each projection to the bin associated with its amplitude. We then used the deformation vector field $\Psi^{bin(t)}$ to obtain the difference image, $p^t - A\Psi^{bin(t)} f_k^0$, in Equation 3-1, where $bin(t)$ was the mean amplitude of the bin to which the projection angle at time, t, was assigned. In the case without gating, we

scaled the model to the measured amplitude of each projection angle to obtain Ψ^t, rather than assigning any projections to bins. This process could demonstrate the accuracy of the modeling because if we increased the number of bins, the diaphragm sharpness was expected to improve due to increasingly accurate modeling of its position at the time of each gantry angle.

3.2.6 Evaluation of Diaphragm Sharpness

To evaluate the accuracy of our motion model via diaphragm sharpness, we employed a sharpness metric from the work of Low, et al. designed to measure motion blur[33]. For each reconstructed image, we chose a profile that crossed the diaphragm dome boundary. We fitted a sigmoidal error function to the profiles and used two measures of blur calculated from the fit. The error function equation with the parameters used for fitting is shown in Equation 3-2, where x is the array of attenuation coefficients across the profile and a, b, σ, and d are parameters optimized in the fit.

$$y(x) = a - b * \text{erf}\,(\sigma * x + d) \tag{3-2}$$

The first measure of diaphragm blur was the width of the range between the 20% and 80% intensities of the error function, termed the *80%-20% distance*. This metric revealed the width of the linear region of the error function, which corresponded to the blurred diaphragm boundary in the image. The second was the fit parameter, σ, which was directly proportional to the slope of the linear region of the error function, thus similarly representing the width of the blur. Our hypothesis was that the 80%-20% distance would be largest in the SART reconstruction and would decrease as the bins became narrower. We hypothesized, then, that σ would increase with narrower bins.

3.3 Results

3.3.1 Bellows Signal Calibration

Examples of the surrogate signals during 5DCT and CBCT acquisition for one patient are shown in Figures 3-3a and 3-3b, respectively. The 5DCT signal includes 25 FHFBCTs, is drift corrected, and has an optimized time shift to account for errors in synchronization. The raw CBCT signal in Figure 3-3b was not yet corrected.

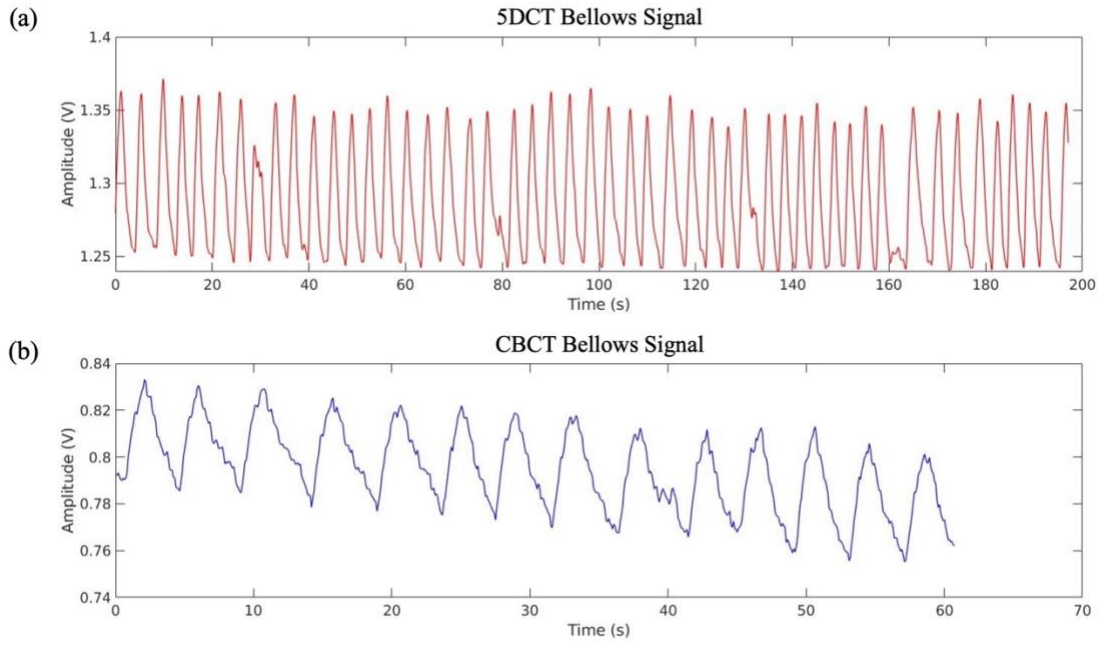

Fig. 3-3: Breathing trace examples. (a) Example of a drift-corrected, time-shifted 5DCT amplitude trace during acquisition of the 25 FHFBCT scans. (b) Example of a raw, uncorrected bellows signal during CBCT acquisition.

Figure 3-4 shows an example of the rigid alignment of the 5DCT reference scan to the SART-reconstructed CBCT scan using the spine. Images show coronal slices of the scans for the same example patient used in Figure 3-3. Red crosshair markers have been placed at the same voxel position in each image to demonstrate the relative positions of the spine to the markers. With the 5DCT image resized and resampled, and the alignment shown in Figure 3-4, the voxel-specific motion model parameters could be used with the CBCT geometry.

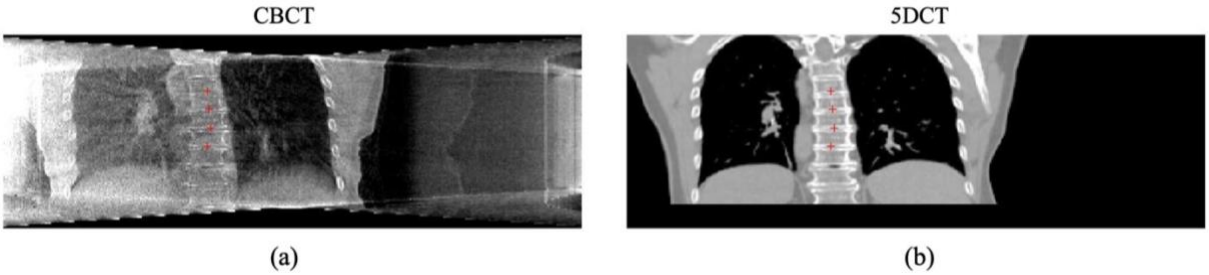

Fig. 3-4: Examples of rigid alignment of the spines. (a) Coronal slice of the CBCT scan with visible spine. (b) Coronal slice of the aligned 5DCT reference scan. Red crosshairs indicate markers at the same voxel locations used to aid alignment.

Figure 3-5 exemplifies the process of aligning the diaphragms to obtain one of the projection points on the bellows signal calibration curve. The top row of Figure 3-5 shows the same raw CBCT projection acquired at 80.3° with an amplitude of 0.782 V. The bottom row of Figure 3-5 shows simulated projections at the same gantry angle obtained by forward projecting through the 5DCT reference scan deformed to different amplitudes. The projection in Figure 3-5a was obtained by projecting through the 5DCT reference scan deformed to an amplitude voltage of 1.27 V, which was lower than the correct calibration voltage. Figure 3-5c was obtained by projecting through the 5DCT reference scan deformed to 1.36 V, which was higher than the calibration voltage. Figure 3-5b shows the correctly aligned diaphragms for the projection through the 5DCT reference scan deformed to 1.33 V.

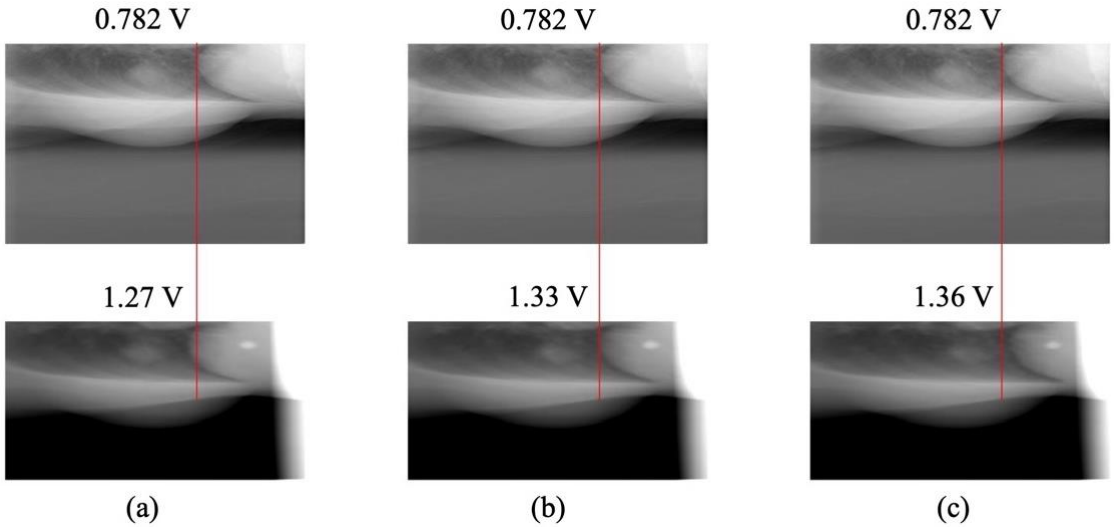

Fig. 3-5: (Top Row) Projection angle from CBCT acquisition at 80.3° with amplitude 0.782 V. (Bottom Row) (a) Simulated projection through 5DCT-generated image at 1.27 V. (b) Simulated projection through 5DCT-generated image at 1.33 V. (c) Simulated projection through 5DCT-generated image at 1.36 V.

The process exemplified in Figure 3-5 was repeated for 55 projection angles to establish a correlation of the CBCT amplitudes to the 5DCT amplitudes. Figure 3-6 shows the resulting calibration curve, which was a scatter plot of the 5DCT and CBCT amplitudes where the diaphragms were aligned, for the patient shown in the previous figures. This calibration curve used the raw amplitude signal of the CBCT projections and yielded an equation of $V_{5DCT} = 2.84 * V_{CBCT} - 0.907$ with an R^2 value of 0.75. Therefore, according to this curve, to use the 5DCT model with this CBCT dataset, the CBCT amplitudes would be converted using this equation. However, the R^2 value of the linear fit equation was improved through the drift and time-shift corrections as shown in the next section.

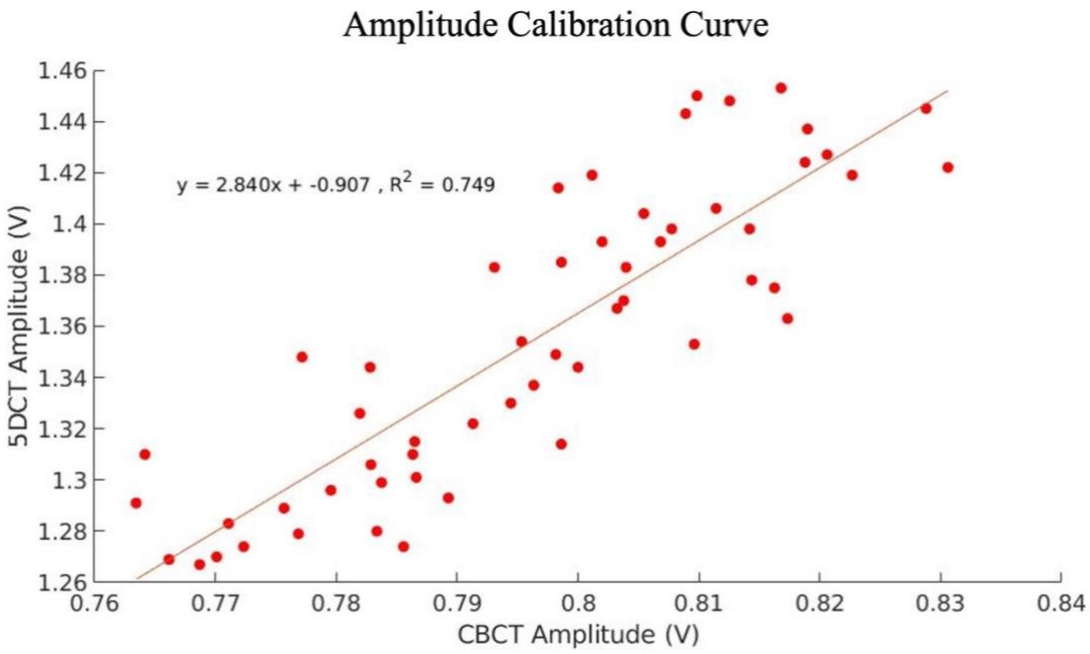

Fig. 3-6: Calibration curve with no drift or time-shift corrections. The resulting calibration equation and R^2 value are displayed on the plot.

3.3.2 Drift and Time-Shift Corrections

Figure 3-7 shows an example of the R^2 values obtained by applying each tested drift and time-shift correction during optimization for the example patient. The figure shows a 2D heatmap where the color axis represents the R^2 achieved for the corresponding drift and time-shift corrections. For this patient, the optimal drift correction was -0.0004 V/s, and the optimal time-shift was -0.14 s, thus yielding an improvement of R^2 from 0.749 to 0.935.

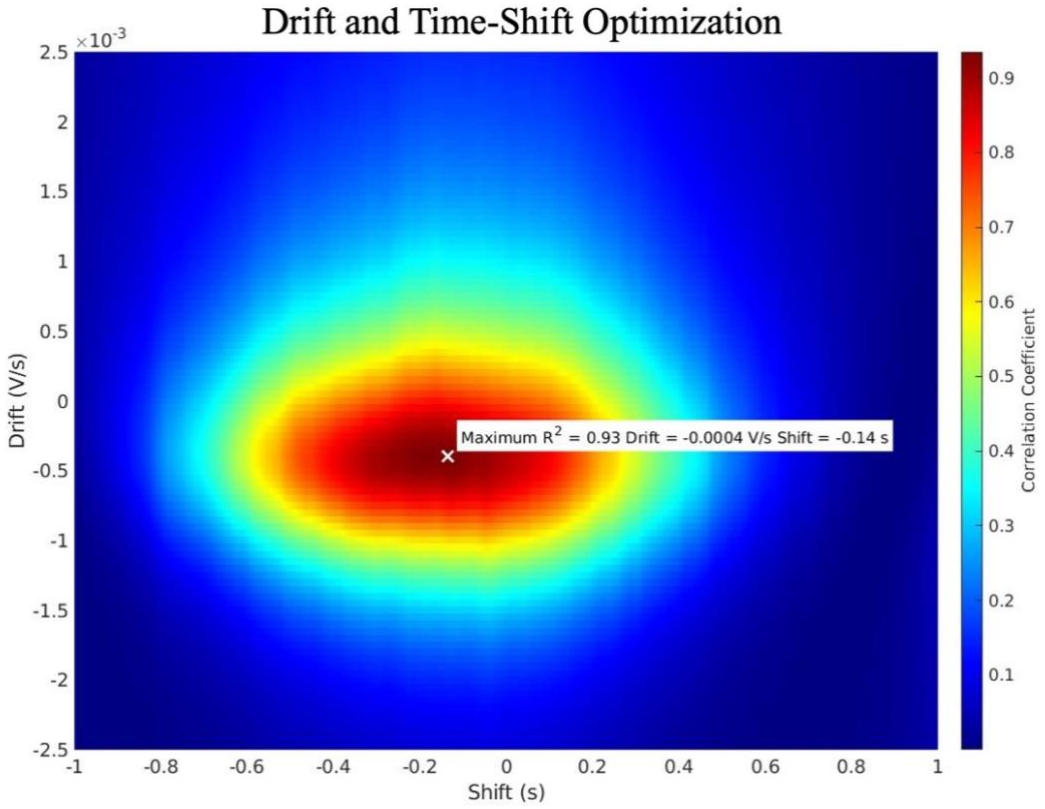

Fig. 3-7: Heatmap of all tested combinations of drift and time-shift corrections. Color indicates the R^2 of the calibration curve with the corresponding corrections. The optimal corrections and resulting R^2 value are displayed on the heatmap.

To show the effect of the optimized drift and time-shift corrections, Figure 3-8 shows comparisons of the results before and after corrections for the example patient shown in the previous figures. Figures 3-8(a-b) show the CBCT amplitude signal from Figure 3-3b and the same signal with the applied corrections, respectively. Figures 3-8(c-d) show the calibration curve from Figure 3-6 and the improved calibration curve with the applied corrections, respectively. The calibration curve in Figure 3-8d was utilized in the CBCT reconstruction of this patient.

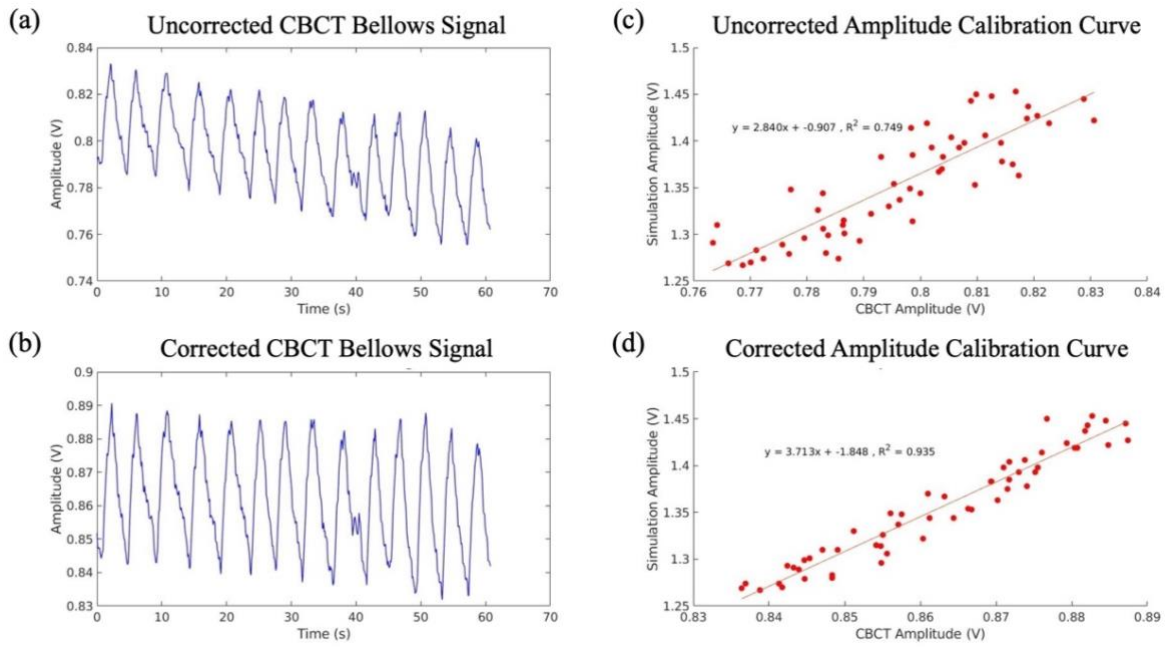

Fig. 3-8: (a) Raw, uncorrected bellows signal during CBCT acquisition. (b) Drift and time-shift corrected bellows signal during CBCT acquisition. (c) Calibration curve comparing 5DCT amplitudes to raw, uncorrected CBCT amplitudes. (d) Calibration curve comparing 5DCT amplitudes to drift and time-shift corrected CBCT amplitudes.

Table 3-1 summarizes the results of the drift and time-shift corrections and the resulting calibrations for all six patients. All drift corrections were between -8.0×10^{-4} and 1.5×10^{-4} V/s. All time shifts were less than 0.4 s and thus only corrected minor errors in time synchronization. All calibrations had an R^2 above 0.800, and the average R^2 was 0.908, demonstrating effective calibrations between amplitude signals.

Table 3-1: Drift and time-shift corrections to CBCT bellows signals and resulting calibration data

Patient	Drift Correction (V/s)	Time Shift Correction (s)	Calibration Slope	Calibration Intercept	R^2
1	0	0.045	1.02	-0.0376	0.943
2	$-4.0*10^{-4}$	-0.135	3.71	-1.85	0.935
3	$-2.5*10^{-4}$	0.105	0.238	0.387	0.894
4	$-8.0*10^{-4}$	-0.195	1.82	-0.982	0.965
5	$-7.5*10^{-4}$	-0.005	0.842	-0.548	0.817

6	$1.5*10^{-4}$	-0.320	6.73	-4.27	0.892

3.3.3 Non-Iterative MC-SART Reconstruction

The first set of figures continues the patient example highlighted in Section 3.3.2. Figure 3-9 shows the reconstructed images including all tested gating bins and the conventional SART reconstruction for comparison. The SART reconstruction visually shows a higher level of noise throughout the image. Additionally, the MC-SART reconstructions all demonstrate a marked increase in contrast and sharpness at the diaphragm and even around the tumor, which are key areas for motion tracking and target delineation, respectively. Moreover, the diaphragm was observed to sharpen with an increase in gating bins, with comparable results between 8 bins and the reconstruction with no gating.

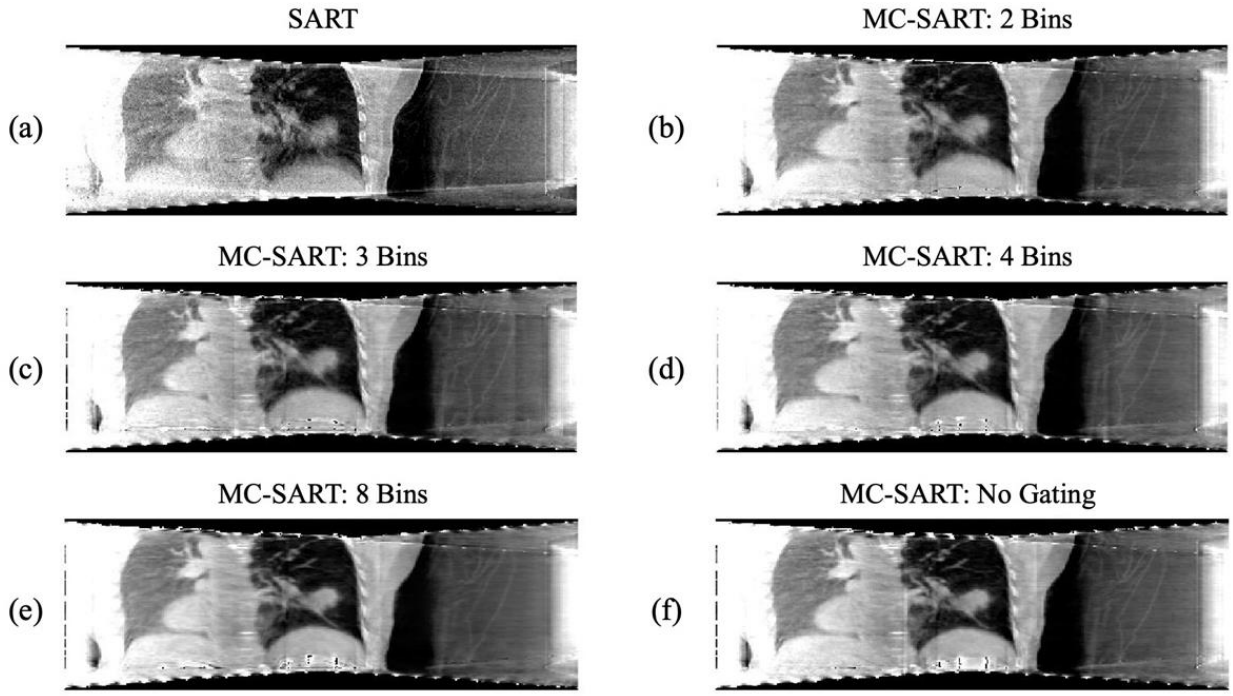

Fig. 3-9: (a) Reconstruction of CBCT using SART with no motion compensation. Reconstruction of CBCT using MC-SART with (b) 2, (c) 3, (d) 4, and (e) 8 amplitude gating bins. (f) Reconstruction of CBCT with no gating. All images were reconstructed with α = 160,000 and 1 iteration.

For each patient, MC-SART resulted in a sharper diaphragm than SART with increased diaphragm sharpness as the number of bins increased, but the effect was more pronounced in some patients than others. The results of each reconstruction for all patients are shown in Figure 3-10. The images in Figure 3-10 were cropped to focus on the diaphragm since it was the key indicator of successful motion compensation in this feasibility study. Patients 1, 2, 3, and 6 best demonstrated the gradual increase in diaphragm sharpness with increased binning. In Patients 4, and 5, the diaphragm was improved from SART, but the gating effect was minimal. The following section includes the quantitative analysis of this increase in diaphragm sharpness using the error function fitting approach to measuring the blur at the diaphragm.

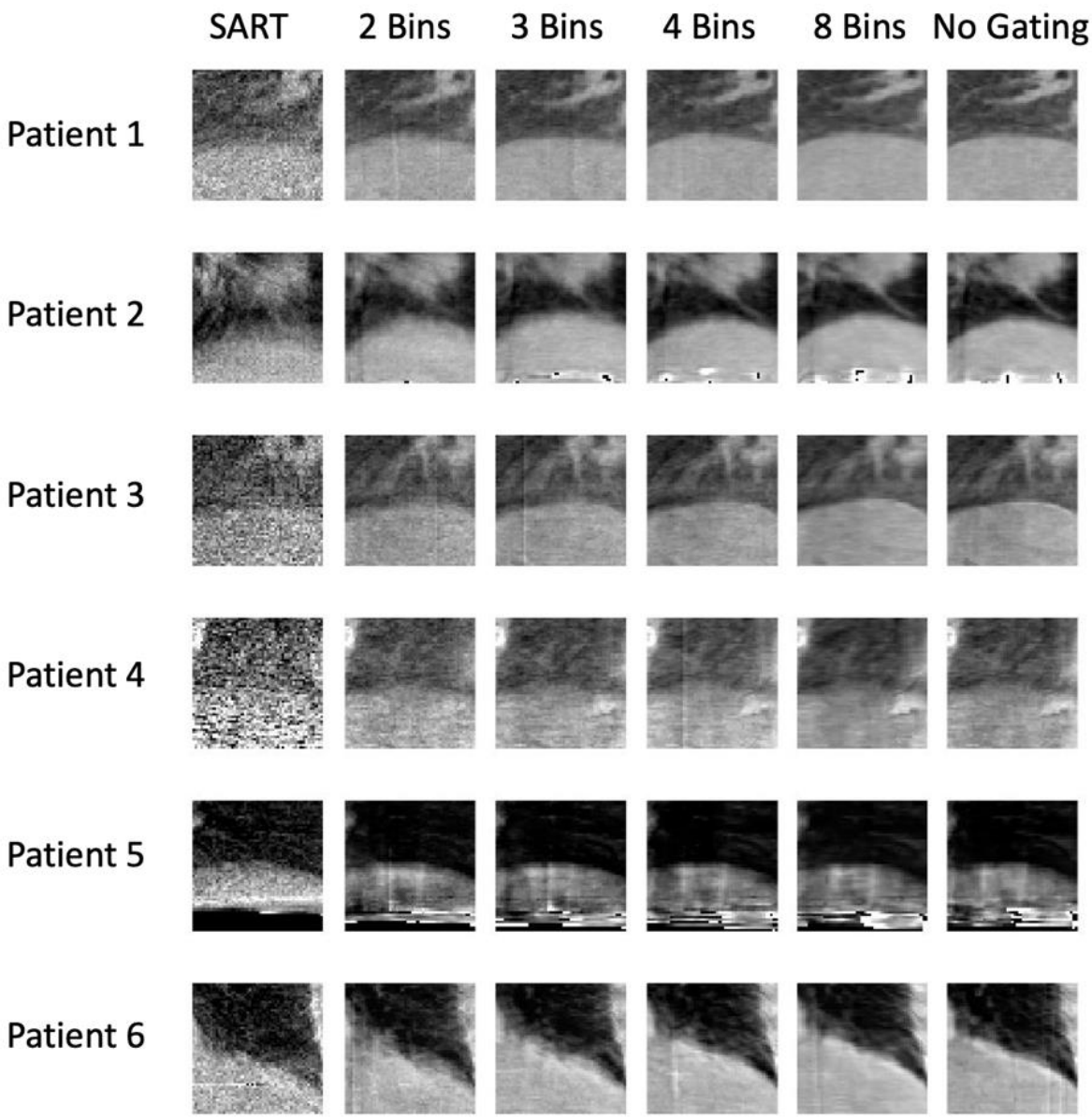

Fig. 3-10: Cropped CBCT reconstruction images at the diaphragm for all patients (rows) and all gating techniques (columns).

3.3.4 Diaphragm Sharpness

Starting again with the highlighted patient example, Figure 3-11 shows the error function along the indicated profile in Figure 3-11a at the diaphragm dome. Figures 3-11(b-d) and 3-11(f-h) show the error functions for all gating strategies and the SART reconstruction. Figure 3-11e on the bottom left shows the changes in both diaphragm sharpness parameters with

increasing bin numbers to demonstrate the effect of gating on diaphragm sharpness. In this case, the increased bin numbers successfully improved diaphragm sharpness until 8 bins, after which there was a slight decrease in sharpness. Both metrics used to evaluate sharpness from the error function fitting followed the same pattern of improvement.

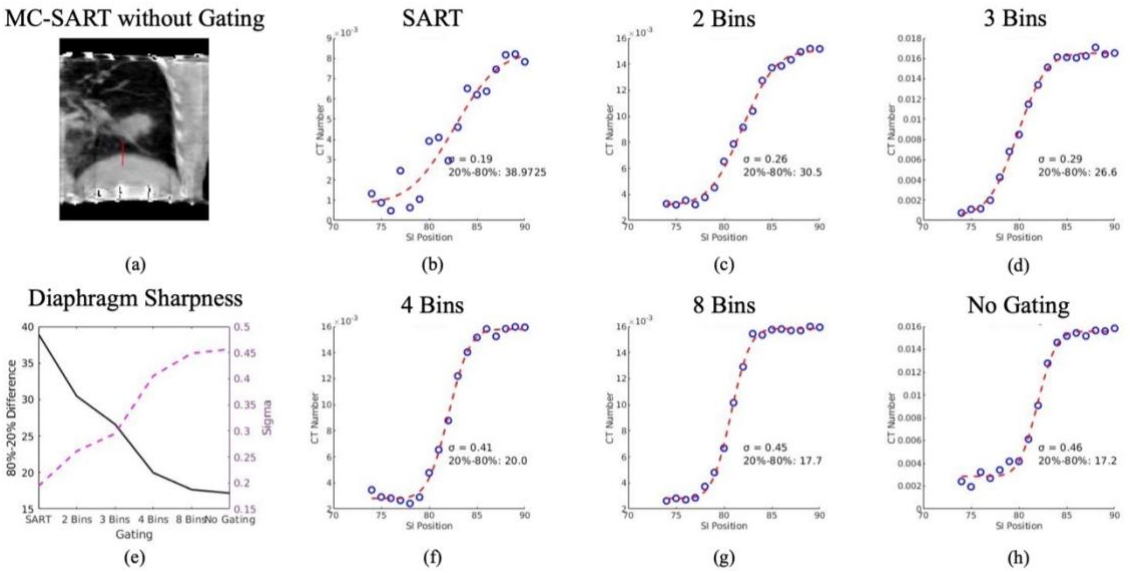

Fig. 3-11: (a) Coronal slice of the CBCT reconstruction at the diaphragm dome with line profile used for error function fitting indicated by the red line. Profile plots (circular datapoints) and fitted error functions (dotted lines) for reconstructed CBCT images with (b) SART and MC-SART using (c) 2, (d) 3, (f) 4, and (g) 8 bins. (h) Profile and error function for MC-SART reconstruction without amplitude gating. (e) Line plot showing the increase in diaphragm sharpness with increase in number of bins.

Tables 3-2 and 3-3 summarize the diaphragm sharpness results for all patients. Table 3-2 includes the diaphragm sharpness results using the 80%-20% distance while Table 3-3 includes the σ fit parameter. For each patient, the sharpness metrics are listed for each MC-SART gating strategy as well as the SART reconstruction. These numbers confirm the same pattern seen in the highlighted example from Figure 3-11. The consistent increase in diaphragm sharpness for the first 3 patients reveals that the motion compensation was successful. Therefore, in the absence of a ground truth, there is evidence of successful motion compensation using our approach.

Table 3-2: Summary of the decrease in the 80%-20% distance with increasing bin numbers

Diaphragm Sharpness: 80%-20% Distance						
Patient	SART	2 Bins	3 Bins	4 Bins	8 Bins	No Gating
1	34.2	27.1	18.3	16.2	12.3	11.9
2	39.0	30.5	26.6	20.0	17.7	17.2
3	32.9	25.0	16.6	10.1	7.54	3.01
4	8.99	36.6	26.8	56.3	32.3	35.2
5	19.9	18.2	14.8	20.8	16.2	18.6
6	10.1	19.9	32.0	14.7	12.2	17.5

Table 3-3: Summary of the increase in σ with increasing bin numbers

Diaphragm Sharpness: σ						
Patient	SART	2 Bins	3 Bins	4 Bins	8 Bins	No Gating
1	0.231	0.294	0.438	0.493	0.658	0.670
2	0.194	0.261	0.294	0.405	0.449	0.457
3	0.239	0.322	0.485	0.828	1.06	3.82
4	0.932	0.217	0.296	0.123	0.244	0.223
5	0.399	0.439	0.525	0.387	0.485	0.425
6	0.796	0.393	0.248	0.553	0.659	0.461

3.4 Discussion and Conclusions

CBCT reconstruction is still in need of improvements in motion management. Solutions based on the 4D sorting approach suffer enough from artifacts that a better solution is necessary. Though others have incorporated *a priori* models to improve CBCT reconstruction, they included the 4D sorting approach in either the CBCT, *a priori* modeling, or both. In this chapter, we presented findings from the first motion-compensated CBCT reconstruction based on free-breathing CBCT projections and a free-breathing-based, *a priori* model. We were able to demonstrate the modeling accuracy of this approach by demonstrating control over the

diaphragm sharpness. With increasing information used by the model, we were able to reconstruct sharper diaphragm boundaries.

For 3 of the patients, the diaphragm sharpness did not quantitatively show a marked increase like the others as the number of bins was increased. However, the images in Figure 3-10 show that the diaphragm was consistently sharp across gating approaches. Therefore, quantitative metrics may have shown roughly the same sharpness with noise in the pattern due to minor sources of error throughout the modeling process. Another potential cause for this result could be the high level of noise in the SART reconstruction causing poor error function fits erroneously suggesting high sharpness, especially in the case of Patient 4.

The diaphragm was our focus because it is the primary driving force of respiratory motion, which is what we aimed to model. It is also the anatomy that is most directly related to our breathing surrogates and has been previously studied in this regard[59]. The diaphragm is also a clear boundary that is consistently visible in each patient and large enough to evaluate in a straightforward manner. However, the goal of CBCT is to align the tumor to the PTV. Therefore, in our next studies, we will evaluate the reconstruction of the tumor region and other key anatomy for radiotherapy planning in more detail.

In this work, we aligned the diaphragms of the simulated projections from deformed CT simulation images and raw projections from the CBCT acquisition to calibrate the breathing surrogates. This was performed over a sufficiently wide range of projections spanning multiple breathes, so the impact of small errors could be minimized, and the R^2 values of the amplitude alignments demonstrate our accuracy. However, in the future, we will work to design an automated approach for this step to be more time efficient and accurate. This was difficult for this study because the left and right diaphragms often had different calibrations due to the

relative position of one diaphragm to the other changing from day to day. Therefore, creating an automatic alignment was difficult because of the shadows of one diaphragm on the other interfering with the projection alignment. Creating a method to avoid this issue will be a key effort in future work.

Though the 5DCT motion model has been well-validated and used clinically, there are still limitations that carry through its application to CBCT reconstruction. One such limitation is motion blur, especially at the diaphragm. While the speed of the fast-helical imaging mitigates motion blur, there are still certain cases where blur is present which could influence the accuracy of the consequential steps in calibrating the models in this study. To improve this, future work will include incorporating the motion model into the reconstruction of the FHFBCT projections, much like the work done in this study.

Finally, additional work should focus on optimizing the reconstruction parameters. To demonstrate feasibility in this study, we found parameters that yielded high-quality reconstructions. We were able to achieve these results with a single iteration, as opposed to the required multi-iteration process of the initial MC-SART workflow[83], which could make this technique more feasible for a clinical setting. However, before further development and implementation of this technique, the α parameter in the MC-SART equation and the number of iterations used should be studied intimately to ensure that the best image quality can be obtained in a clinically relevant time frame.

In conclusion, we developed an entirely free-breathing-based workflow to apply an *a priori* model to CBCT reconstruction. We demonstrated modeling accuracy through control of the diaphragm with different amplitude gating bins. Future work will evaluate other aspects of CBCT imaging, such as image contrast in different parts of the anatomy, image noise, and

other qualities. Though we have demonstrated the feasibility of using such a model and have shown its effectiveness in reconstructing the diaphragm, there is much more work to continue improving imaging results and evaluating all aspects of these improvements.

The work in this chapter demonstrated that FHFBCTs could be used to improve the CBCT stage of the radiotherapy workflow. Though FHFBCT has been used in radiotherapy for CT simulation, it can provide valuable information for CBCT reconstruction. Importantly, since it already exists in the workflow, it can be applied without adding any dose. The next chapters will all focus on extending FHFBCT beyond radiotherapy as the scope of our applications broaden even further.

CHAPTER 4: DESIGN A CFD-COMPLIANT AIRWAY MESHING ALGORITHM TO ENABLE DOWNSTREAM CFD AIRFLOW MODELING FOR SURGICAL PLANNING

Automatic Triangulated Mesh Generation of Pulmonary Airways from Segmented Lung 3DCTs for Computational Fluid Dynamics

A version of this chapter has been published as a manuscript: IJCARS, Vol. 17, No. 1, 2022. doi: 10.1007/s11548-021-02465-3

4.1 Introduction

Fluid Structure Interaction (FSI) is heavily involved in many biological mechanisms, from the elastic wings of insects to the human cardiovascular system, and it can aid in scientific understanding and lead to improvements in treatment management[91,92]. Several groups have suggested that a complete FSI model for pulmonary airflow and tissue interactions could benefit patients with respiratory conditions requiring ventilation, deposition of therapeutic particles, or surgery[93-95]. We envision a FSI lung model for lung-related interventional applications (e.g. radiotherapy or LVRS), complete with established CT motion[26], biomechanical property estimation models[96], and airflow dynamics simulation[97]. This vision relies on the unique capabilities of FHFBCT to provide the necessary dynamic breathing information to fully realize these models.

CFD has been utilized in numerous pulmonary airflow studies[97-99] for airflow dynamics simulation. However, to enable successful simulations, it is necessary to generate an accurate mesh geometry of the pulmonary airway structure from 3D/4D medical images. For our vision, it is especially necessary to generate these mesh geometries using FHFBCT data. The generated mesh should accurately reflect anatomical geometry and should not have any errors

that could result in leaking airways or blocked airflow. Therefore, the integrity of an automatic pulmonary airway mesh is the focus of this study.

Previous studies have used various conventional meshing methods. Several have used commercial software, such as GAMBIT by FLUENT, VIDA/PASS, or MIMICS[100-104]. These software applications can require time-consuming, manual correction of resulting meshes. Open-source software programs exist that generate meshes from 3D medical image DICOMs, such as 3D Slicer or MeshLab that employ surface reconstruction algorithms such as Marching Cubes (MC)[105-107]. However, when applied to lung airway geometry, resulting meshes lack explicit constraints for avoiding holes and airway blockages, so they can experience both, which can lead to escaping or impeded airflow volumes. These errors would require the same time-consuming, manual intervention.

Previous work with CFD in lung airways has also included idealized, analytical geometry based on established work by Weibel discussing the morphology of the human lung, thus not representing real anatomical data[108-110]. These idealized geometries can reach higher resolution and quality than real human anatomy retrieved from medical images, such as a FHFBCT. To aid in the interventional arena, work with CFD simulations of airflow through pulmonary airways needs to shift towards real patient anatomy built with a more automated meshing solution.

The need for anatomy-specific meshing has been addressed with various novel approaches. A large collection of work has been dedicated to tracking similar geometrical features in blood vessels, such as 1-D centerlines, cross-sectional approaches to detecting the surface, and bifurcation detection, summarized in a review by Lesage et al.[111]. These efforts have provided inspiration for tracking features in pulmonary airway anatomy, but a careful triangulation using

these features is required to enable CFD applications. Some groups have formulated sophisticated methods for tracking the airway features in the meshing process[112,113], and extensive work has also been developed to re-mesh problematic meshes from other generic methods[114,115]. However, the objectives of these efforts have not explicitly included avoiding the missing triangles or surface intersections that leak or impede flow, respectively. The focus of this work is to specifically address this issue with a novel meshing approach using FHFBCTs that requires no remeshing or repair to be CFD-compliant.

In this paper, a simple, fast, automatic, CFD-compliant meshing technique focused on the specific nature of meshing lung airway geometry is presented[116]. FHFBCTs were employed for the segmentation to demonstrate that they can provide the necessary geometry to enable CFD simulations with free-breathing data. Airway branches were isolated, and bifurcations were identified in the airway skeleton to allow for careful meshing around these features. One patient is showcased to demonstrate detailed results, while a total of six patient FHFBCT scans were used to provide further results.

4.2 Materials and Methods

4.2.1 Terminology

The following definitions are used in this section: The term medial skeleton describes the median line through the center of the airways. A branch describes the bronchi or bronchioles. These features are included under one term to generalize the different generations. A branch point is any point in the skeleton point cloud along these branches. A bifurcation is defined by the splitting of branches into new generations, so a bifurcation point is the skeleton point where this split occurs. The points at either end of a branch, which form a bifurcation, are called terminal points. Three terminal points meet around a bifurcation.

The skeleton points track the middle of the airways, but the points on the surface of the airway structure need to be considered for the mesh. A surface point is a member of the point cloud based on the outline of the airway segmentation. This was obtained using the outline plugin in ImageJ[117]. The plugin detects the outer boundary of a binary image, which was then converted to a point cloud for use with the meshing algorithm. In this approach, points were generated around the skeleton to match the outline points. These are called radial points to distinguish between the true outline points and the generated ones used in the mesh. Finally, a connectivity matrix is defined as the matrix that maps vertices to be connected in the meshing triangulation process.

4.2.2 Preprocessing of Lung Geometry

Given a 3D lung volume from FHFBCT scans, an initial segmentation was performed using the automatic segmentation package, pulmonary toolkit (PTK)[118], to generate a binary airway mask. For the implementation and validation in this study, PTK was integrated with our algorithm to demonstrate the automated nature of our process. Accurate meshing does not rely solely on PTK to provide segmentation of the airways. The medial skeleton of the binary airway mask was then obtained based on an implementation of the 3D thinning algorithm[117,119]. This approach from Lee et al. employs an Euler characteristic formula to relate objects, holes, and cavities in a simple manner. A sample of the raw output is shown in Figure 4-1a. The medial skeleton was then exported as a 3D point cloud for the subsequent steps.

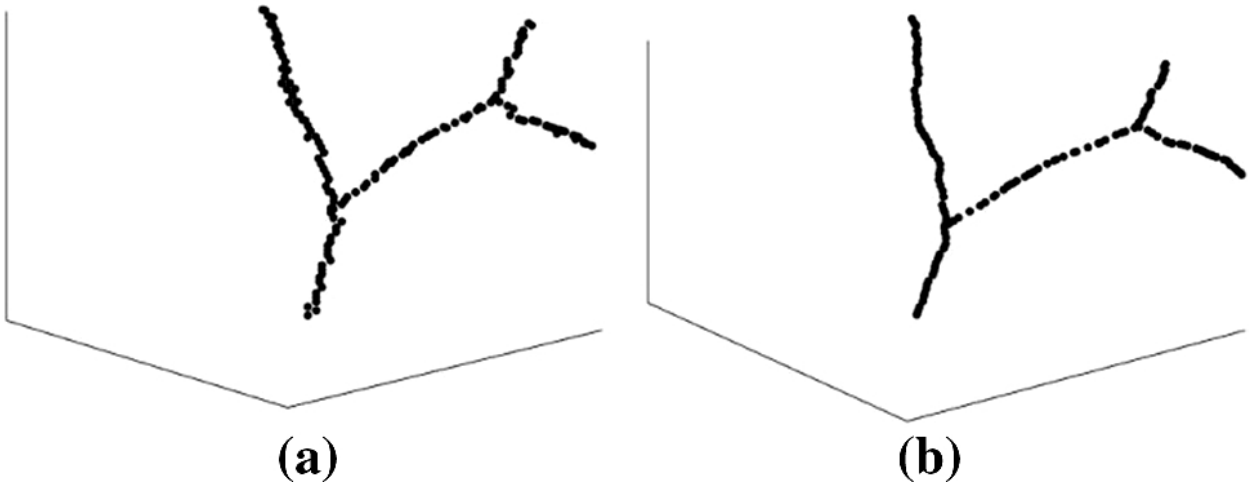

Fig. 4-1: Section of skeleton 3D point cloud (a) before smoothing and (b) after smoothing

4.2.3 Skeleton Point Cloud Smoothing

The algorithm requires a smooth medial skeleton to ensure accurate categorization of points as branch points, bifurcations, etc. A conditional regularization method from Huang et al. was utilized that applies a repulsion force to locally formed skeleton branches to prevent undesirable accumulation[120]. An iterative expression was used to apply this technique so that smoothness and displacement of the skeleton could be balanced. Figure 4-1b shows the same set of points in Figure 4-1a after smoothing with this technique. Execution of three iterations provided a smooth skeleton without significantly moving the skeleton from its initial position. (The mean distance that each point moved was 0.59 mm.).

Following the smoothing process, the skeleton point cloud was ordered. Points were tracked beginning at the top of the trachea by consecutively finding the nearest neighbor. Discontinuities were allowable in the skeleton ordering as only the individual branches needed to be sorted, and a discontinuity would suggest a bifurcation occurred or a terminal branch was reached.

4.2.4 Bifurcation Point Detection

After smoothing, the bifurcation points between branches were identified to find where the branches split. First, each 3D point was grouped with the two previous and two following points of the ordered skeleton. These five points were considered for the condition in Equation 4-1 to test alignment, similar to a method in Huang et al., where x is a point and n is the index of each of the five points[120]. The parameter, γ, is a criterion for alignment (set to -0.8).

$$\cos\left(\angle\left(\overrightarrow{x_n x_{n-1}}, \overrightarrow{x_n x_{n+1}}\right)\right) \leq \gamma \tag{4-1}$$

If all five of these points satisfied the condition, the point was automatically considered a branch point as opposed to a bifurcation point. Example results are shown in Figure 4-2a, where several branch points were removed from the bifurcation point candidate pool, denoted by the green "X" markers, because they did not satisfy Equation 4-1.

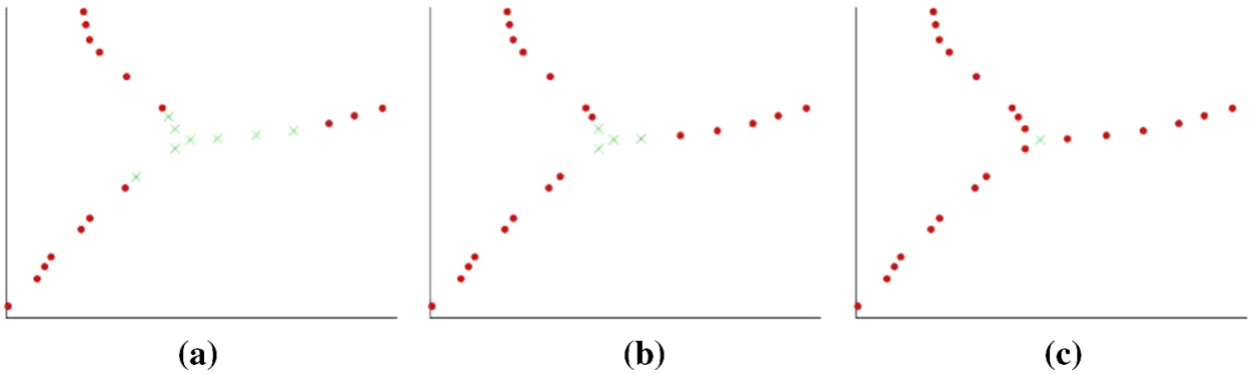

Fig. 4-2: Example of bifurcation identification (a) Candidates (green "X" markers) from alignment criterion. (b) Candidates after angle criterion. c Final bifurcation point (most central point)

To further reduce the number of bifurcation candidates, the candidates were evaluated to find three unique, nearby points that were each at least 25° apart, which would imply that three separate branches connected at that point. If three such points within a small search radius were found, the candidate was kept. However, this would have yielded several results for each bifurcation if the density of points were high. If this were the case, the most central candidate was deemed the final bifurcation point. Figures 4-2b-c demonstrate this process. Figure 4-2b

shows green “X” markers for points whose three nearest neighbors are all at least 25° apart. With several candidates in that small neighborhood, Figure 4-2c shows that the most central point of the group was selected as the bifurcation point in the appropriate location.

4.2.5 Discretization of Individual Lung Branches

The next step was to isolate individual branches so that meshing could be performed carefully along the primary branch axis. Therefore, the bifurcation points needed to be translated into terminal points at the ends of the associated branches. The configuration of terminal points resembled a triangle shape and was treated as such when meshing. Therefore, triangles were fit to every combination of points near the bifurcation. Three chosen points were then optimized such that the most equilateral triangle was formed with the smallest achievable area. Once three points were identified, the points inside the triangle were removed, resulting in three terminal points for every bifurcation, denoting the ends of each branch in the skeleton.

At this stage, the terminal ends of each branch had been identified, but the points that make up each branch had yet to be grouped together so that the entire branch could be isolated for meshing. To group them, the first branch began at the top of the trachea, and the next closest point was chosen and added to its branch. To continue tracking the branch, the next nearest point was repeatedly identified and added to the branch group. This was repeated until at least one of three criteria caused the branch to end: (a) A point, p, was evaluated as existing along the same branch by ensuring that the vector $\overrightarrow{x_{p-1}x_p}$ was less than 90° from the vector $\overrightarrow{x_{p-2}x_{p-1}}$. If the angle was greater than 90°, the branch tracking ended. (b) If the next point in the tracking process was a terminal point, the branch tracking ended, and the detected terminal point began the next branch grouping. (c) If the next point was very far, branch tracking ended.

In each case, a new terminal point was found to begin the next branch. The result was a branch classification for every point on the skeleton.

4.2.6 Radial Point Generation Around Medial Skeleton Points

With the branches isolated, the next step was to form the surface of the geometry around them so that the meshing could ultimately occur along the surface. This task was approached by first creating rings around the skeleton with a fixed radius that could expand to fit to the anatomical surface. To do so, each branch point was considered along with the two neighboring points to fit a line along the branch axis. A series of points were then generated around a circle, centered at the point, with the circle normal axis parallel to the branch axis. The initial circle had a set number of evenly distributed radial points with an equal unit radius. In our current implementation, a set of eight radial points were employed to represent the airway in a single plane. After the unit radial points were generated, the radial axis of each point was projected until it crossed the plane of the surface points. The result of this step was a set of radial points around each branch that could be meshed in careful, consecutive order.

4.2.7 Branch Mesh

For every connection along the branches, a global connectivity matrix mapped the triangulation of the radial points, paired respective of the radial angle, between any pair of subsequent branch points. Isolating the two sets of radial points allowed careful triangulation in a local coordinate frame and avoided kinks or gaps found in conventional automatic meshes. Figure 4-3a-b show a close-up example of the triangulation along a section of one branch, leaving half of the branch unmeshed to demonstrate the approach. With conventional methods, the orientation of these points with respect to their branching nature would be unknown, and if the distance across the branch is similar to the distance between points on the surface, there exists no mathematical

constraint for incorrect triangles (blocks) to not form. This is avoided in our approach with the isolation of and tracking along the branches in this algorithm, as shown in the sample of an 8th generation branch mesh in Figure 4-3c. In figures containing meshes, face colors correlate to superior–inferior position.

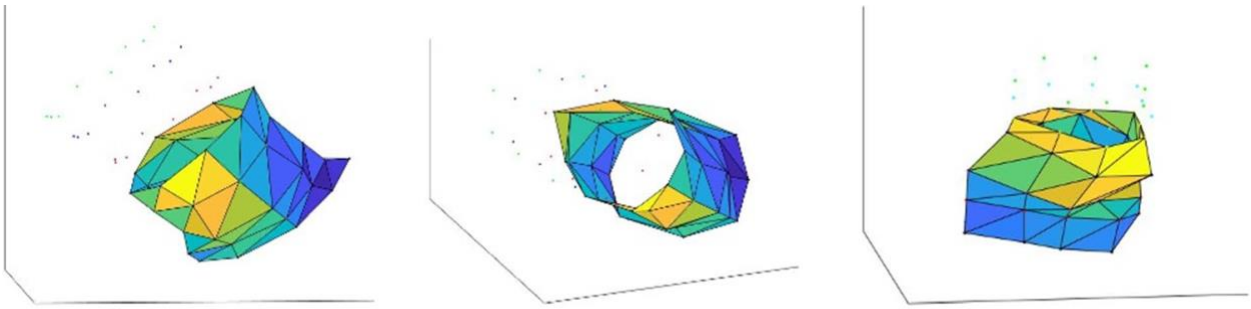

Fig. 4-3: Generated mesh for half of a branch section showing mesh and point cloud (a) Angle to highlight the point-by-point triangulation. (b) Angle to highlight the open airway path. (c) Example of half-meshed branch at the 8th generation

4.2.8 Bifurcation Mesh

Avoiding Branch Collisions: Because the terminal points were identified without considering the surface radii, some circles generated around connecting branches could overlap or interfere. We refer to these instances as *branch collisions*. The terminal points may have been identified very close to the bifurcation point, so building a mesh around them would create triangle edges that intersect the open airways. To consider the interference of radial points around the bifurcation, the search for terminal points was repeated. During this reiteration, when considering the terminal points that fit an equilateral triangle, point combinations were eliminated by testing if the radial points generated around each terminal point would create rings that intersect one another. This added criterion ensured that no airways would be blocked. To execute this intersection test, a perfect circle matching the maximum radius from the

segmentation surface was generated around one of the terminal points. Spheres were generated around the other two with radii matching their maximum surface radii. If the circle intersected either sphere, the point was removed from the terminal point candidates since this meant the branches would collide at these points. This was repeated for each of the terminal point candidates. After removing these terminal point combinations, new terminal points were chosen to optimize the equilateral triangle fit. Essentially, the branches were shortened to avoid overlapping.

Meshing Around Bifurcations: A simplified method was implemented for meshing around the bifurcation features. It was easier to isolate the three terminal points that make up the bifurcation and handle them in their own coordinate system. A unique connectivity map was then applied to the triangulation of these points. An example of the piece that connects the terminal points is shown in Figure 4-4. Three branches are presented while the terminal points are meshed together to form the bifurcation piece. The mesh in Figure 4-4 shows how our algorithm avoided typical leakage from attempting to mesh over these airway features with other approaches.

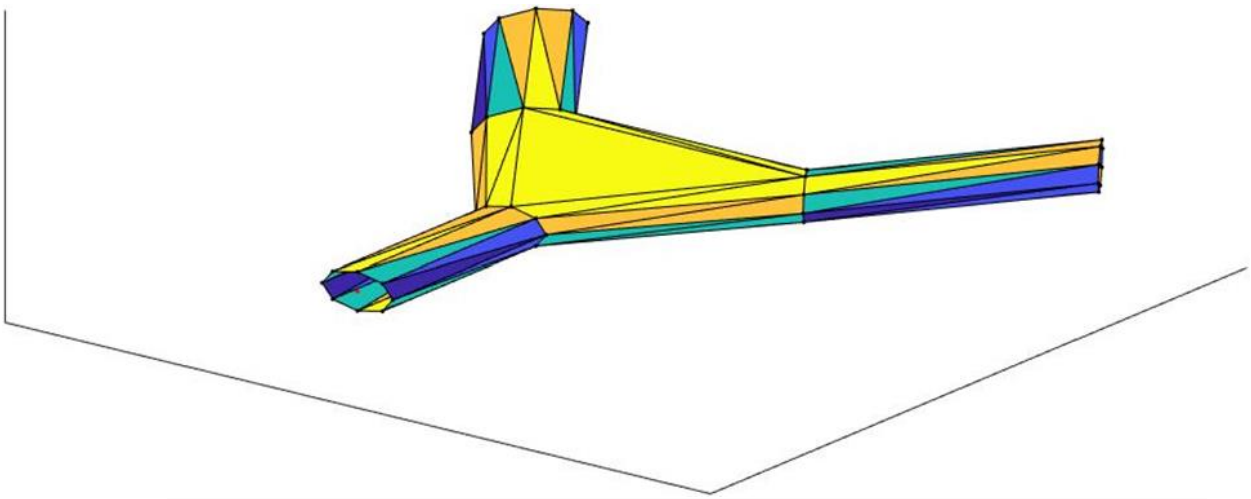

Fig. 4-4: Mesh constructed around isolated bifurcation by connecting terminal points from associated branches

4.2.9 Mesh Quality

Five metrics were calculated to characterize the quality of the resulting mesh. The first was the distance from each mesh vertex to the surface of the original segmentation. The second metric was the distance from each surface point to the nearest vertex, or the reverse of the first metric. This metric describes how well the shape of the resulting mesh reflects that of the original geometry. Another metric calculated was the edge length to report the size of each triangle relative to the voxel size. The two other metrics, skewness and aspect ratio, were calculated to describe the quality of each triangle in the mesh and were calculated using Equations 4-2 and 4-3, respectively, following the established metric formulae[113].

$$skewness = \frac{min(\angle)}{60°} \tag{4-2}$$

$$Aspect\ Ratio = \frac{shortest\ height}{longest\ edge} * \frac{2}{\sqrt{3}} \tag{4-3}$$

4.2.10 Computational Fluid Dynamics Simulations

To demonstrate the compliance of meshes, CFD simulations were run with the smoothed-particle hydrodynamics (SPH) formulation employed in the DualSPHysics software[121]. SPH discretizes continuous Navier–Stokes equations by approximating fluid as a set of material points that interact with surrounding points based on their physical properties. The set of surrounding points are controlled by a smoothing kernel, which is a function of the smoothing length parameter. The theory behind SPH has been extensively described in previous studies that employed the technique to fluid dynamics simulations of air or in anatomical geometries[122,123].

In the simulations used in this study, the only external force applied was gravitational. Air properties were used as provided by the DualSPHysics multiphase low package. The Verlet

time stepping algorithm was used with a minimum time step of 0.01 μs and initial time step of 0.1 μs. The smoothing kernel was set to Wendland[121]. Volume spacing was set to 0.5 mm and the smoothing length was set to √3 mm, which is a function of the volume spacing.

4.3 Results

We first present our results using an ideal model of the lung airway to show how the algorithm works for a simple case. We then present our results using patient-specific lung airways generated from FHFBCT, beginning with one showcased example followed by a summary of the six patients.

4.3.1 Ideal Model Case

Figure 4-5 shows the meshing process for a generic, artificial case. The image starts from a generated 3DCT, shown in Figure 4-5a. Figure 4-5b shows the final mesh for this geometry created from the presented algorithm. With the presented algorithm, there are complete triangles throughout the branches, preventing any potential leakage. There are no twists in the mesh, and no triangulations crossing the diameters or connecting incorrect features. Figure 4-5 offers a clearer look at how well the algorithm performs in simple cases at the 5th and 6th branch generations.

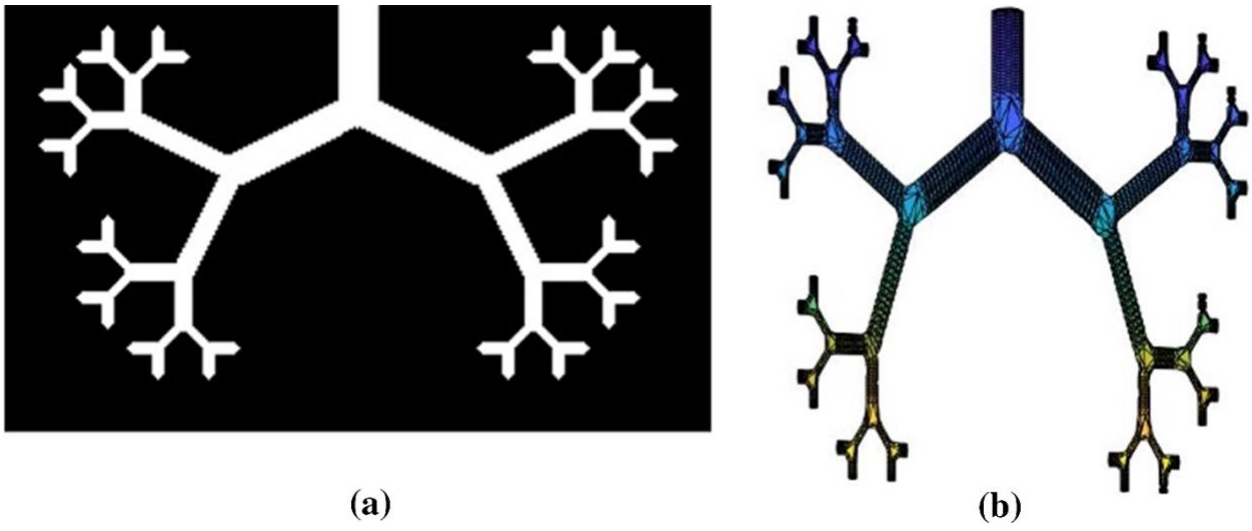

(a) **(b)**

Fig. 4-5: (a) Coronal slice of simplified tracheobronchial model. (b) Completed mesh rendered in MATLAB

The ball-pivoting algorithm (BPA) implementation in MeshLab was used to compare the mesh in Fig. 4-5 to one generated using a state-of-the-art technique using a pivoting ball radius of 3.3785, clustering radius of 20%, and angle threshold of 90°[124]. To exemplify some key discrepancies between the presented mesh and the BPA one, three key examples are shown in Figure 4-6. Figures 4-6a and 4-6c show enlarged regions in the mesh from our algorithm, while Figures 4-6d and 4-6f show the same regions in the BPA mesh. In Figure 4-6d, the red arrows point to three of many holes in this region. The green face color from the opposite side can be notably seen through the hole in the yellow section. These holes would be detrimental to the flow simulations as air would leak out and yield useless simulations. In Figure 4-6e, an error in the mesh at the bifurcation can be seen, exemplifying the trouble these software programs experience with these features, specifically, which are characteristic of the tracheobronchial tree. For use in CFD simulations for interventional procedures, handling these features is highly critical. In Figure 4-6f, more examples of holes and errors at bifurcations are shown at the 5th to 6th generation. These issues occur in even the simplest case, and the lack of any of these errors using our algorithm demonstrates the value of a lung-specific meshing technique.

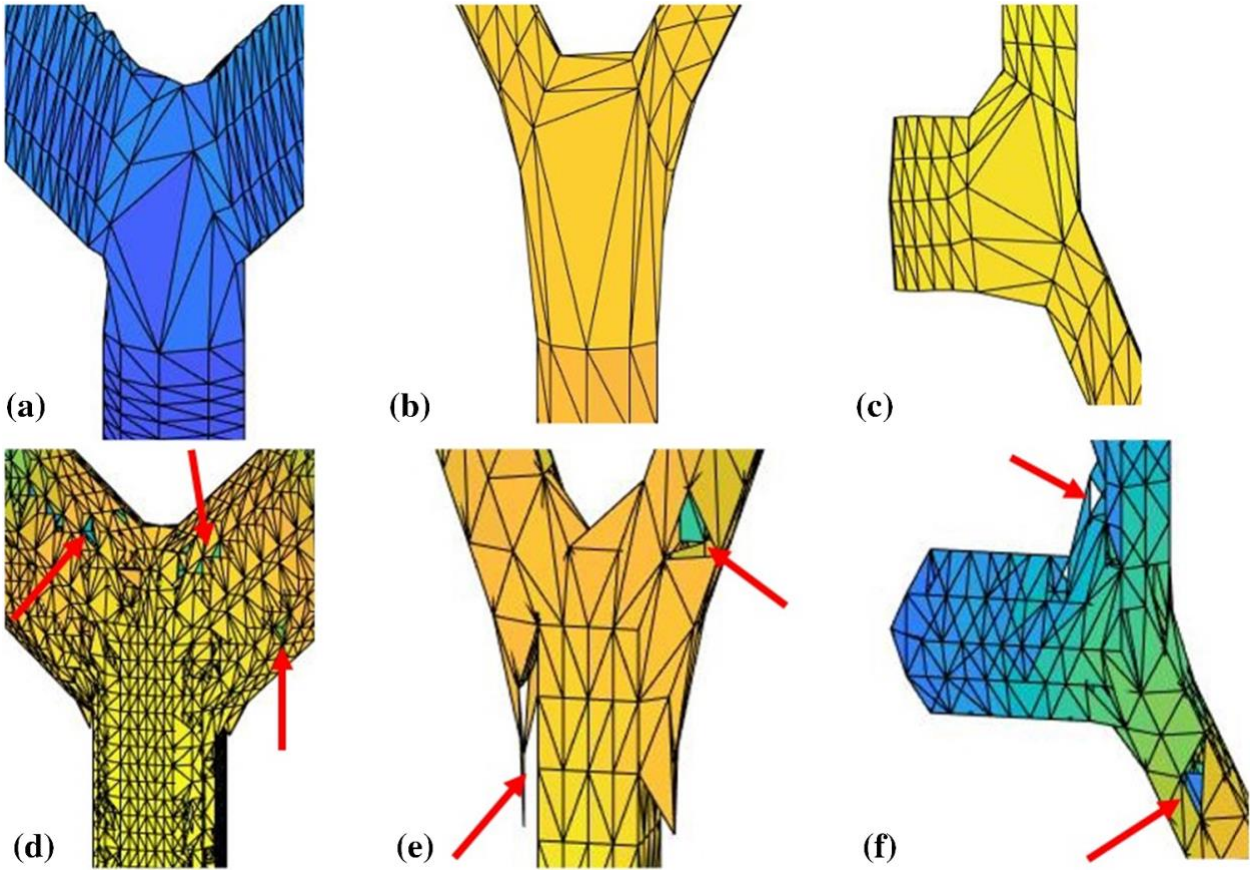

Fig. 4-6: Mesh at first bifurcation with (a) our algorithm presented in this paper and (d) BPA. Bifurcation mesh between 4th and 5th generation branches with (b) our algorithm and (e) BPA. Bifurcation mesh between 5th and 6th generation branches with (c) our algorithm and (f) BPA. Red arrows point to holes or errors in the BPA examples not seen in the examples from our algorithm

4.3.2 Ideal Model Case

Preprocessing and Mesh Result: The results for one patient case are shown in detail. Beginning with the preprocessing, Figure 4-7a shows a coronal slice of the initial CT scan. The segmentation mask of the CT is converted to a skeleton in ImageJ, shown in Figure 4-7b. Figure 4-7c shows the resulting mesh used for CFD simulation.

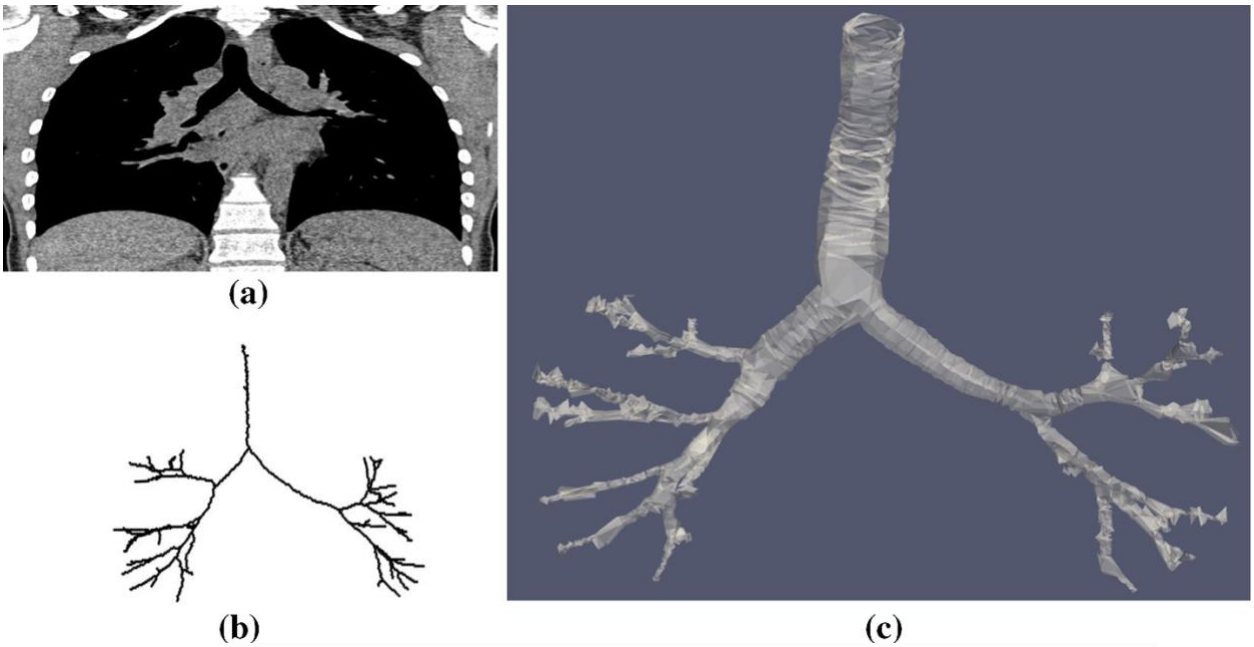

Fig. 4-7: (a) Coronal slice of the original patient CT. (b) 3D point cloud of the raw skeleton. (c) Resulting mesh of airway geometry

Mesh versus State-of-the-Art: To compare specific differences in CFD-compliance between our mesh and current state-of-the-art meshing techniques, three currently used algorithms were employed to model the same geometry. Figure 4-8 shows these meshes. In Figure 4-8a, the mesh using the BPA technique is displayed with the same parameters as previously described. Figure 4-8b shows the resulting mesh from the MC algorithm. The algebraic point set surfaces variant of MC was applied in MeshLab with a filter scale of 3, spherical parameter of 1, and 15 iterations[125]. Notably, the MC method performs well at the trachea and bronchi, but non-physical artifacts appear at higher level branches. In Figure 4-8c, a mesh using CGAL implemented through a MATLAB-based package is shown[126,127]. This mesh provides high-quality meshing elements, but some of the higher generation branches are not able to be meshed. Figure 4-8d shows our mesh, with fewer missing triangles than BPA, fewer exaggerated distal branch artifacts than MC, and greater coverage than CGAL. These

examples show the difference in mesh quality between our algorithm and current ones, as well as some differences in capability through different branch generations.

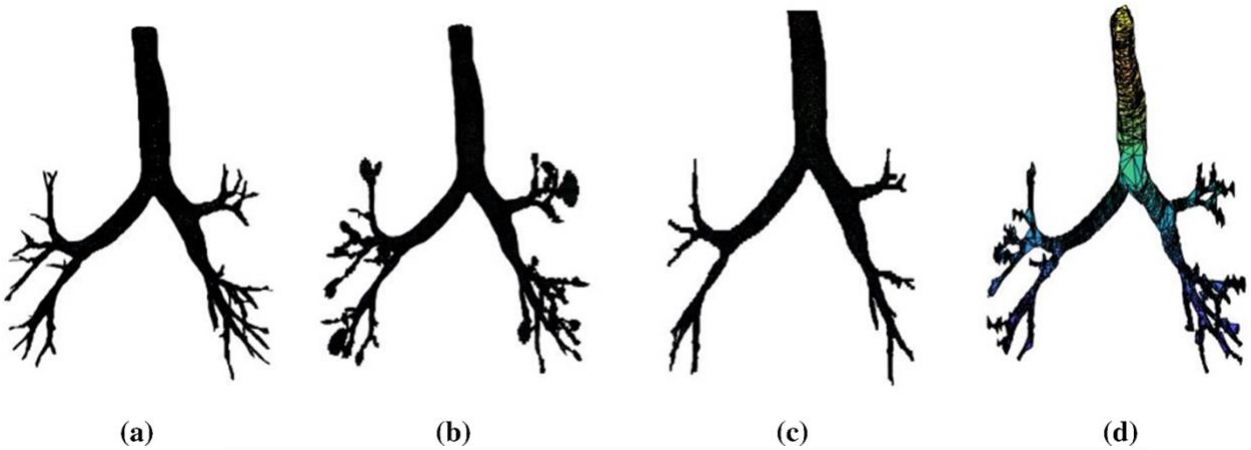

Fig. 4-8: Meshes created with (a) BPA, (b) MC, (c) CGAL, and (d) our algorithm

CFD Airflow Simulations: The value of our method is demonstrated in the presented CFD simulations. To better quantify the meshing errors, we simulated airflow through the airway mesh with generic flow parameters using DualSPHysics[121]. The results of the CFD simulation using the BPA mesh are shown in Figure 4-9a. These results are compared to those resulting from our algorithm in Figure 4-9b. With a specific focus on lung anatomy, our method allows fluid particles to pass properly through as many as five branches of the airways, whereas leakage occurred immediately with the BPA technique. The missing flow through the branch in the right inferior region is due to insufficient flow resolution, as determined by visual inspection of the airway mesh, which was performed for all cases.

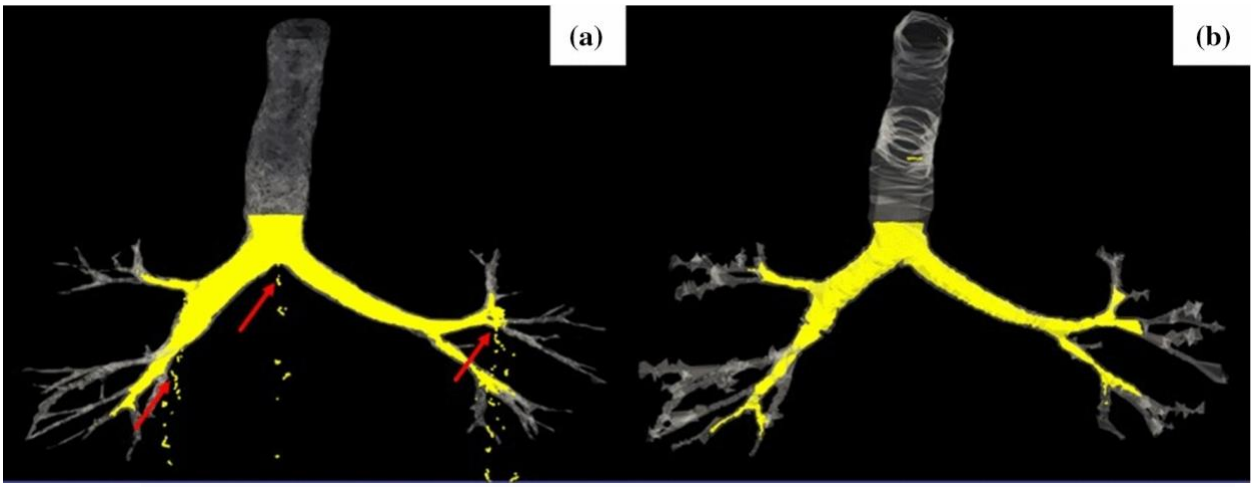

Fig. 4-9: (a) Flow resulting from CFD simulation using the mesh generated with BPA. Arrows denote leakage points. (b) Flow simulation using our method

We show two specific locations where the MC and CGAL meshes failed. First, Figure 4-10a shows one example of a close-up on the leakage from the 3rd to 4th generation bifurcation compared to the non-leaking simulation using our mesh shown in Figure 4-10b. This is as a common problem with generic meshing, where meshing of the bifurcation features leaves holes across from the parent branch. The unique bifurcation feature created in our algorithm makes the problem simpler. Second, Figure 4-10c shows impeded flow in the CGAL mesh due to constricted branches at a higher branch level. Using our algorithm, flow can be reached at the same or greater branching level than the conventional approaches without any leakages or blockages, as shown in Figure 4-10d. This is critical for enabling the use of CFD techniques in a clinical setup.

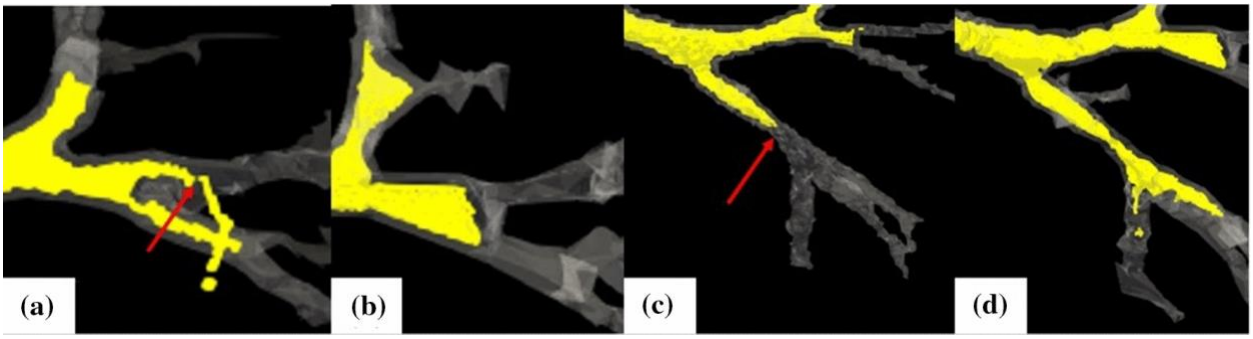

Fig. 4-10: (a) Close-up of leakage (arrow) in MC mesh and (b) repaired leakage using our algorithm. (c) Blocked flow (arrow) in CGAL mesh and (d) extended flow using our algorithm

To summarize, our algorithm was able to take patient lung CT scans and automatically generate airway meshes usable for conducting CFD-based airflow studies.

4.3.3 Mesh Quality

Table 4-1 summarizes the global quality metrics of our mesh and the alternative meshes to compare the quality of the triangles across methods. The table also summarizes the quality metrics for the first three branch levels of our mesh to demonstrate how these metrics change with higher branch generations. Our mesh was on average within a millimeter of the true airway surface demonstrating accuracy to within a voxel. Its mean distance from the vertices to the surface was the least of the meshes except for the BPA mesh, but one aspect of BPA is that no points are created or removed from the point cloud, thus explaining the perfect accuracy. This shows that each vertex in our algorithm accurately reflects a position in the outline segmentation. However, the mean distance from the surface points to the vertices did not perform as well due to the lack of point sampling along branches and the simplistic bifurcation mesh feature. The mean edge length for our mesh was longer than that of the others, giving a quantitative measure of the notably larger meshing elements. However, the minimum edge length was 0.0022 mm, demonstrating that our algorithm is capable of meshing vertices very close together, which is useful at distal branches and if the point sampling were increased. Notably, the CGAL mesh has a high number of vertices, though there is less coverage of higher generation branches, indicating a high resolution of vertices over the first few generations. The skewness and aspect ratio for our mesh were slightly worse than that of the other three. However, the branch-wise qualities show that the metrics improve with increasing branch

level. This is likely due to consistent sampling of radial points with smaller branch radii, thus altering the sampling resolution with increasing branch generation. Moreover, the qualities are relatively low at the bifurcations with values within the range of those for the first three generation branches. This is likely due to the current implementation of the algorithm but could also similarly result from point sampling remaining constant while the radii are different at different levels. Therefore, quality can be improved in the future by making the sampling vary with branch level. The low number of vertices in the mesh resulting from our algorithm relative to the others demonstrates this low sampling that likely explains the discrepancies in other qualities. The number of vertices and distance to vertices are not available for level-wise analysis as these would require associating the original surface to a branch, which is not well defined. These are marked as "N/A" in the table.

Table 4-1: Quality metrics for our mesh and conventional meshes

Mesh	# of Vertices	Distance to Surface (mm)		Distance to Vertices (mm)		Mean Edge Length (mm)	Skew.	Aspect Ratio
		Mean	Median	Mean	Median			
BPA	14208	0.00	0.00	0.04	0.00	2.18	0.44	0.42
MC	22686	0.97	0.54	0.64	0.64	1.45	0.53	0.48
CGAL	20044	0.77	0.67	1.73	0.71	1.14	0.81	0.76
Our Mesh	19397	0.70	0.46	1.81	1.39	1.59	0.63	0.56
1st Level	N/A	0.66	0.42	N/A		6.26	0.17	0.19
2nd Level		0.43	0.42			4.12	0.25	0.27
3rd Level		0.44	0.41			2.71	0.40	0.39
Bifurc.		0.72	0.53			4.98	0.34	0.34

4.3.4 Full Patient Cohort

Five additional patient scan datasets were implemented with our meshing algorithm and the three benchmark algorithms. CFD simulations were performed using all four meshing techniques for each patient case. In all cases, our algorithm provided a mesh that demonstrated CFD-compliance as well or better than the other techniques. Three examples of such scenarios

are included in Figure 4-11. In Fig. 4-11a, a CFD simulation using our algorithm is shown. Figure 4-11b shows an example of a leakage at the red arrow that occurred in the left bronchus of the same patient when meshing with BPA. This same leakage also occurred when using MC. Figures 4-11c, d show an example of a patient case where the flow was blocked from the left bronchus at the red arrow when using MC, but no blockage occurred when using our algorithm. Finally, in Figures 4-11e, our algorithm is shown for a third patient case with extended flow at the two red arrows, compared to the flow using the mesh generated from CGAL. The results from the larger patient cohort support the conclusions from the spotlighted example. When using our algorithm, resulting meshes provide flow through at least as many branches as the comparative methods, which are all standard in anatomy meshing studies.

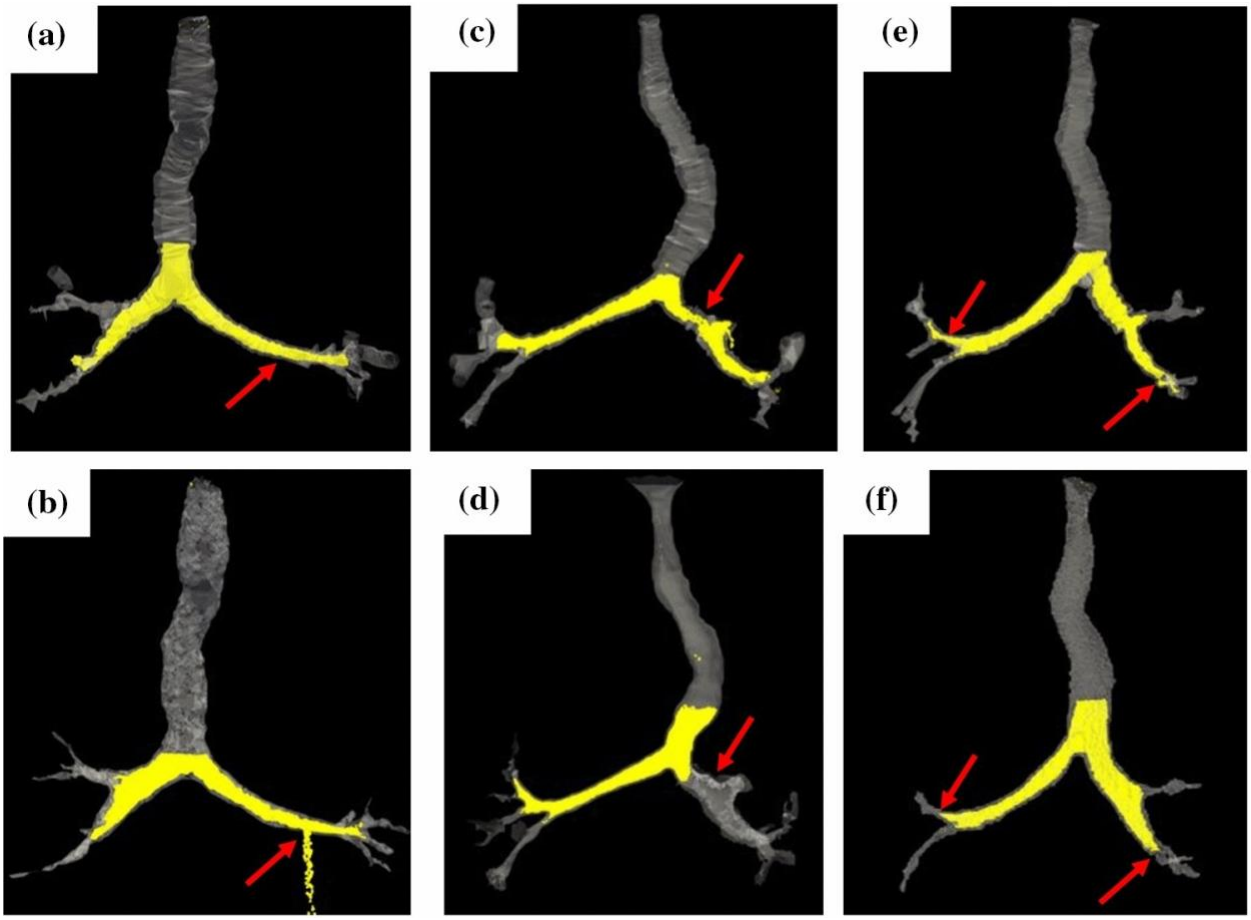

Fig. 4-11: Examples of CFD simulations from additional patient datasets. (a) Our mesh and (b) BPA mesh where our algorithm outperformed BPA. (c) Our mesh and (d) MC mesh

where ours outperformed MC. (e) Our mesh and (f) CGAL mesh where ours outperformed CGAL. Red arrows denote points of interest

Table 4-2 summarizes the meshing element qualities as defined previously. Each entry in the table shows the average value for that quality metric across all patients for the given meshing technique. The results are mostly consistent with the findings from the spotlighted patient case in Table 4-1. When accounting for all patients, both average distance metrics perform better for our mesh than MC and CGAL, which are likely due to the large artifacts in the small airways of the MC mesh and many segmentation points not being represented by the CGAL mesh. An additional metric has been added in the final two columns. These summarize the average minimum branch reached by flow without leaks or blockages, as well as the maximum such branch. These are higher for our mesh on average and are higher or equal to the other metrics in every case.

Table 4-2: Mean quality metrics across patient cohort

Alg.	Mean Distance to Surface (mm)	Mean Distance to Vertices (mm)	Edge Length (mm)	Skew.	Aspect Ratio	Min. Fluid Branch	Max. Fluid Branch
BPA	0	3.80	1.56	0.62	0.54	3.00	3.67
MC	0.88	4.64	1.19	0.53	0.47	2.50	3.50
CGAL	0.67	5.29	0.97	0.80	0.75	2.33	3.33
Our Mesh	0.69	4.16	2.74	0.39	0.39	2.83	3.33

4.4 Discussion and Conclusions

The algorithm presented in this paper focuses on an approach specifically designed for meshing lung airways in a CFD-compliant manner. This sets the method apart from generic meshing techniques because it does not confuse airway features, leave holes in the surface, nor create triangles that cross the airway path and block airflow. The primary goal of this paper is to put forth the importance of managing the careful triangulation along airway features to avoid leakage and blocked flow in subsequent CFD simulations using FHFBCT. This importance has been highlighted by comparing our results to meshes from BPA, MC, and CGAL, which

although they have been used in very recent CFD and meshing studies for airways and vessels, resulted in leakage and blocked flow in several patient datasets[128-132].

The meshing algorithm offers the potential to automatically generate airway meshes, which is valuable in a clinical setting where time is an important factor. There exists a multitude of clinical applications related to the lungs where CFD simulations using such meshes can provide valuable insight. For instance, in the case of COPD management, these CFD simulations could show predicted post-intervention breathing patterns, such as changes in post-operative flow dynamics after bronchodilator administration, or even lobe volume reduction. Having a fast, robust workflow, especially combined with motion and elastography models, would be revolutionary in this line of interventions.

The compliance of our mesh has been demonstrated through (a) lack of blockages and holes that were present in meshes from standard, available open-source software and (b) CFD simulations of airflow, as discretized air volumes were able to travel through as many as five bifurcations without experiencing leakage, compared to conventional methods that leak as soon as the trachea.

In our current implementation, for each airway, we used eight radial points per branch point for simplicity. The number of faces and vertices in the mesh could be easily increased by increasing the number of radial points. Increasing the point sampling of the segmentation outline would further increase the accuracy of the surface geometry and improve the quality. Improvements to the initial airway segmentation and skeletonization would also lead to higher branch generation meshing. Moreover, the bifurcation meshes may be simplistic, but at this point, they show that we can isolate the bifurcation features and automatically generate a consistent mesh around them. Additionally, a simpler, more efficient mesh may provide

computational efficiency in CFD simulations in which every vertex adds additional interactions. In future efforts, these pieces will be tested and optimized to more closely match the anatomical bifurcation features for a large cohort of patients while maintaining efficiency. We will perform a systematic study to evaluate how increasing the segmentation and radial point sampling, developing new connectivity maps, and coordinating different sampling resolutions for different branch levels at the bifurcations all affect the individual mesh element quality.

Future work will involve fine-tuning parameters, improving the initial skeleton quality, and adding additional techniques to increase the extent of successful branch detection and triangulation. The decision to smooth before detecting airway features was consequential of the quality of the skeleton. Our detection algorithm was too sensitive to jaggedness and occasional point inaccuracies. Improved skeletonization would specifically allow for feature detection and tracking before smoothing. This would enable smoothing to be done locally to specific branches for higher quality results, as in previous work with meshing vasculature[133,134].

Several works summarized by Lesage et al. could be adapted from blood vessel segmentation to airway triangulation, such as unique bifurcation detection or similar cross-section-based approaches[111]. There are also many search space parameters in our algorithm to detect bifurcation points, surface points, etc. that can be further optimized to improve results. To improve mesh robustness along the branches, the branch collision process will be applied to all general points. Doing so would help to avoid internal leakage, which is the leakage of particles between two branches that are so close that they are misinterpreted as merging.

Though the isolation of the bifurcations and separate meshing performed in this algorithm contain this issue for five or six generations, higher levels could pose a larger problem.

After applying the branch collision process to all points, more sophisticated efforts to target internal leakage can be adapted from other studies focusing on this issue with implicit surfaces[135,136]. Moreover, the current algorithm uses a simplified approach to controlling the projection of radial points by applying generation-specific radius limits. Regularization would provide a more sophisticated approach to this problem and aid in smoothing the mesh and increasing robustness to inaccurate surface segmentation points. Methods such as fitting circles or ellipses to regularize the radius or providing energy functions to curve tracing provide a roadmap for regularization approaches[137,138].

Additionally, more features and techniques that were the focus of other approaches, such as improving the quality of individual triangles, smoothing the surface mesh, and developing trifurcation detection will be included in continuing efforts. Techniques developed for surface blending, or the use of intermediate surfaces to blend other surfaces of an object, can be incorporated to smoothly join the branch and bifurcation mesh features. These techniques can vary from parametric approaches to neural networks[139-141].

A future study will be conducted to test the CFD-compliance via measure of leakages or blocked flow in the resulting meshes when implementing key techniques from the body of work regarding blood vessel modeling. This study will involve developing an implementation from several works cited in this paper, meshing our patient datasets with those implementations, performing CFD simulations, and quantitatively evaluating the CFD compliance in our patient datasets. This study will help evaluate these methods in terms of

compliance, which was often not the focus of their studies, as well as potentially increase the compliance of our algorithm in certain cases.

The focus of this study was to present our algorithm with an emphasis on the step-by-step approach. The next immediate goal is to perform a careful, phantom-based validation study. Phantoms will be developed with different simulated holes or blockages, and an automatic validation technique will be developed and tested so that the ultimate meshing approach includes automatic hole and blockage detection. Another validation procedure to add in this stage is automatic feedback regarding flow resolution versus blocked flow. Rather than diagnosing the problem via visual inspection, future developments will compare particle size and density to the airway diameter when flow stops to discern flow resolution errors from true blockage due to meshing errors. The following step is to apply the technique to a larger cohort of 40+ patients with COPD and non-COPD cohorts to validate its use across many datasets using the developed automatic validation procedure to minimize error in data analysis. Future studies will also focus on developing a complete CFD workflow with the proper parameters for the case of patient-specific breathing. The ultimate goal is a FSI system with a well-validated biomechanical lung model to combine the effects of tissue elasticity and airflow on one another in a fully integrated, dynamic system. Beyond a lung FSI model, future studies will also include extension of this work into other anatomy with similar structure, such as modeling vessels and blood flow in the cardiac system.

The work in this study has demonstrated that FHFBCT-based geometry can be automatically meshed using a CFD-compliant approach. This is one step towards using FHFBCTs to create comprehensive anatomical breathing models. In the following chapter, other aspects of the envisioned model, including ventilation mapping and elasticity estimation,

were applied using FHFBCT to further demonstrate its capabilities in providing dynamic breathing information for medical purposes. In this chapter, the application in question was CFD modeling for intervention planning. In the following chapter, the applications that benefit from our findings include the same interventions as well as diagnostic potential and overall scientific understanding. However, we used FHFBCT for different modeling approaches and calculations.

CHAPTER 5: CHARACTERIZE THE REGIONAL, LOBE-WISE HETEROGENEITY OF PATIENTS WITH COPD USING CT-BASED VENTILATION MEASUREMENTS

Lobar Heterogeneity of CT-Based Ventilation in Lung Cancer Patients with and without COPD

A version of this chapter is in preparation to be submitted as a manuscript to CHEST

5.1 Introduction

As discussed previously in this dissertation, COPD is the fourth leading cause of death in the United States[11] and the third leading cause of death worldwide[12]. COPD is a heterogeneous disease by nature, including many sub-phenotypes such as emphysema, chronic bronchitis, and asthma-COPD overlap syndrome[142]. However, COPD also presents a high degree of heterogeneity in terms of regional differences[143,144] that have implications for pulmonary function[145].

The effects of regional disease heterogeneity on pulmonary function can impact several pulmonary interventions in terms of decision making and outcomes. One such intervention is lung volume reduction surgery (LVRS), which aims to reduce the volume of a lobe that suffers from air trapping to allow the other lobes to compensate in terms of ventilation[146,147]. Improvements in quality of life have been shown for patients with emphysema compared to traditional therapeutic approaches when LVRS is successful, but the mortality rates are higher when LVRS is unsuccessful[148]. The patient selection criteria for LVRS includes evaluation of emphysema morphology, spirometry, fitness, quality of life, and co-morbidities[149]. Beyond these criteria, an additional analysis of the impact of COPD heterogeneity on pulmonary

function could improve patient selection and decrease the mortality rate, making LVRS a more viable option for patients.

An additional intervention impacted by the heterogeneity of pulmonary function resulting from COPD is BLVR. In BLVR, a duckbill valve is placed bronchoscopically in the airway to occlude the poorly ventilating lobe and essentially mimic the effect of LVRS[150,151]. Like LVRS, BLVR has been specifically noted to suffer from narrow patient eligibility criteria due to limited pre-operative spirometry data used for patient selection[150,152]. To improve these interventions, specifically identified areas of improvement include a comprehensive heterogeneity analysis, improved physiological testing, and further insight into disease characteristics[147,148,151]. Many studies have specifically demonstrated that an analysis of the heterogeneity of lobar disease and function is crucial in selecting patients for these interventions[150,153-155].

Regional ventilation mapping with medical imaging could be a factor in improving these interventions and many others by providing a regional map indicative of pulmonary function, rather than using regional analysis of density-based indicators of emphysema from CT along with a holistic measure of pulmonary function from spirometry. Though not yet clinically implemented, research has already shown the promise of ventilation mapping for such applications as contouring in functional avoidance radiation therapy[156], targeting aerosol deposition in inhaled therapies[157], and diagnosis of pulmonary embolism[158]. Most importantly, early ventilation mapping research has been encouraging for pre-operative evaluation for surgical interventions like lobectomy, LVRS, or BLVR[159].

Previous work in the literature has begun to address the concept of ventilation mapping for surgical applications. Wechalekar, et al. compared lobar distributions of ventilation using a

combination of single photon emission spectroscopy (SPECT) and CT to conventional planar distributions to demonstrate feasibility of using such an approach[159]. Later, Eslick, et al. went on to show that a CT-only based method developed by Guerrero, et al.[160] relating the Hounsfield Units (HU) in inhalation and exhalation breath-hold scans could perform as well as the conventional PET-CT approach[161]. Additionally, this study was able to show differences in the predicted post-operative lung function between the image-based analysis and the conventional anatomical segment counting technique, thus providing evidence of the additional guidance ventilation imaging could bring to surgical decision making.

These studies provide promise for improving outcomes using ventilation mapping, but CT-based ventilation is still an ongoing development effort. This issue of inconsistent approaches to ventilation mapping was best exemplified by the VAMPIRE challenge published in 2018[162]. 50 sets of either 4DCTs or PET/SPECT images were obtained by seven different research groups. Each group then uploaded their calculated ventilation maps or image registrations used to derive ventilation. A high degree of variation was seen between algorithms, imaging modalities, and subjects. The study concludes that this variability, along with a lack of a ground truth, call for further development and validation of ventilation mapping techniques.

The focus of this study is to answer the call for attention to heterogeneity with the promise of CT-based ventilation mapping while also providing a novel approach to ventilation calculation. The goal is to calculate lobar ventilation distributions and document the heterogeneity in patients with and without COPD. We aim to investigate the amount of ventilation heterogeneity across lungs and lobes as well as analyze these heterogeneities in the context of COPD presence and severity.

A unique aspect of this study is found in the ventilation approach, which is a novel technique involving a set of FHFBCTs and two independent methods of calculating lobar ventilation from them. Using two independent methods provides a level of confidence in each in the absence of a ground truth. The use of FHFBCT offers the ability to capture dynamic information as opposed to static breath-hold CT images. FHFBCTs and consequent model-based CT using them also avoid sorting artifacts and shortcomings of the more traditional 4DCT-based approaches[24,163]. Our work therefore provides both novel approaches to ventilation calculation at the lobar level as well as documented characteristics of heterogeneity to inform pulmonary interventions.

4.5 Materials and Methods

5.2.1 Data Acquisition

50 men and women were retrospectively employed for the study. Seven of them had mild COPD, seven had moderate COPD, four had severe COPD, and three had COPD of unknown severity. The rest of the patients did not have COPD, but all 50 had lung cancer that was to be treated using radiation therapy.

For each patient, we acquired 25 FHFBCTs through an IRB approved study, using the same three scanners and scanning parameters described in Chapter 2. As in Chapters 2 and 3, to offer a constant monitor of breathing amplitude and rate, we acquired a breathing signal using a pneumatic respiratory bellows (Lafayette Instrument Company, Lafayette, IN) wrapped around the abdomen during scanning. The bellows was placed around the patient abdomen to maximize the correlation between the bellows signal and the diaphragm motion[59]. The pressure transducer voltage signal was acquired at 100 Hz, and the signal was used to assign each slice a breathing amplitude and breathing rate, the latter determined by the derivative of the

amplitude signal. The bellows signals were synchronized and drift-corrected by maximizing the correlation of the amplitudes to the patient abdominal skin surface motion across the 25 scans as previously demonstrated in O'Connell, et al[34]. The drift-corrected bellows signals were used to define end-exhalation and end-inhalation states as the 5th percentile and 85th percentile amplitudes, respectively. Together, the FHFBCTs and bellows signals supplied the necessary information for both ventilation calculation methods.

5.2.2 Lobe Segmentation

To obtain lobar ventilation calculations, we semi-automatically obtained lobe segmentations using the open-source PTK[164] implemented in Matlab (MathWorks, MA, USA). PTK analyzes both fissure-like structures and vessel wall structures to overcome limitations of other methods. It also applies 3D multilevel B-spline fits to generate smooth fissure boundaries, which helps to overcome fissure incompleteness. In certain cases, corrections were made by medical experts of minor errors in the PTK segmentations. We performed lobe segmentations on the reference FHFBCT scan. Following segmentation, we applied a threshold of -700 HU and ignored voxels above this threshold to ensure that the ventilation data only captured the functional lung parenchyma.

5.2.3 Ventilation Method A: 5DCT-based

In the first method to calculate the lobar ventilation, we employed 5DCT motion modeling[22,25,26,29]. We used the 5DCT model to generate images at end-exhalation and end-inhalation. To calculate ventilation using the 5DCT model, we calculated the ratio of the end-inhalation volumes to the end-exhalation volumes, using the volume ratio to represent the overall lobar ventilation. Though the 5DCT model has been validated and is implemented in our clinic, there are certain assumptions involved that carry over to the ventilation results.

Since there is no ground truth available, we developed a parallel method that does not require generation of a 5DCT model.

5.2.4 Ventilation Method B: FHFBCT-based

This method of ventilation calculation follows the work of Low, et al.[24] In this approach, we used only the FHFBCT scans, their registrations, and breathing amplitudes. To be consistent with the 5D definition of inhalation and exhalation, the amplitudes were normalized such that the 5th an 85th percentile amplitudes were 0 and 1, respectively. The registrations were used to calculate the lobar Jacobians, thus avoiding the assumptions of the 5DCT-based approach in Method A. We registered 24 FHFBCTs to one reference scan for each patient and calculated the voxel-to-voxel Jacobians of each of these registrations.

It is known that the Jacobian operator is prone to large errors as a result of even small registration errors[165,166]. To minimize lobar ventilation measurement errors, we developed a slab-based approach where the voxel-wise Jacobians were averaged over larger slab volumes. Because the scanning protocol was fast enough that neighboring slices had approximately the same amplitudes, we divided the lobes into axial slabs of three slices each and selected the middle slice amplitude to reflect the amplitude of the slab. For each slab, we calculated the mean Jacobian of each registration and considered that the expansion of the slab. Then, we fit the 24 slab Jacobians to the slab breathing amplitude. The slope of the fit, *dJ/dA*, therefore corresponded to the average expansion from end-exhalation to end-inhalation of that slab, i.e., the Jacobian of the slab. Finally, to get the lobar ventilation through this method, we performed a volume weighted mean of the dJ/dA values across the slabs for each lobe. Method A and Method B provided two independent methods of ventilation calculation with only the data and image registrations in common to support the results of both.

5.2.5 Statistical Analysis

We first investigated the agreement between the two ventilation methods at the lobar scale. To do so, we calculated the mean and standard deviation of the discrepancies in lobar ventilation determined by Methods A and B. Discrepancies were calculated as the difference of Method A ventilation minus Method B ventilation. Additionally, we created Bland-Altman plots of the lobar ventilation results measured by each method as well as calculated the correlation coefficients between them to quantify the difference between the approaches.

We used Method A to perform all calculations in the heterogeneity analysis and considered the discrepancy between Method A and Method B to be the margin of error in these results. First, we compared the ventilation of left and right lungs. To analyze the heterogeneity between whole lungs, we calculated the linear fit parameters of the right lung ventilation to the left lung ventilation for each patient. Then, we compared the fit parameters across COPD severity groups. For each patient, we also compared the left and right lung ventilation datapoint to the *identity line*, where the left lung ventilation equals the right lung ventilation. We calculated the length of the normal line from the datapoint to the identity line, defined as η. This was done to quantify the deviation of each patient's ventilation from a perfectly symmetrical relationship between left and right lung ventilation to measure lung ventilation heterogeneity. The relationship between the ventilation datapoint, the identity line, and the normal line, η, is shown in the diaphragm in Figure 5-1. We analyzed η across all patients as well as across COPD severity groups.

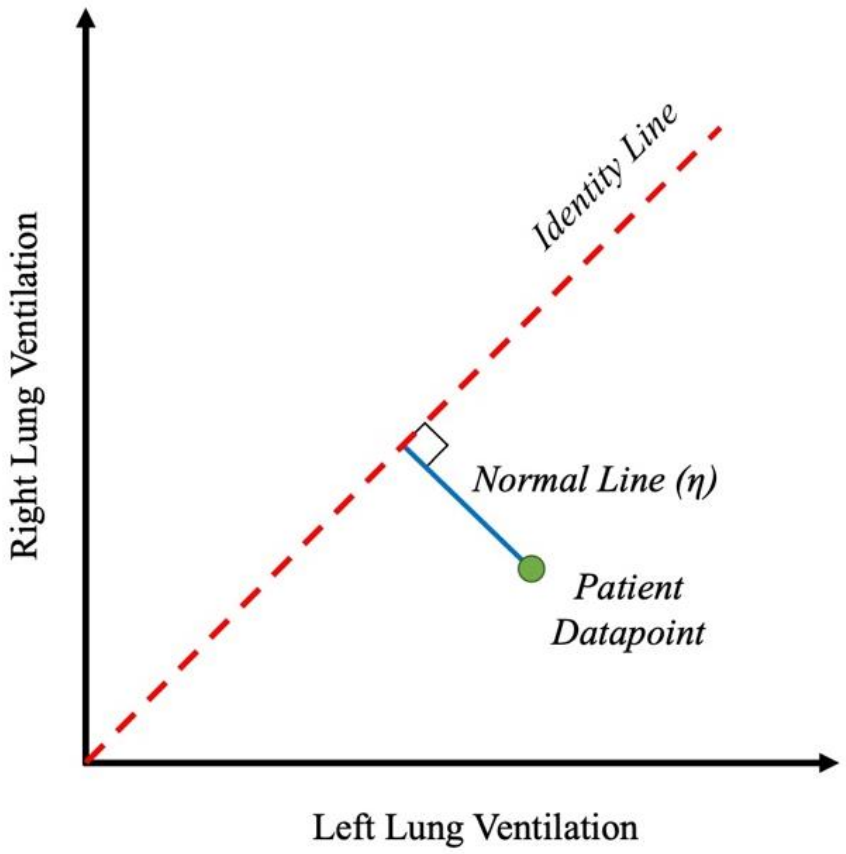

Fig. 5-1: Diagram showing the relationship between the left and right lung ventilation for a given patient, the identity line where left and right lung ventilations are equal, and the normal line, η, extending from the datapoint to the identity line.

We also compared the ventilation between the right upper lobe (RUL) and left upper lobe (LUL), the right middle lobe (RML) and the LUL, and the right lower lobe (RLL) and left lower lobe (LLL) to compare general differences in upper and lower contralateral lobe ventilation across lungs. We then calculated the heterogeneity in ventilation across ipsilateral lobe boundaries. Namely, these included the ventilation heterogeneity between the RUL and RML, the RML and RLL, and the LUL and LLL. To analyze heterogeneity across each lobar comparison, we repeated the analysis performed on the left and right lung data.

Finally, we defined an index to summarize the heterogeneity between the ventilation of the worst functioning lobe and that of the other lobes. This was defined as the *Ventilation Heterogeneity Index (VHI)* and was calculated using Equation 5-1.

$$VHI = \left| 1 - \frac{V_{min} - 0.9}{\overline{V_{\sim min}} - 0.9} \right| \quad (5\text{-}1)$$

In Equation 5-1, V_{min} is the minimum of the five lobar ventilations, and $\overline{V_{\sim min}}$ is the mean of the other four lobar ventilations. Subtracting 0.9 from the lobar ventilation values increased the spread of the index results to obtain a better scalar representation of the lobar heterogeneity. We chose 0.9 because no lobar ventilation was observed to be less than 0.9.

Each measure of heterogeneity (lungs, neighboring lobes, VHI) was compared across COPD severity groups as well as between groups of patients with and without COPD.

4.6 Results

5.3.1 Ventilation Method Consistency

The average discrepancy between results from Method A and Method B across all lobes was -0.0109 ± 0.0397. Figure 5-2 shows a histogram of the ventilation discrepancies between methods for all lobes of all patients.

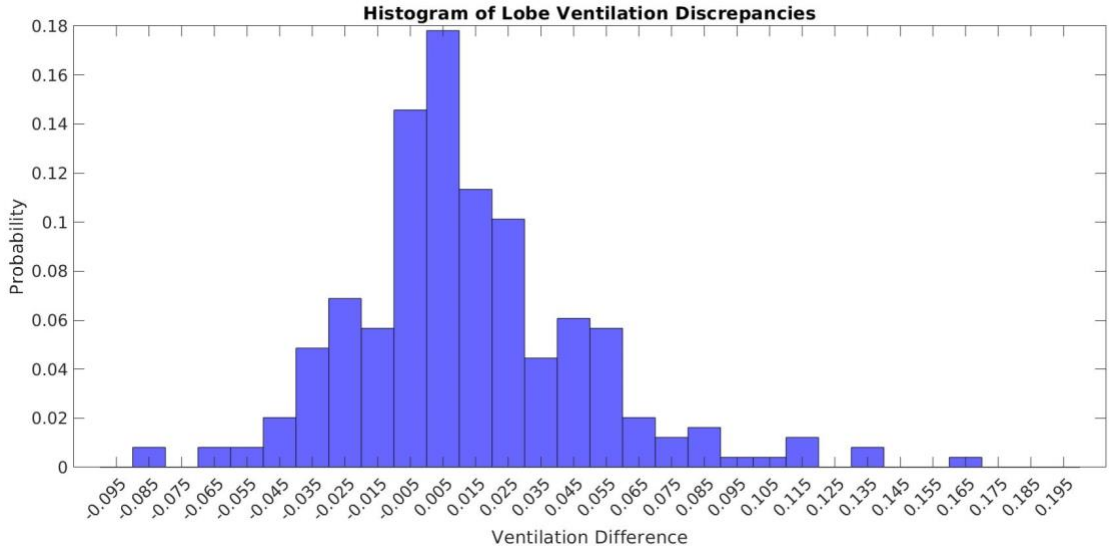

Fig. 5-2: Histogram of the differences between ventilation calculated using Method A and Method B. Differences were calculated as Method A – Method B. Bin labels indicate the center of the bins.

The first column of Table 5-4 shows the mean differences between ventilation calculated using Method A and Method B for each COPD severity group as well as patients with and without COPD. There was no dependency of ventilation discrepancy between methods on COPD severity.

Figure 5-3 shows the Bland-Altman plot of the ventilation differences between Method A and Method B color coded by COPD severity. As shown in the plot, the repeatability coefficient (RPC) was 0.07, indicating that the absolute difference between the two methods would lie within 0.07 with 95% confidence[167]. The coefficient of variation (CV), or the standard deviation as a percent of the mean, was 3.3%. The mean difference of -0.01 was statistically significant ($p < 0.01$), showing that the methods agreed well on average. Figure 5-3b shows the correlation plot of Method A and Method B for all lobes with an R^2 value of 0.74.

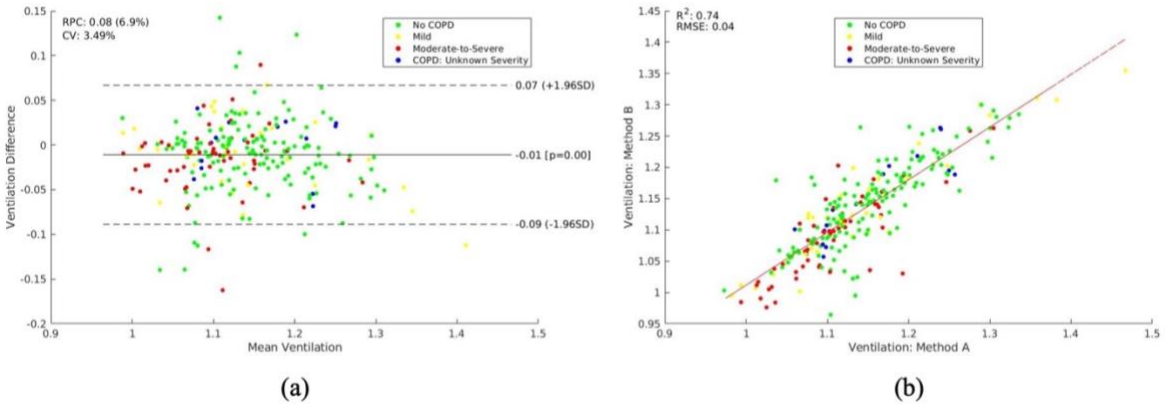

Fig. 5-3: (a) Bland-Altman plot of the mean ventilation calculated using Method A and Method B. The mean and 95% confidence interval (1.96 * standard deviation) lines are shown. (b) Scatter plot of ventilation calculated with each method. Color indicates COPD severity in both plots. The red line represents the fit line with a slope of 0.84 and y-intercept of 0.17.

5.3.2 Left vs. Right

The ventilation between the left and right lungs were typically about the same as indicated by the mean ratio of left lung ventilation to right lung ventilation across all patients, which was 1.00 ± 0.032. There was also very minimal difference in the left lung to right lung ratio between patients with and without COPD. The left-to-right lung ventilation ratios for all COPD severity groups are shown in the second column of Table 5-4.

Figure 5-4 shows scatter plots of the left and right lung ventilation for all patients, color-coded to indicate COPD severity. The error bars on the plot indicate the discrepancy in the two ventilation calculation methods, considered to be the minimum measurement error. The black solid line represents the identity line where the left lung ventilation is equal to the right lung ventilation. The green, yellow, and red lines show the linear fits of the groups of patients with no COPD, mild COPD, and moderate-to-severe COPD, which had slopes of 0.635 (R^2 = 0.719), 0.728 (R^2 = 0.866), and 0.720 (R^2 = 0.746), respectively. Each of these relationships showed a consistent trend towards higher ventilation in the left lung than in the right lung in each COPD severity group.

The datapoints in Figure 5-4 with left lung ventilations between 1.10 and 1.25 appeared to lie closer to the identity line, while values outside this range seemed to drive the slopes to show a bias towards the left lung ventilation. Therefore, lung ventilation heterogeneity may be more common in cases with either high or low overall ventilation than in cases of more moderate ventilation.

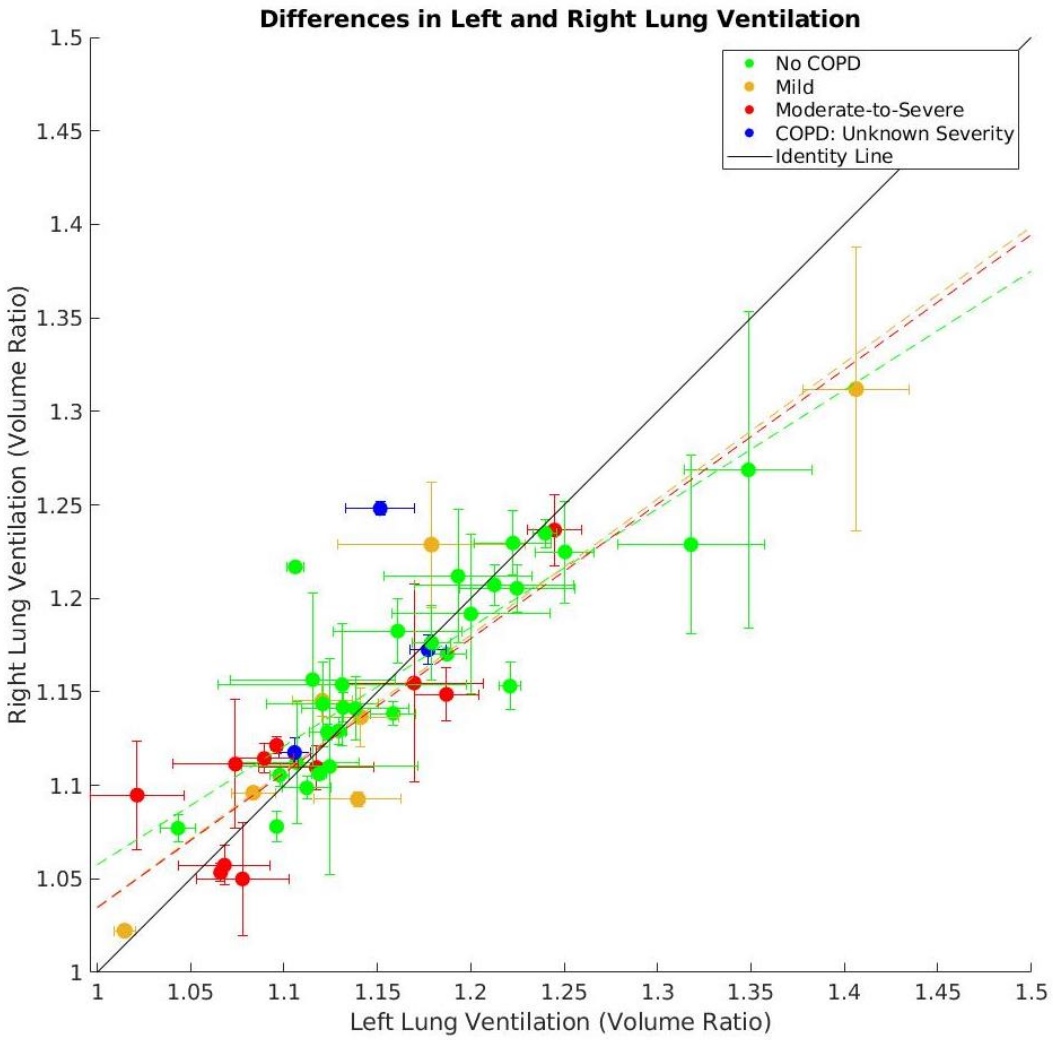

Fig. 5-4: Scatter plot of the left and right lung ventilation using Method A. The black solid line represents the identity line. The other dashed lines show the linear fit lines for each severity group. Color indicates COPD severity for data points and fit lines. Error bars represent the difference between Method A and Method B for the given datapoint.

Figure 5-5 shows histograms of the η values calculated from the data in in Figure 5-4 to quantify how often there was asymmetry in left and right lung ventilation. Figure 5-5a shows these histograms for different COPD severity groups. Figure 5-5b shows them for all patients and patients with and without COPD. In general, there is enough variability in η in all cases that one should analyze the left and right lung heterogeneity while planning relevant interventions. There may be some evidence of an increase in η in patients with COPD as

indicated by the increasing mean η shown in each plot. There also appears to be evidence of higher η in patients with mild COPD relative to both patients without COPD and patients with moderate-to-severe COPD.

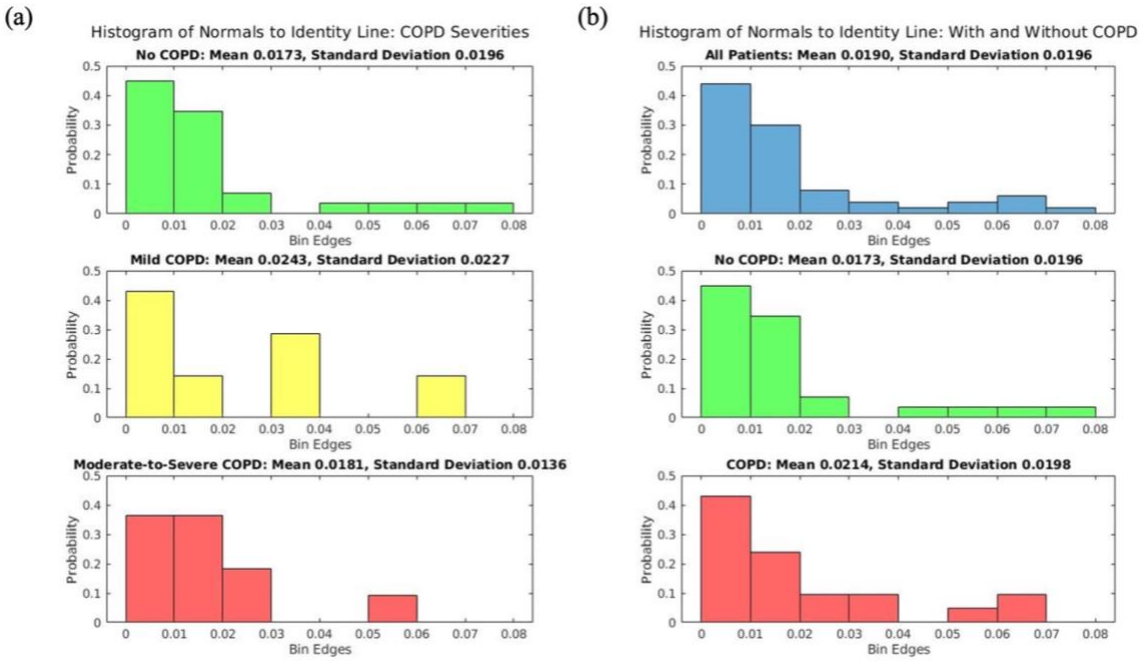

Fig. 5-5: Histograms of η from left and right lung ventilation datapoints to the identity line. (a) From top to bottom, histograms include η for patients with no COPD, mild COPD, and moderate-to-severe COPD. (b) From top to bottom, histograms include η for all patients, patients without COPD, and patients with COPD. All histograms are shown as probabilities, or the number of counts in each bin relative to the total counts.

5.3.3 Lobar Heterogeneity

Figure 5-6 shows scatter plots of the upper and lower contralateral lobe pairs, including comparisons of the RUL to the LUL, RML to the LUL, and RLL to the LLL. The fit lines show linear fits to the data for each COPD severity, along with the black dashed identity line, as in Figure 5-4. These slopes are tabulated in Table 5-2 along with the associated R^2 values. In each comparison, the ventilation was generally symmetrical. However, the RML/LUL and RLL/LLL fits for patients with moderate-to-severe COPD had poor correlations, thus indicating a high level of variability in these cases.

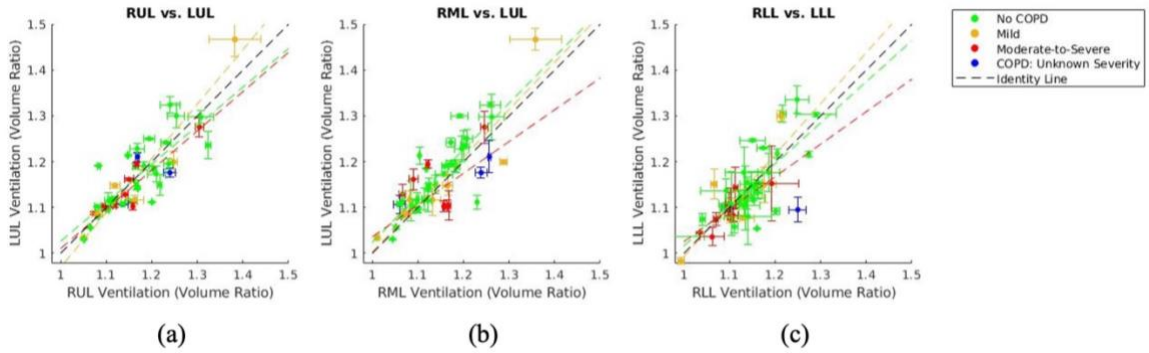

Fig. 5-6: Scatter plot of the upper and lower contralateral lobe pair ventilations using Method A. (a) Scatter plot of the RUL vs LUL ventilation. (b) Scatter plot of the RML vs LUL ventilation. (c) Scatter plot of the RLL vs LLL ventilation.

Figure 5-7 shows scatter plots of the ventilation for the three ipsilateral lobe pairs (RUL/RML, RML/RLL, LUL/LLL). These relationships were much more variable than the upper and lower contralateral lobe pairs. The RUL vs RML slope for patients with mild COPD showed a generally symmetrical relationship. The other fits with R^2 values above 0.500 showed much more heterogeneous ventilation, particularly in the RUL vs RML slopes for patients with no COPD and moderate-to-severe COPD. Additionally, several relationships had very low R^2 values (< 0.500), thus implying a high level of ventilation heterogeneity variability.

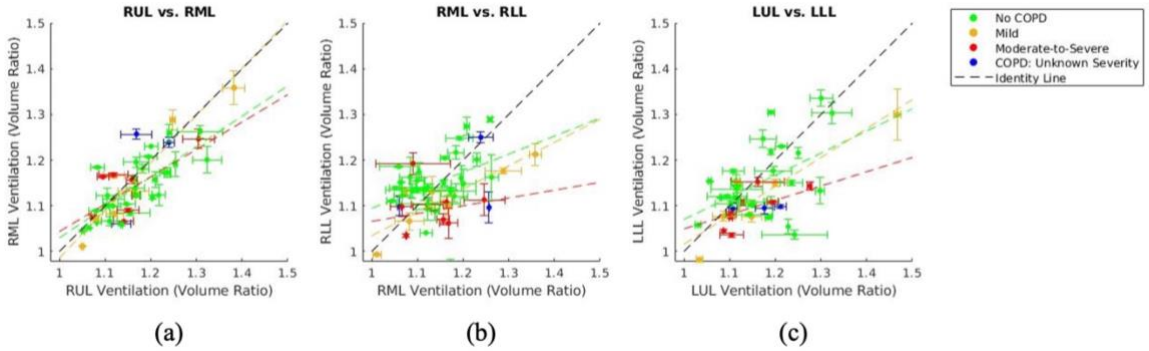

Fig. 5-7: Scatter plot of the ipsilateral lobe pair ventilations using Method A. (a) Scatter plot of the RUL vs RML ventilation. (b) Scatter plot of the RML vs RLL ventilation. (c) Scatter plot of the LUL vs LLL ventilation.

Table 5-2: Slopes of the ipsilateral lobe ventilation relationships. R^2 values in parentheses.

Lobe Combination	No COPD	Mild COPD	Moderate-to-Severe COPD

RUL vs LUL	0.841 (0.627)	1.19 (0.916)	0.857 (0.830)
RML vs LUL	1.01 (0.695)	1.03 (0.821)	0.694 (0.345)
RLL vs LLL	0.896 (0.555)	1.11 (0.673)	0.701 (0.387)
RUL vs RML	0.666 (0.580)	1.04 (0.915)	0.599 (0.566)
RML vs RLL	0.395 (0.144)	0.510 (0.775)	0.171 (0.0502)
LUL vs LLL	0.484 (0.220)	0.632 (0.846)	0.312 (0.181)

Table 5-3 shows the means and standard deviations of η for each of the interlobar fits in different COPD severity groups shown in Figures 5-6 and 5-7. On average, η was higher for the ipsilateral lobes than for the upper and lower contralateral lobe relationships across all severity groups. The relationship with the lowest mean η was the RUL and LUL correlation among patients with mild COPD. Across all groups, the RUL and LUL showed lower η values than the RLL and LLL on average, implying a stronger correlation between the upper contralateral lobes than between the lower contralateral lobes. The lobe ventilation relationship between the RML and RLL in patients with moderate-to-severe COPD had the highest η on average, implying these lobes showed the greatest ventilation heterogeneity variability. In general, across all groups, the RML and RLL had the highest mean η and therefore the highest variability in ventilation heterogeneity.

Table 5-3: Mean and standard deviation of η for each lobar combination

	Upper and Lower Contralateral Lobes			Ipsilateral Lobes		
COPD Severity Group	RUL vs LUL	RML vs LUL	RLL vs LLL	RUL vs RML	RML vs RLL	LUL vs LLL
No COPD	0.0232 ± 0.0191	0.0265 ± 0.0225	0.0261 ± 0.0220	0.0277 ± 0.0196	0.0410 ± 0.0274	0.0401 ± 0.0356
All COPD	0.0238 ± 0.0200	0.0326 ± 0.0230	0.0286 ± 0.0300	0.0307 ± 0.0230	0.0446 ± 0.0330	0.0431 ± 0.0362

Mild COPD	0.0205 ± 0.0139	0.0246 ± 0.0271	0.0304 ± 0.0241	0.0296 ± 0.0213	0.0383 ± 0.0147	0.0410 ± 0.0349
Moderate-to-Severe COPD	0.0236 ± 0.0250	0.0365 ± 0.0232	0.0249 ± 0.0254	0.0292 ± 0.0232	0.0472 ± 0.0370	0.0429 ± 0.0403
All Patients	0.0235 ± 0.0193	0.0290 ± 0.0227	0.0271 ± 0.0254	0.0289 ± 0.0209	0.0425 ± 0.0296	0.0414 ± 0.0355

The mean VHI for all patients was 0.238 ± 0.162. The moderately high mean VHI demonstrates that ventilation is typically present across patient lobes. However, the standard deviation was 68% of the mean value, showing a high level of variation of lobar heterogeneity across patients. The third column of Table 4 summarizes the mean VHI for each COPD severity group. The mean VHI is higher in each COPD group than in the group without COPD. This implies a higher level of interlobar heterogeneity in cases of COPD.

Table 5-4: Ratios of left lung ventilation to right lung ventilation for COPD severity groups

COPD Severity Group	Mean Ventilation Discrepancy	Mean Left to Right Lung Ratio	Mean VHI
No COPD	-0.0100 ± 0.0413	1.00 ± 0.0309	0.213 ± 0.150
All COPD	-0.0122 ± 0.0374	0.996 ± 0.0347	0.272 ± 0.175
Mild COPD	-0.0098 ± 0.0390	1.01 ± 0.0390	0.268 ± 0.197
Moderate-to-Severe COPD	-0.0166 ± 0.0376	0.997 ± 0.030	0.301 ± 0.180
All Patients	-0.0109 ± 0.0397	1.00 ± 0.0323	0.238 ± 0.162

4.7 Discussion and Conclusions

COPD is a common and deadly disease that requires further research for improving treatments and interventions. Two such interventions include LVRS and BLVR, which both stand to benefit from improvements in patient selection and decision making. An analysis of lobar

heterogeneity of lung function could be one key contributor to these improvements. In this study, we provided a CT-based analysis of ventilation heterogeneity across both lungs and lobes to provide documented trends and guidance for future interventions.

We used 5DCT modeling to calculate ventilation to study its heterogeneity across lungs and lobes. Because there was no ground truth, we designed a second independent method to ventilation calculation based solely on the FHFBCTs and the acquired breathing signal, essentially removing an intermediate modeling step and creating an alternative formulation of the ventilation calculation. While comparing the results from these two methods offered a measure of confidence in the results, focusing on ways to further improve their individual accuracy will be helpful in supporting future studies. This could be done by improving deformable image registration accuracy, reducing motion blur in the CT scans, and further developing the 5DCT modeling approach.

Using our approaches to measure the heterogeneity between left and right lung ventilation showed that there was typically asymmetry between the two, as was the case in all COPD severity groups, with a bias toward higher ventilation in the left lung in cases of particularly high or low ventilation. Calculating fit lines of left-to-right lung ventilation showed that the COPD severity groups did not have notably different relationships between left and right lung ventilation. While the relationships may be similar, there was evidence that an increase in variation may arise with an increase in COPD severity, as indicated by the histograms of the η values in Figure 5. Future work should include a larger cohort with more patients with COPD to determine the significance of this trend. Additionally, other factors, such as age, sex, and comorbidities should be analyzed with heterogeneity to see if there may be other predictors in future work.

The lobar heterogeneity analysis showed that there were typically good relationships between the upper lobes and between the lower lobes. However, when analyzing the three sets of adjacent lobe pairs, there was a much higher degree of heterogeneity. Not only was there more heterogeneous behavior in the ventilation of these lobes, but the variability in the data also increased as indicated by η, and these relationships were generally less predictable. This supports the need to acquire and analyze these data when planning surgical interventions or other pulmonary treatments that could be affected by the ipsilateral lobes.

A larger question that demands further research is in determining the best way to define heterogeneity. In this study, we compared ratios of ventilation as well as developed an index, the VHI, to offer a concise metric. There may be better definitions based on physiology, normal trends in larger datasets and deviations from those trends, or just more comprehensive definitions. The more ways we can describe heterogeneity, the more we can learn about these differences in ventilation and incorporate the findings into interventional planning.

We used FHFBCTs to ensure that we captured free-breathing dynamics in our data and analysis. However, there were only FHFBCTs available for these patients, so a direct comparison to how the results may look from residual volume (RV) and total lung capacity (TLC) scans has yet to be accomplished. In future studies, we will expand data collection to add RV and TLC scans to our FHFBCTs so that comparisons against more common ventilation methods can be made. This will require a reduction in scanning dose, so prospective gating and other dose-reduction techniques, like reducing the number of scans or adjusting the scan parameters, will need to be developed to enable this future study.

In conclusion, we have used two unique CT-based ventilation calculations to measure ventilation in patients with varying severities of COPD. We have documented the differences

in ventilation between left and right lungs as well as across different lobar combinations. We have found that the variation in these relationships calls for close attention to ventilation patterns in patients to best inform surgical decision making or any other treatment planning concerned with lung function performance.

In the next chapter, our motivation is the same, but we focus on a different biomarker for lung function: tissue elasticity. Since our elasticity measurements were based on a validated biomechanical model, we can emphasize a voxel-by-voxel analysis, unlike the work in this chapter, which was limited to a lobar analysis. We also include a lobar analysis in Chapter 6 since it is relevant to the surgical interventions discussed.

CHAPTER 6: CHARACTERIZE THE REGIONAL, LOBAR HETEROGENEITY OF PATIENTS WITH COPD USING ELASTICITY AND PARAMETRIC RESPONSE MAPPING

A Systematic Analysis of the Regional Heterogeneity in Tissue Elasticity Distributions and Parametric Response Mapping in Lung Cancer Patients with COPD

A version of this chapter has been submitted as a manuscript to Medical Physics

6.1 Introduction

In Chapter 5, we employed ventilation as a key biomarker for lung function. While the studies of functional tissue mapping using ventilation discussed in that chapter are promising, accurately calculating ventilation from CT is still an ongoing effort[24,162,168,169]. Many of the developed approaches in previous research incorporate transformation-based calculations, or calculations based on a mapping of CT images, both of which rely on the accuracy of deformable image registration. It has been shown that the even small errors in the image registration can cause much larger errors in ventilation calculations[165,166]. For this reason, we devised our lobar analysis. However, if accurate results are desired on a voxel-by-voxel scale, it may be beneficial to explore other functional properties to guide surgeries or radiotherapy until image registration can be performed with sufficient accuracy for these calculations.

In this study, we propose elasticity as an additional functional property that can be analyzed regionally from end-exhalation CT. Tissue elasticity is a biomechanical property that describes tissue stiffness[170]. Elasticity can be calculated from medical images in several ways. In this study, it is done so with the HU from the end-exhalation image and the DVF mapping to end-inhalation. These inputs are provided to an iterative model that estimates the Young's modulus (YM) of each voxel to represent the elasticity, as has been validated in previous work[96,170,171].

Since elasticity is calculated with a physics-based model, it can be calculated on a voxel-by-voxel basis. Reduced elasticity is indicative of lung disease, so it can be another regional marker for COPD. Previous work showed that elasticity of voxels in the 1-3 kPa range was a better biomarker for COPD than the traditional RA950[172]. CT-based elasticity measurements thus offer an additional way to characterize regional lung function based on CT.

Another established quantitative CT-based technique for the regional characterization of lung disease is the parametric response mapping (PRM) approach which links the end-exhalation image to the end-inhalation image to categorize voxels into emphysema, functional small airway disease (fSAD), or normal tissue categories based on their HUs[173-176]. This technique has been shown to be a good biomarker for COPD, and thus has been used in this study to quantify the disease state of each voxel in CT images.

The heterogeneity of lung function is of particular concern because, as mentioned previously, COPD is such a heterogeneous disease[142,143,145]. LVRS, BLVR, and other lung interventions depend on disease heterogeneity to ensure that lung function can be compensated post-intervention[177,178]. Lung radiotherapy depends on heterogeneity to define functional subregions[179,180]. Studying the patterns of disease heterogeneity can help these medical approaches take advantage of a key characteristic of COPD to improve outcomes.

In this chapter, we statistically characterized the regional lung function heterogeneity in lung cancer patients using both PRM and tissue elasticity. All properties were CT-based and were applied along with lobe segmentations to obtain lobar distributions. Lobar distributions were calculated and analyzed to offer an analysis specifically relevant to lobar interventions. The statistical results were therefore divided based on the lobe volumes and underlying COPD severity. Additionally, interlobar heterogeneity of elasticity was analyzed to provide insight

for regionally defined treatments such as radiotherapy. By investigating the lobar heterogeneity of these properties, we have shown evidence of how assessing tissue elasticity heterogeneity could benefit surgical or radiotherapy planning for patients with all levels of COPD.

6.2 Materials and Methods

6.2.1 Data Collection

For this study, we retrospectively employed 23 of the 5DCT patients described in Chapters 2 and 5. To perform lobar HU-based and biomechanical property measurements, end-exhalation and end-inhalation images along with their corresponding DVF needed to be generated. We selected the 5th and 85th percentile amplitudes with zero flow to represent end-exhalation and end-inhalation respiratory phases as shown in previous studies[22]. The tissue-specific 5DCT motion parameters were used to deform the reference image to its position in the end-exhalation and end-inhalation breathing phases.

The end-exhalation and end-inhalation scans were deformably registered separately to obtain the DVFs. The registration technique pTVreg was used to register the images and resulted in DVFs pointing from end-exhalation to end-inhalation. This method has been previously shown to be successfully used for end-exhalation and end-inhalation registration tasks[39]. This technique uses isotropic total variation regularization to accurately register sliding interfaces and avoid physically implausible DVFs[38]. This resulted in a voxel-by-voxel deformation vector field in the end-exhalation geometry.

6.2.2 HU Correction

Currently, the 5DCT approach does not have a correction to the HU based on changes in air content at different breathing states. To calculate the HU-based PRM properties, we added such a correction to the 5DCT process to scale the HUs according to the HUs sampled in the

25 scans. We employed a ventilation-based HU correction that was recently published by Low et al.[24]. In this method, the voxel locations were tracked across the 25 FHFBCTs. The associated HU values were then linearly fit to the breathing amplitudes. This resulted in a correction factor for each voxel that allowed an adjustment of the reference CT HU to the HU at end-exhalation and end-inhalation amplitudes.

6.2.3 Lobe Segmentation

To analyze lobar statistics of HU-based and biomechanical properties, we generated lobe masks that grouped lung voxels into one of the five lung lobes. We performed lobe segmentations semi-automatically on the FHFBCT reference scans using the open-source software Pulmonary Toolkit (PTK). The software first built a lobar approximation, then applied a "fissureness" filter, and finally fit a smooth multi-level B-spline curve through the fissureness and extrapolated to the lung boundaries to create the lobe segmentation[164]. In some cases, the automated segmentation results experienced minor errors, so manual corrections were made using the graphical user interface in PTK and verified by medical experts. An example of a coronal slice from a patient CT is shown in Figure 6-1a with the corresponding lobe mask in Figure 6-1b. The CT shown is the reference image used for modeling and was therefore deformed along with the mask to obtain end-exhalation and end-inhalation images and masks.

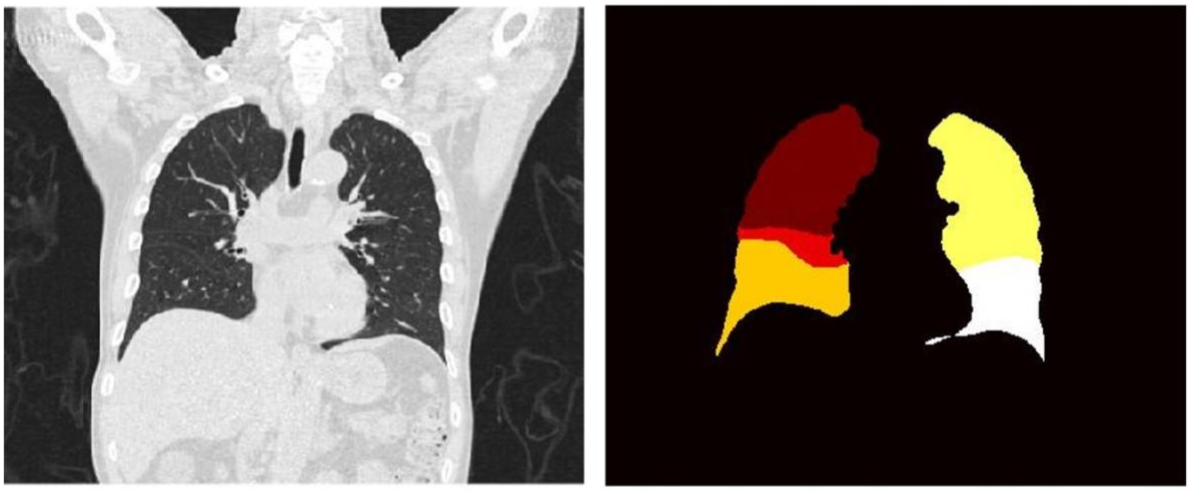

Fig. 6-1: (a) Example of coronal slice from a FHFBCT scan used as the reference scan for modeling and (b) corresponding lobe mask from PTK[164]

To only include lung parenchyma in the analysis, we removed blood vessels from the segmentations by excluding voxels with greater than -700 HU. This threshold was chosen based on the HU distribution found in the lungs of clinical CT scans in a published study[181]. Our focus was only on the functional lung parenchyma. For example, blood vessels do not expand or ventilate during respiration and have very high elasticity, so their values would misrepresent the lung parenchyma distributions. We used the binary lobe masks to analyze the HU-based and biomechanical properties of the segmented lobes. Therefore, our analysis only pertained to the parenchymal tissue with HU less than -700 in 5th percentile images.

6.2.4 Parametric Response Mapping

With the HUs in end-exhalation and end-inhalation, we categorized voxels based on the published PRM techniques[173,174]. For each voxel, we considered the HU in the end-exhalation and end-inhalation images and categorized voxels into emphysema, fSAD, and normal tissue categories, summarized in Table 6-1. We computed the percentages of lobe voxels in the end-

exhalation geometry that fell into each category. For analysis, the combined percentage of voxels in the emphysema and fSAD ranges was considered *diseased*.

Table 6-1: Categories of tissue based on PRM analysis

Disease Category	End-Exhalation HU	End-Inhalation HU
Emphysema	< -856	< -950
fSAD	< -856	> -950
Normal	> -856	> -950

6.2.5 Tissue Elasticity Estimation

A previously developed and validated biomechanical model was used to estimate elasticity of the lung parenchyma, evaluated as the YM. In this study, the model used the DVF pointing from the 5DCT-based end-exhalation image to the end-inhalation image as the ground-truth DVF. Then, an initial elasticity distribution was set based on the HU of the end-exhalation scan. The elasticity distribution was then optimized to minimize the difference between the model-calculated DVF based on boundary conditions and the calculated deformations from elastic forces and the ground-truth DVF. In each iteration, the elasticity was updated, the new DVF was calculated from the updated elasticity values, and the DVF was compared to the ground truth. This process is shown in the flowchart in Figure 6-2. Details of the finite element approach, governing equations, boundary conditions, and description of the inverse approach to optimize the elasticity can be found in several publications describing the model[96,170,182]. The *lobar elasticity* was obtained by calculating the mean elasticity across each lobe distribution.

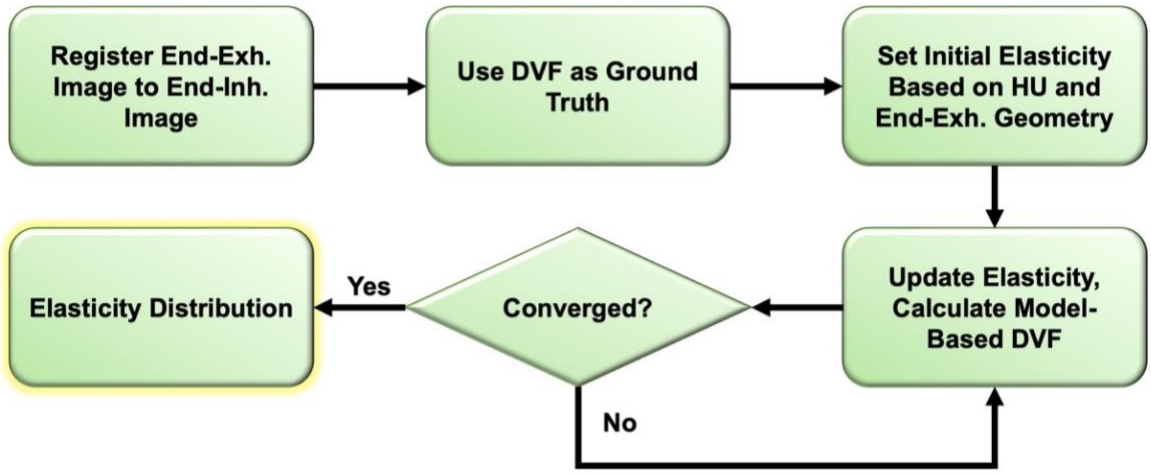

Fig. 6-2: Flowchart of the iterative parameter optimization problem to estimate elasticity. Exh. and Inh. are abbreviations for exhalation and inhalation, respectively.

We also considered voxels based on their elasticity into COPD biomarker and normal elasticity categories. Elasticities in the range of 1-3 kPa indicated diseased lung because COPD causes the lungs to poorly respond to expansion or contraction according to a previous study[172]. Therefore, we classified these voxels in the COPD biomarker category.

6.2.6 Heterogeneity Analysis of PRM and Elasticity

First, we calculated heterogeneity between the five lobes for each patient, or the interlobar heterogeneity. Since interlobar heterogeneity does not have a consistent definition in the literature, we formulated a single, scalar parameter for each property that described heterogeneity on a 0-1 scale, much like the VHI formulation in Chapter 5. First, we defined the Emphysema and fSAD Heterogeneity Index (EFHI) as

$$EFHI = \left|1 - \frac{100 - EF_{max}}{100 - \overline{EF_{\sim max}}}\right| \tag{6-1}$$

where EF_{max} is the maximum lobe percentage in the emphysema or fSAD ranges, and $\overline{EF_{\sim max}}$ is the mean of the other four lobe percentages. A higher EFHI indicates a larger difference between the most affected lobe and the mean of the four other lobes.

Finally, we defined the Elasticity Heterogeneity Index (EHI) based on the maximum percent of voxels in the COPD biomarker range among the five lobes, E_{max}, and the mean of the other four lobe percentages, $\overline{E_{\sim max}}$, as in Equation 3. Like the other indices, this index indicated the least functioning lobe compared to the other four.

$$EHI = \left|1 - \frac{100 - E_{max}}{100 - \overline{E_{\sim max}}}\right| \quad (6\text{-}2)$$

To analyze the intralobar heterogeneity, or the heterogeneity within each lobe, using PRM, we defined a PRM intralobar index. The index was devised to represent 50% of diseased tissue as perfectly heterogeneous and 0% or 100% diseased as perfectly homogeneous. The expression used to calculate the PRM intralobar index is shown in Equation 6, where EF is the percentage of lobe voxels in the diseased categories. The PRM intralobar index is 0 for lobes with 0% or 100% of voxels in the diseased categories and 1 for lobes with 50% of such voxels.

$$PRM\ Intralobar\ Index = \frac{50\% - |50\% - EF|}{50\%} \quad (6\text{-}3)$$

To measure intralobar heterogeneity in elasticity, we calculated the coefficient of variation, or the standard deviation as a percent of the mean, of the elasticity distributions within each lobe. This metric summarizes the spread of data within each lobe distribution. To document the intralobar heterogeneity of PRM indication, we simply considered the percentage of voxels in the diseased categories.

6.3 Results

As in Chapter 5, each patient was considered to have no COPD, mild COPD, or moderate-to-severe COPD based on their physician notes. Three patients were noted to have COPD, though the severity was unknown from their charts.

6.3.1 Comparison of Lobar Elasticity and PRM Results

We observed that nine of the 14 patients with COPD had lobes with a mean elasticity in the COPD biomarker range. However, only one of the five patients with COPD but elasticity outside of the COPD biomarker range had a lobe with at least 1% of voxels in the emphysema range based on the PRM analysis. So, typically when elasticity did not indicate the presence of COPD in one of the lobes, neither did the PRM analysis. Additionally, five of the six patients with moderate-to-severe COPD had lobes with elasticity in the COPD biomarker range. This may suggest that elasticity is a more effective biomarker for patients with more severe cases of COPD than less severe cases.

To analyze how well elasticity could indicate the disease heterogeneity in the context of lobe damage, Figure 6-3 shows results for the most diseased lobe of each patient according to the PRM analysis. The most diseased lobe was determined by the lobe with the highest combined percentage of voxels in the emphysema and fSAD categories. The most diseased lobe of each patient was plotted in the scatter plot shown in Figure 6-3 based on its lobar elasticity and percent of lung voxels in the disease categories from the PRM analysis. The variation of these data is discussed in the heterogeneity section (6.2.6).

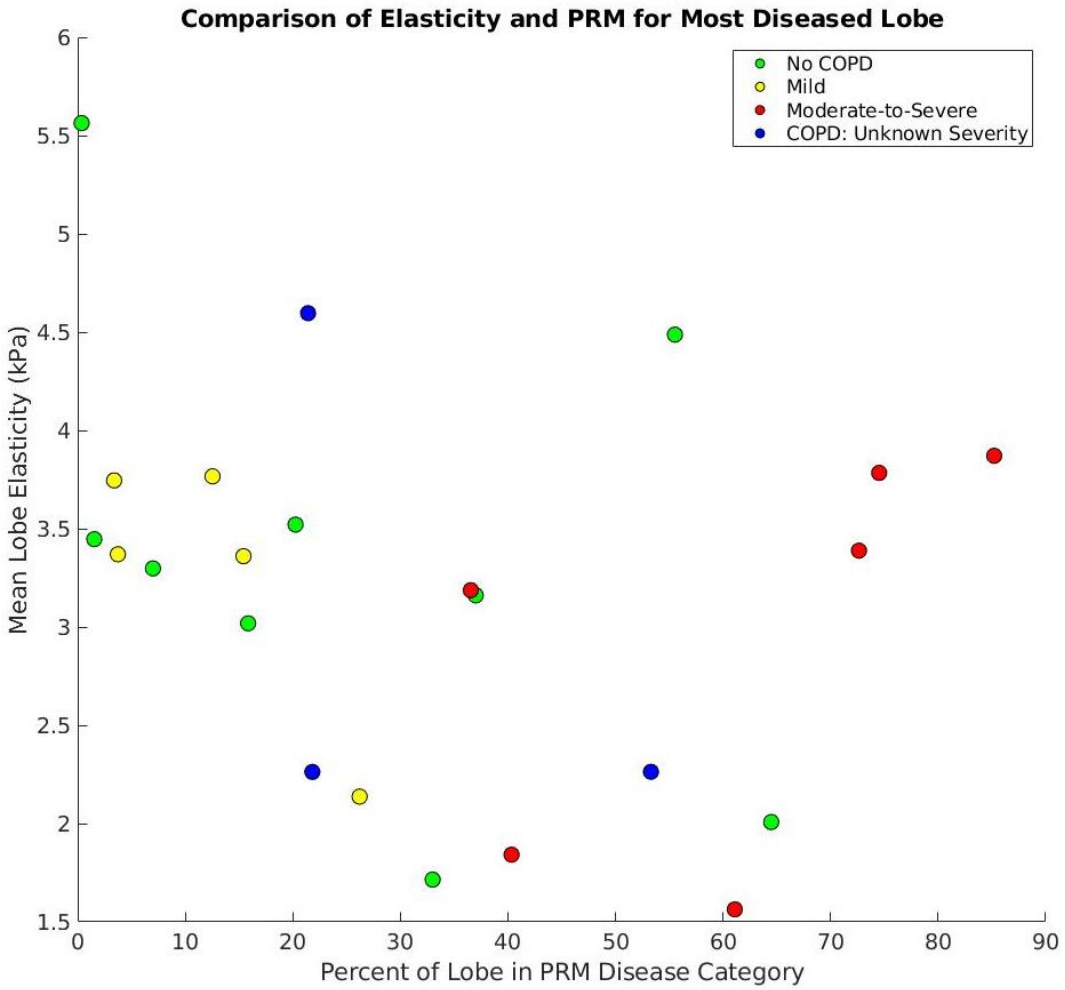

Fig. 6-3: Scatter plot of mean lobe elasticity vs. the percent of lobe voxels in disease categories for the lobe with the highest percent of diseased voxels according to PRM. The color and shape of the markers indicate disease severity of the patients.

From Figure 6-3, it can be seen that in certain cases, the two biomarkers agree. For instance, the group of patients below 20% diseased lobe showed mean elasticity values above 3 kPa. Seven patients with PRM results above the 20% diseased line had mean lobe elasticities in the 1-3 kPa range. However, there was also a few patients where the PRM indication was a high percentage of diseased lobe, but the lobar elasticity remained above the 1-3 kPa range. Notably, this included the three moderate-to-severe cases with greater than 70% of the lobe categorized as diseased. Therefore, there was not always a common agreement between mean elasticity

and PRM indicated disease. This shows that the biomechanical properties of the tissue may not strictly adhere to the measured presence of disease.

Although the elasticity did not always fall in the COPD biomarker range when PRM indicated a high level of disease, the most diseased regions often agreed between the properties. When comparing the most diseased lobe determined by PRM to the lobe with the lowest elasticity, the same lobe was indicated 43.5% of the time. However, if we analyzed the lungs in terms of upper vs. lower (combining the right upper and right middle lobes), then the two properties indicated the same regions 82.6% of the time. When indicating the least diseased lobes or regions, the two properties agreed 60.9% of the time in either case. Therefore, elasticity may be more in accordance with PRM in identifying the most diseased regions of the lungs relative to the other regions but may differ more often in identifying the healthier regions.

Figure 6-4 shows examples of the distributions in coronal slices for a patient that had good agreement between elasticity and PRM in identifying the most diseased lobe and a patient that did not agree. Figures 6-4a and 6-4b show the CT scan and lobe segmentation for the patient with good agreement between elasticity and PRM, respectively. Figures 6-4c and 6-4d show the PRM and elasticity distributions, respectively. Figures 6-4(e-h) show the same figures for the patient with poor agreement between properties. This figure helps to visualize the possible similarities and differences between elasticity and PRM distributions.

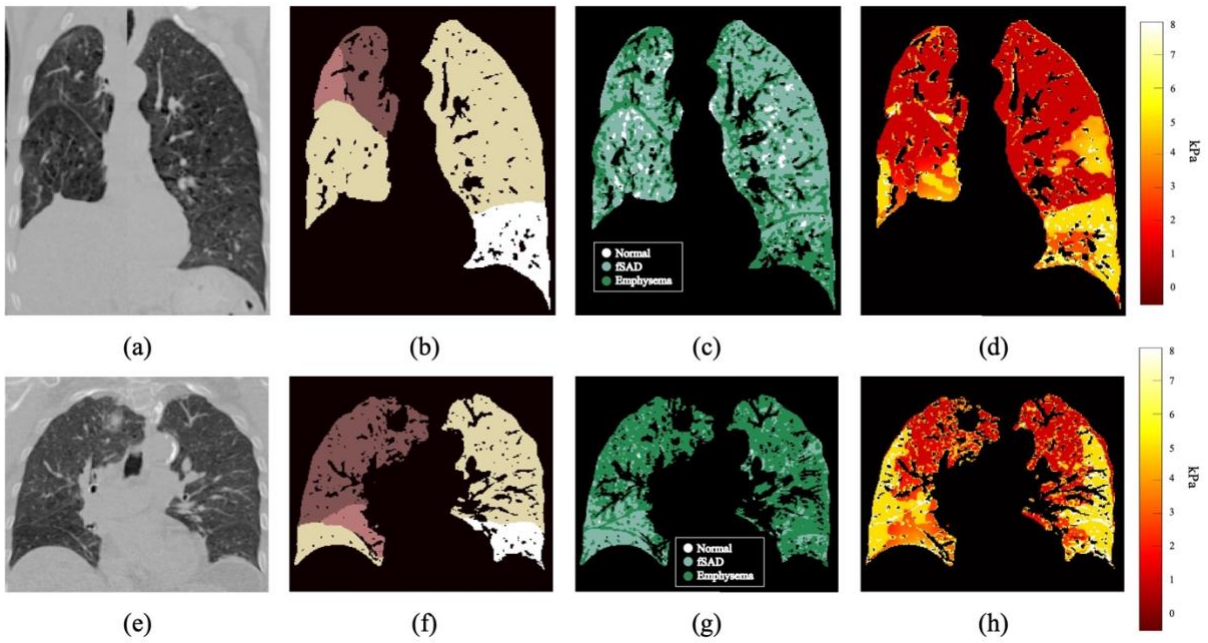

Fig. 6-4: Example distributions for two different patients. TOP ROW: (a) End-exhalation scan, (b) end-exhalation lobe mask with vessels segmented, (c) PRM distribution, and (d) elasticity distribution for patient with good agreement. The most diseased lobe was the right middle lobe (RML) according to PRM and lobar elasticity. BOTTOM ROW: (e) End-exhalation scan, (f) end-exhalation lobe mask with vessels segmented, (g) PRM distribution, and (h) elasticity distribution for patient with poor agreement. The most diseased lobe was also the RML, but the highest lobar elasticity was in the right upper lobe (RUL). The left and right lungs were enlarged to enhance visibility.

6.3.2 Heterogeneity Results

The mean EFHI was 0.223 ± 0.183, and the mean EHI was 0.388 ± 0.162. Therefore, on average, there were moderate levels of interlobar heterogeneity in each property. Figure 6-5 shows a scatter plot of the EHI and the EFHI for each patient. For patients with an EFHI less than 0.4, designated by the vertical line, the indices seemed to correlate. The linear fit of these 18 patients had an equation of 1.20*EFHI+0.206 with an R^2 of 0.606. However, for patients with an EFHI above 0.4, the relationship broke down. These data suggest that the interlobar heterogeneity in elasticity may correlate to the heterogeneity of disease determined by PRM in less severely heterogeneous cases.

Another notable observation was that the moderate-to-severe cases all showed relatively heterogeneous behavior as measured by the indices of both properties. All these patients had EFHIs and EHIs of at least 0.2. Additionally, all the patients with mild COPD had an EFHI below 0.2, but EHIs varied greatly.

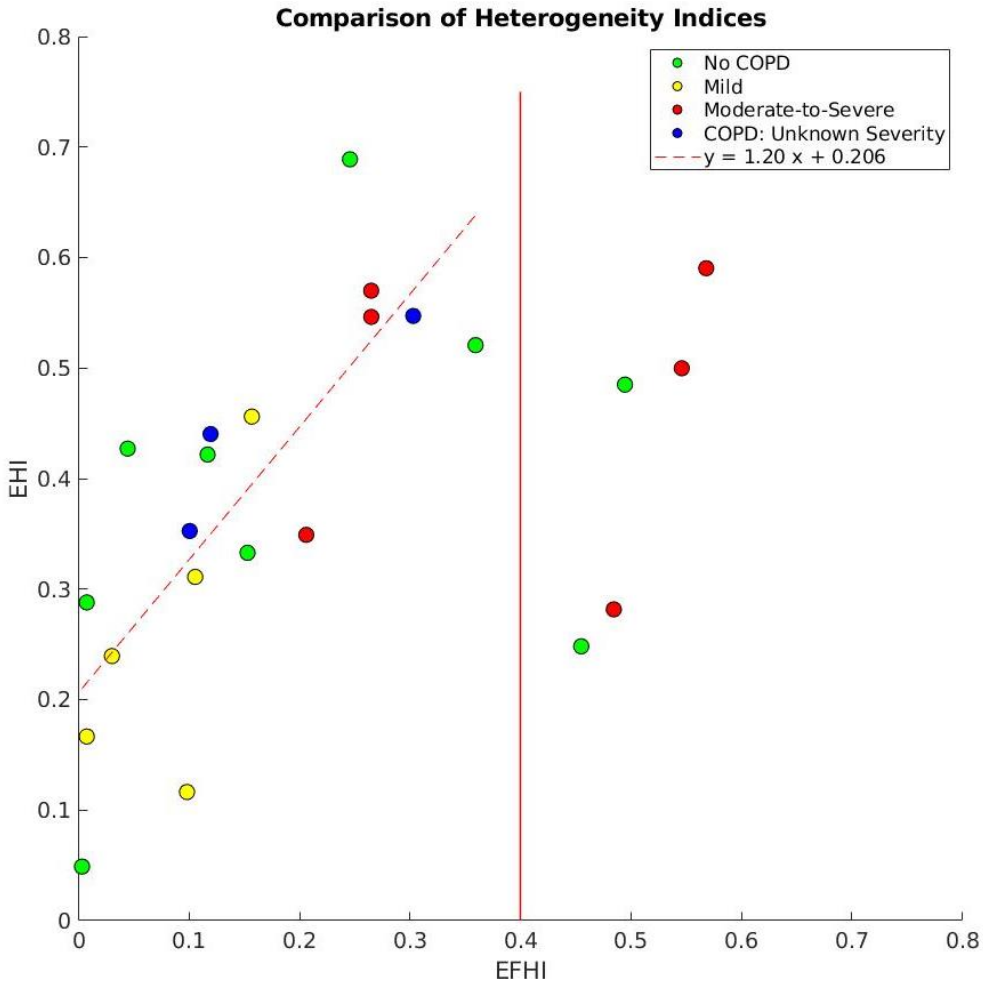

Fig. 6-5: Scatter plot of EHI vs. EFHI for all patients. The color and shape of the markers indicate disease severity of the patients. The vertical line designates the EFHI after which the linear fit relationship degrades.

Figure 6-6 shows a bar graph of the mean EFHI and EHI across patients in each COPD severity group. In each group, the EHI was consistently higher than the EFHI, suggesting more interlobar heterogeneity in disease indication in elasticity than PRM. Moreover, the interlobar heterogeneity in patients with mild COPD was lower than those without COPD or with

moderate-to-severe COPD. Finally, both heterogeneity indices were highest for patients with moderate-to-severe COPD.

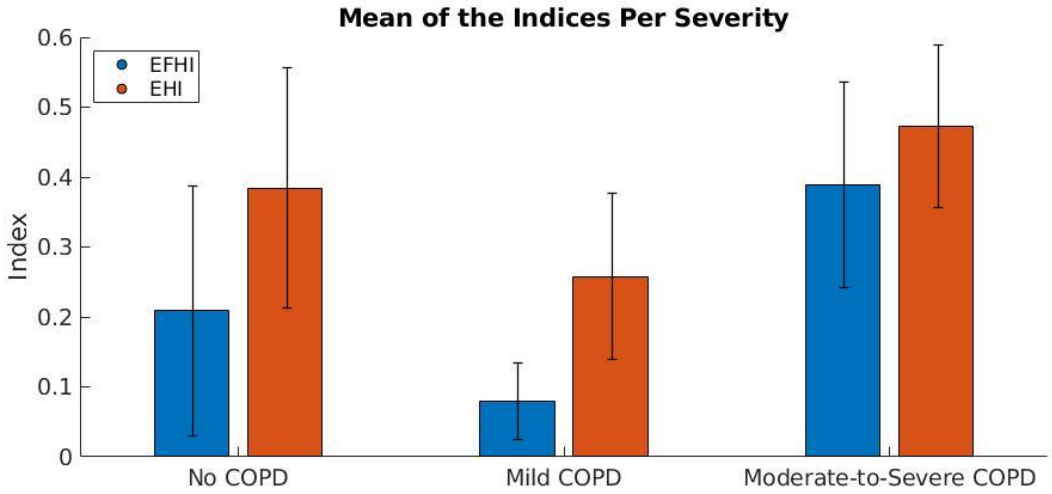

Fig. 6-6: Bar graph of the mean EFHI and mean EHI of patients in each COPD severity groups. The left bar shows the mean EFHI. The right bar shows the mean EHI. Error bars indicate standard deviations.

The intralobar heterogeneity measured by the intralobar PRM index were summarized by the histograms shown in Figure 6-7. Figure 6-7a shows the distribution across all lobes of all patients, which had a mean PRM intralobar index of 0.319 ± 0.297. Figure 6-7b shows the histogram across all lobes of patients without COPD (mean 0.218 ± 0.274). The lobes of patients with mild COPD had the lowest heterogeneity on average (mean 0.127 ± 0.145), and not one lobe had an intralobar PRM index higher than 0.6, as shown in Figure 6-7c. Based the histogram in Figure 6-7d, the heterogeneity is highest on average for patients with moderate-to-severe COPD (mean 0.577 ± 0.221).

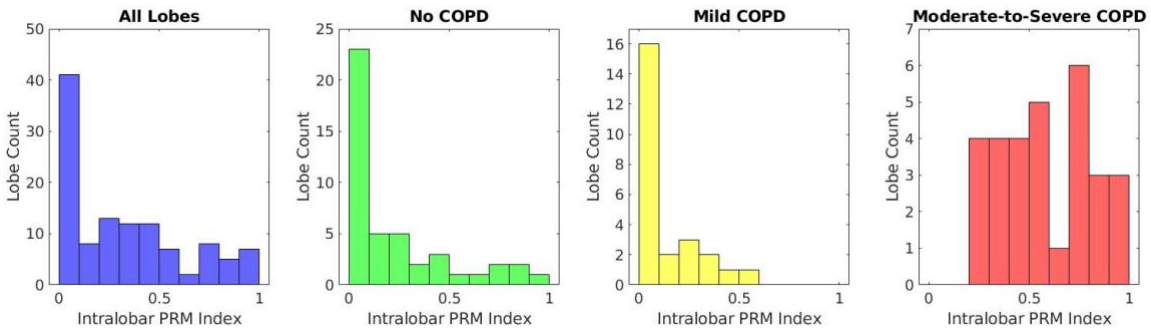

Fig. 6-7: Histograms of the intralobar PRM index for (a) lobes of all patients, (b) lobes of patients without COPD, (c) lobes of patients with mild COPD, and (d) lobes of patients with moderate-to-severe COPD.

The coefficients of variation of each lobar elasticity distribution are summarized by the histograms in Figure 6-8. The histogram in Figure 6-8a includes all lobes to offer a general sense of intralobar heterogeneity regardless of disease state. The mean of this distribution was 51.1% ± 16.6%, showing that there was a high level of intralobar heterogeneity in all cases. Figure 6-8b shows the histogram of the coefficient of variation for the lobes of patients without COPD (mean 47.9% ± 17.5%), and Figure 6-8c shows the histogram for those of patients with mild COPD (mean 47.3% ± 11.2%). These two groups exhibited a similar distribution to each other and to distribution of all patient lobes. On the other hand, the histogram of the moderate-to-severe COPD group coefficients shown in Figure 6-8d exhibited a higher distribution (mean 58.9% ± 17.7%). This may indicate that patients with more severe COPD may experience higher levels of intralobar heterogeneity.

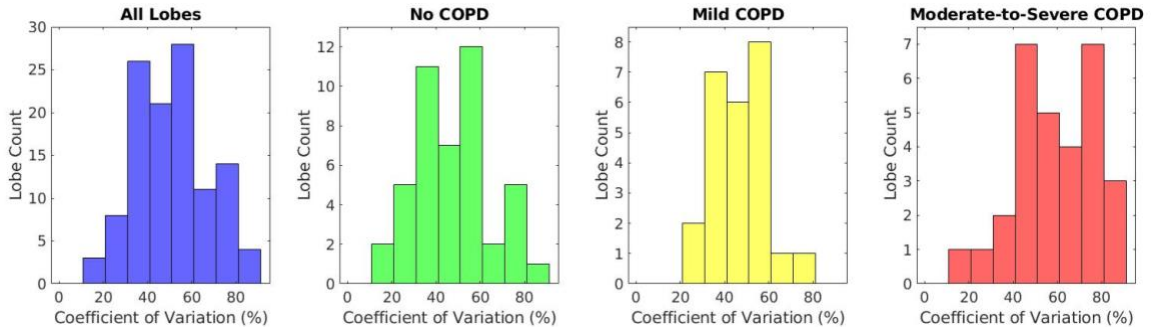

Fig. 6-8: Histograms of the coefficients of variation of elasticity distributions for (a) lobes of all patients, (b) lobes of patients without COPD, (c) lobes of patients with mild COPD, and (d) lobes of patients with moderate-to-severe COPD.

6.4 Discussion and Conclusions

In this paper, we analyzed the lung tissue functional heterogeneity on a lobar and sublobar basis to inform decision making in pulmonary surgeries or planning in radiation therapy. We did so by constructing 5DCT models to obtain end-exhalation and end-inhalation scans that served as the basis for all calculations. We used these scans to categorize voxels by disease state (emphysema, fSAD, or normal) using a PRM analysis. We also used the scans and the vectors mapping them to estimate elasticity using a validated biomechanical model. We showed that while the mean lobar elasticity might not always agree with the PRM indications, the most diseased lobe often did. This demonstrated that elasticity could indicate regional patterns of lobe function that are not identified by categorizing the HUs. Heterogeneity was analyzed across lobes as well as within lobes. Based on the consistent heterogeneity seen in elasticity at both levels, we conclude that the heterogeneity of lung function needs to be considered to make the most informed decisions for surgical or radiotherapy planning.

From the intralobar heterogeneity results, specifically, we observed some consistency in disease indication between elasticity and PRM. Both biomarkers showed higher intralobar heterogeneity in patients with moderate-to-severe COPD. This might suggest that heterogeneity of disease could be an indicator for disease severity. The discrepancies between the intralobar heterogeneity measured by the two biomarkers support the hypothesis that elasticity may provide additional functional information to indicate the disease of regional tissue. So, while both showed an increase in heterogeneity for moderate-to-severe cases, the

nuances between them show that considering elasticity and PRM together offers a fuller picture of the disease state.

The 5DCT approach used in this study has been well-validated in accurately modeling tissue motion. However, the accuracy of the modeling still has two primary limitations. One is the motion blur near the diaphragm. Though mitigated by the fast-scanning protocol, some motion blur artifacts may persist. To correct for motion blur, the velocity information needs to be considered before reconstruction, so this correction was not available with the retrospective datasets employed. In the future, such a correction will be developed and implemented to remove these effects from future data. The second limitation is from the image registration. These registration techniques have been well-validated and showed very accurate results, but some inaccuracies could be seen near the diaphragm due to the maximum motion. In the future, the motion blur correction should ameliorate this issue. A systematic analysis comparing all available deformable image registration techniques will also be executed to fully diagnose any discrepancies between methods and their individual limitations. Finally, more detailed model terms such as a cardiac motion term could be included in future developments to fine tune model accuracy.

Lobe segmentation was performed using an open-source software with a published validation[164]. However, in certain cases, minor corrections were required possibly due to fissure incompleteness. To reduce segmentation time and increase accuracy, a recently published machine learning technique[183] will be implemented instead. Additionally, the vessels were segmented out using a thresholding technique. There may be noise in the HU and boundary voxels that could cause some parenchymal voxels to be mistakenly segmented out of the images. Therefore, in the future, we will incorporate blood vessel tracking algorithms to

increase the sophistication of the technique and maintain as many parenchymal voxels as possible.

PRM analysis in this study was performed using the 5DCT-generated end-exhalation and end-inhalation scans with ventilation correction. Typically, PRM is performed on forced breathing CT scans (scanned at residual volume (RV) and total lung capacity (TLC)). The use of PRM analysis in this study may therefore be of particular interest as we have applied it to unique data. Future work will include a more comprehensive study of this application. This work will include an updated protocol to incorporate RV and TLC scans with the fast-helical scans so that the results can be compared. Such a study will yield a vast array of useful comparisons between the two protocols.

The tissue elasticity estimation using YM has been well-validated in previous studies[170]. However, any of the inaccuracies in the images or DVFs could potentially limit the model. Future work will include using a machine learning approach to estimate elasticity from just the end-exhalation scans, which would help to limit the effects of DVF inaccuracies[182]. In the future, this will replace the current iterative approach for faster and more accurate results. This technique could greatly reduce the computation time (from several days per patient to order of a few seconds). This would enable faster data collection and processing as well as a clinical path to relevance for tissue elasticity estimation.

Limitations of the study results are largely derived from the retrospective data collection. For example, too much missing data and some inconsistencies limited this study from including spirometry and smoking history to explore the relationships among these and compare to the regional properties. In the future, with a prospective protocol, we will acquire consistent spirometry measurements to provide further analysis to compare the presented

results to a more quantitative assessment of COPD via FEV_1/FVC as well as carefully documented smoking history.

In conclusion, heterogeneity of PRM and elasticity were consistently observed within and across lobes in patients with no COPD, mild COPD, and moderate-to-severe COPD. Though these properties agreed in some cases, they differed in others in terms of both disease indication and heterogeneity. Therefore, a thorough analysis including PRM and elasticity measurement on a lobar basis could together enable the best guidance for decision making during pulmonary surgical procedures or function sparing treatment planning for patients undergoing radiotherapy.

CHAPTER 7: CONCLUSIONS

7.1 Summary of Work

In this dissertation, we investigated several applications of FHFBCT within CT simulation in radiotherapy, beyond CT simulation, and beyond radiotherapy altogether. The individual projects tested the feasibility of using FHFBCTs to improve medical technologies and employed FHFBCT to gain insight into respiratory diseases to inform relevant treatments. Many of the projects also included 5DCT motion modeling to help characterize the motion dynamics captured in the images. These projects provided evidence for the value of using FHFBCTs for the studied applications, thus offering a basis to eventually impact radiotherapy and surgical planning. Finally, this work established a foundation to encourage further investigations into the many other potential treatments or procedures that could benefit from the characterization of free breathing dynamics in patients.

In Chapter 2, we investigated FHFBCTs in the traditional CT simulation setting of radiotherapy by quantifying the ability of the skin surface to serve as a surrogate for the diaphragm motion. We found that the skin surface motion correlated with the diaphragm motion within 11.8% ± 4.61% for at least regions in the center abdomen. The work in this study showed that FHFBCTs could not only be used to verify the integrity of the respiratory bellows but also to investigate the accuracy of using surface imaging as a respiratory surrogate. The varying patterns observed across the torso also showed that surface imaging could provide a comprehensive surrogate that allows for differentiation of different modes of breathing, such as abdominal vs. chest breathing.

In Chapter 3, we applied the breathing dynamics provided by FHFBCTs to a different step of the radiotherapy workflow by using a motion model to guide motion compensation during

CBCT reconstruction. To demonstrate the feasibility of our technique, we showed that we could improve the sharpness of the diaphragm in reconstructed CBCT images by adjusting the number of amplitude gating bins. We compared our results using FHFBCTs and 5DCT to the more conventional SART approach and showed vast improvements in image quality and sharpness. A 5DCT-based MC-SART approach could lead to CBCTs with less artifacts without any added dose to the radiotherapy workflow as well as the potential for improved ART approaches. Our approach also only required one iteration of the MC-SART formulation, thus vastly reducing computation time and making it far more feasible for a clinical setting.

In Chapter 4, we stepped outside of the radiotherapy domain and investigated the possibility of using FHFBCTs in fluid dynamics modeling for surgical guidance. Conventional methods for automatically modeling the airway geometry using segmented airways from FHFBCTs typically resulted in meshing errors during simulation. To address this concern, we developed a novel, automatic meshing algorithm to generate CFD-compliant geometry using airways segmented from FHFBCT and demonstrated improvements over several conventional automatic techniques. Future CFD modeling with our technique could lead to a comprehensive FSI model used to simulate interventional outcomes.

In Chapter 5, we demonstrated two benefits of FHFBCTs in the pulmonology domain, including a confident approach to calculating ventilation using FHFBCTs as well as a characterization of ventilation heterogeneity across lungs and lobes. We quantified the tendency of ventilation to be higher in the left lung rather than the right lung. We also demonstrated that while the ipsilateral lobes each showed heterogeneous ventilation patterns, as expected, the contralateral lobes had rather similar ventilation patterns. We were also able to characterize these trends in various COPD severity cases and found that ventilation

heterogeneity was higher for patients with COPD than without COPD. LVRS, BLVR, and other pulmonary interventions depend on disease heterogeneity, so using a functional property like ventilation could benefit to the patient selection process.

In Chapter 6, we turned our attention to a biomechanical property that could be assessed on a voxel-by-voxel scale by regionally analyzing the tissue elasticity of some of these patients. We compared our results to a studied technique, PRM, to identify the differences in disease indication between the two. We found that they offered similar results in patients with moderate-to-severe COPD but varied in other cases. We also found higher levels of interlobar and intralobar heterogeneity in patients with moderate-to-severe COPD than others as indicated by both biomarkers. This study conveyed the value of using elasticity estimated from FHFBCT for disease characterization during the planning stages of respiratory interventions.

These works have all contributed to the overall goal of exhibiting the immense value of applying breathing dynamics from FHFBCT to novel medical technologies and procedures. There are many directions that future work in this area could take to further develop these applications or extend the vision of this work to include others.

7.2 Future Work

One important step in future work is the addition of residual volume (RV) and total lung capacity (TLC) breath-hold CT images to the imaging protocol. This will be pivotal in comparing the dynamic information of FHFBCT to the static information contained in RV and TLC scans. This would further solidify our knowledge of the additional information provided by dynamic imaging. To complete this investigation, a large cohort of patients should be scanned with 25 FHFBCTs followed by RV and TLC scans in the same imaging session to control for potential day-to-day variations. Then, functional properties such as ventilation and

elasticity should be calculated from each to compare the discrepancies in the distributions. This could lead to a quantification of the different patterns of functional properties extracted from dynamic vs. static images, as well as offer a comparison of our protocol to those typically used in surgical intervention planning.

Another key area of investigation to expand this research is dose reduction. The scanning dose of the 5DCT protocol considers the fact that patients will already receive much higher doses during treatment. For many of the proposed applications, the dose would have to be reduced to be considered clinically acceptable. Dose can be reduced through several techniques. One such technique is reducing the number of scans. Research has been done on the feasibility of reducing the scans used in the 5DCT model[184]. Additionally, lowering the tube current can reduce the dose, but will increase the noise in the images[185]. Further research into the effects of each dose reduction technique on our methods should be performed to bring the topics of this dissertation to clinical practice outside of radiation oncology.

We have made initial efforts to explore reducing the dose via reduction of the tube current. Specifically, we set out to measure the effect of tube current reduction on ventilation consistency. For 11 patients, we simulated reductions in tube current in the FHFBCTs and calculated ventilation maps between each FHFBCT and a reference scan using the Jacobian operator. Figure 7-1 contains a flowchart of the proposed study design, including noise injection on FHFBCTs using a method from Hasse, at al.[186], registration of each FHFBCT to a common reference, calculation of Jacobians using dJ/dA, and comparison of the distributions via measurement differences and image similarity metrics.

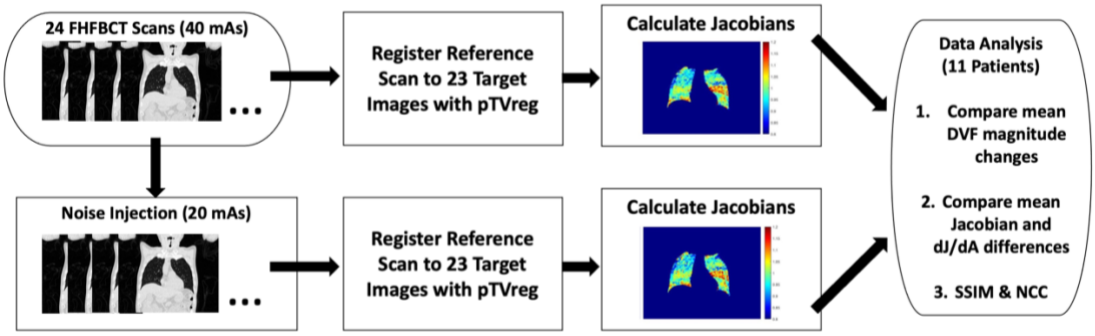

Fig. 7-1: Proposed study to measure the impact of dose reduction on ventilation measurements. SSIM and NCC are abbreviations for Structural Similarity Index Measure and Normalized Cross Correlation, respectively.

Preliminary results showed high consistency in dJ/dA between original image sets and image sets simulated to 20 mAs. The mean dJ/dA difference when amplitudes were normalized to the breathing range was 0.081. The mean SSIM and NCC between ventilation maps were 0.995 and 0.978, respectively, indicating consistency in regional patterns. Figure 7-1 shows an example of a scan pair with a simulated tube current reduction of 40 mAs to 20 mAs and the corresponding dJ/dA distributions.

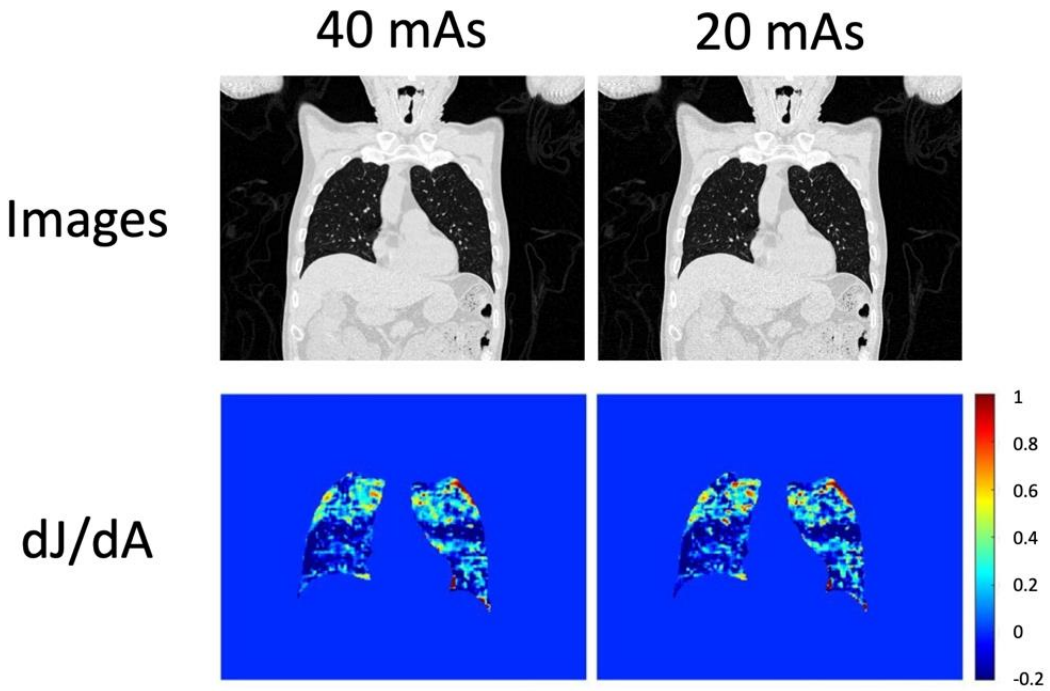

Fig. 7-2: Preliminary results from noise injection study from one patient case. The top row shows images at 40 mAs (left) and simulated 20 mAs (right). The bottom row shows the corresponding ventilation maps. The mean SSIM was 0.979 and the mean NCC was 0.850 for the dJ/dA distributions.

The noise injection study is still in progress. Results of the noise injection must be validated using a phantom study. This will either indicate accurate simulation of mAs reduction or provide an "effective mAs" conversion that can be used to correct the noise injection. Furthermore, we have previously mentioned the instability of the Jacobians on a voxel scale in Chapters 5 and 6. Therefore, this work will also have to include an analysis of larger regions of voxels and their dJ/dA consistency. The slab-based method in Chapter 5 could prove useful for this purpose. Continuing this work could offer an avenue for some of the methods proposed in this dissertation to be performed with images acquired at satisfactory doses for the pulmonology domain.

Additionally, future work should include the topic of image registration. The methods used in this dissertation work, deeds and pTVreg, followed the work of previous studies and were sufficiently accurate for our studies. However, as the motion modeling in each project is driven by the image registration, improving registration accuracy will be paramount in improving the precision of each method. For example, in Chapter 5, we decided to use lobar distributions due to known inaccuracies in ventilation calculations at the voxel level due to image registration inaccuracies. Therefore, future research pushing the boundaries of registration capabilities would directly benefit all work performed in this dissertation. Additionally, developing methods to quantify the accuracy of current registration techniques could offer more detailed insight into the limitations of each method due to errors in image registration.

As discussed in Chapter 1, 5DCT is a well-validated technique already in clinical use. However, there are still improvements to the workflow that could lead to more accurate modeling of human breathing. This could include a cardiac modeling term that removes errors commonly observed near the heart[22]. Additionally, in Chapter 6 we applied a HU correction to account for changing air content during respiration. This should be further developed as a component of the 5DCT model. Future work in this regard could develop the 5DCT modeling accuracy and therefore improve the methods used in this dissertation.

Developing machine learning techniques to replace certain steps in each of the presented studies could offer several advantages. These methods could reduce computation time[187], increase availability of the techniques[188], and identify intricate patterns in patient data[189]. For example, machine learning could be used to comprehensively analyze the skin surface as a surrogate following the work of Chapter 2, perform the diaphragm alignment in Chapter 3, or measure ventilation from CT in Chapter 5. A machine learning technique for estimating elasticity has already been developed to reduce computation time in studies such as the one in Chapter 6[182]. However, as is the case with many machine learning tasks, much more patient data needs to be acquired and analyzed to confidently replace these proposed methods with machine learning-based solutions. Therefore, future work to introduce machine learning and its advantages must first begin with expanding all the patient cohorts.

The work performed in Chapter 3 to offer improved CBCT reconstruction could lead to a great deal of future work. A study quantifying the impact of our CBCT reconstruction technique on alignment accuracy for during radiotherapy treatment could be a key step in translating our method to the clinic. Moreover, research to harness the improved CBCT

reconstruction for ART techniques could offer methods to reduce side effects of radiotherapy and improve tumor coverage over several treatment fractions.

In the case of airflow modeling, we showed that FHFBCTs could be used to generate CFD-compliant geometries. This should lead to future efforts to incorporate flow modeling to the overall FSI model. To complete this non-insignificant task, the first step should be to develop a comprehensive airflow model with the correct parameters for patient-specific breathing. These parameters and constraints could come from spirometry and respiratory surrogates such as the bellows or the skin surface. Then, the lung parenchyma needs to be biomechanically modeled to include ventilation, elasticity, and any other relevant property that can be measured from medical imaging. This could be initially accomplished by modeling a sponge-like material to represent tissue and using the ventilation mapping approaches proposed in Chapter 5. Finally, the 5DCT model associated with each patient should be incorporated to include the deformable motion of the airways as well as the parenchyma.

Finally, in terms of ventilation mapping and using FHFBCT in the pulmonology domain, future work should first continue to develop and comprehensively analyze the ventilation mapping approaches. We performed our study on the lobar scale because the lobe volumes offered more confidence in the resulting ventilation than a voxel-by-voxel approach, while still being anatomically defined and physiologically meaningful sub-regions of the lungs. In the future, a full study exploring the resolution of ventilation mapping versus the confidence in the results should be executed to determine if finer, functionally defined sub-regions could be used instead to gain more insight into disease heterogeneity. Secondly, more patient data should be acquired, focusing primarily on patients with COPD. Not only should more patients be studied, but as much information regarding demographics, comorbidities, and spirometry as possible

should be included. This will shed light on how disease heterogeneity and all these factors may correlate, which could provide necessary information for personalized medicine.

REFERENCES

1. Schittny JC. Development of the lung. *Cell and tissue research.* 2017;367(3):427-444.

2. Loring SH, Topulos GP, Hubmayr RD. Transpulmonary pressure: the importance of precise definitions and limiting assumptions. *American journal of respiratory and critical care medicine.* 2016;194(12):1452-1457.

3. Biga LM, Dawson S, Harwell A, et al. *Anatomy & physiology.* 2020.

4. Flynn D. A survey of hysteresis models of mammalian lungs. *Rend Sem Mat Univ Politec Torino.* 2014;72:17-36.

5. Macklem P. Normal and abnormal function of the diaphragm. *Thorax.* 1981;36(3):161.

6. De Troyer A, Estenne M. Coordination between rib cage muscles and diaphragm during quiet breathing in humans. *Journal of Applied Physiology.* 1984;57(3):899-906.

7. Haddad M, Sharma S. Physiology, lung. 2019.

8. Cotes JE, Chinn DJ, Miller MR. *Lung function: physiology, measurement and application in medicine.* John Wiley & Sons; 2009.

9. Key Statistics for Lung Cancer. American Cancer Society. https://www.cancer.org/cancer/lung-cancer/about/key-statistics.html#references. Published 2022. Accessed2022.

10. Mannino DM. COPD: epidemiology, prevalence, morbidity and mortality, and disease heterogeneity. *Chest.* 2002;121(5):121S-126S.

11. Murphy SL, Xu J, Kochanek KD, Arias E. Mortality in the united states, 2017. 2018.

12. Chronic obstructive pulmonary disease (COPD). World Health Organization. https://www.who.int/news-room/fact-sheets/detail/chronic-obstructive-pulmonary-disease-(copd). Published 2021. Updated 6/21/2021. Accessed 7/7/2021, 2021.

13. Baker S, Dahele M, Lagerwaard FJ, Senan S. A critical review of recent developments in radiotherapy for non-small cell lung cancer. *Radiation oncology.* 2016;11(1):1-14.

14. Criner GJ, Cordova F, Sternberg AL, Martinez FJ. The National Emphysema Treatment Trial (NETT) part II: lessons learned about lung volume reduction surgery. *American journal of respiratory and critical care medicine.* 2011;184(8):881-893.

15. Ernst A, Anantham D. Bronchoscopic lung volume reduction. Paper presented at: Seminars in thoracic and cardiovascular surgery2010.

16. Buzug TM. Computed tomography. In: *Springer handbook of medical technology.* Springer; 2011:311-342.

17. Hounsfield GN. Computerized transverse axial scanning (tomography): Part 1. Description of system. *The British journal of radiology.* 1973;46(552):1016-1022.

18. Lell MM, Wildberger JE, Alkadhi H, Damilakis J, Kachelriess M. Evolution in computed tomography: the battle for speed and dose. *Investigative radiology.* 2015;50(9):629-644.

19. Vock P, Jung H, Kalender W. Single-breath-hold Spiral Volumetric CT of the lung. Paper presented at: Proceedings of the 75th anniversary scientific assembly and annual meeting of the Radiological Society of North America (Abstracts)1989.

20. Hugo GD, Rosu M. Advances in 4D radiation therapy for managing respiration: part I–4D imaging. *Zeitschrift für medizinische Physik.* 2012;22(4):258-271.

21. Keall PJ, Mageras GS, Balter JM, et al. The management of respiratory motion in radiation oncology report of AAPM Task Group 76 a. *Medical physics.* 2006;33(10):3874-3900.

22. Low DA, White BM, Lee PP, et al. A novel CT acquisition and analysis technique for breathing motion modeling. *Physics in Medicine & Biology.* 2013;58(11):L31.

23. Yamamoto T, Kabus S, Lorenz C, et al. 4D CT lung ventilation images are affected by the 4D CT sorting method. *Medical physics.* 2013;40(10):101907.

24. Low DA, O'Connell D, Lauria M, et al. Ventilation measurements using fast-helical free-breathing CT. *Medical Physics.* 2021.

25. Low DA, Parikh PJ, Lu W, et al. Novel breathing motion model for radiotherapy. *International Journal of Radiation Oncology* Biology* Physics.* 2005;63(3):921-929.

26. Thomas D, Lamb J, White B, et al. A novel fast helical 4D-CT acquisition technique to generate low-noise sorting artifact–free images at user-selected breathing phases. *International Journal of Radiation Oncology* Biology* Physics.* 2014;89(1):191-198.

27. Dou TH, Thomas DH, O'Connell DP, Lamb JM, Lee P, Low DA. A method for assessing ground-truth accuracy of the 5DCT technique. *International Journal of Radiation Oncology* Biology* Physics.* 2015;93(4):925-933.

28. O'Connell D. *Development, validation, and translation of a respiratory motion model-based 4DCT technique for use as a clinical protocol for radiation therapy treatment planning*, UCLA; 2018.

29. O'Connell DP, Thomas DH, Dou TH, et al. Comparison of breathing gated CT images generated using a 5DCT technique and a commercial clinical protocol in a porcine model. *Medical physics.* 2015;42(7):4033-4042.

30. O'Connell D, Shaverdian N, Kishan AU, et al. Comparison of lung tumor motion measured using a model-based 4DCT technique and a commercial protocol. *Practical radiation oncology.* 2018;8(3):e175-e183.

31. Thomas DH, Tan J, Neylon J, et al. Investigating the minimum scan parameters required to generate free-breathing motion artefact-free fast-helical CT. *The British journal of radiology.* 2018;91(1082):20170597.

32. O'Connell D, Thomas D, Dou T, et al. Adaptive weighted median filtering for reduced blurring when fusing co-registered fast helical CT images. *Biomedical Physics & Engineering Express.* 2017;3(6):067002.

33. Low DA, Yang L, Chen J, et al. Analysis of motion blurring artifact in fast helical free-breathing thoracic CT scans. *Medical physics.* 2017;44(4):1456-1461.

34. O'Connell D, Thomas DH, Lamb JM, et al. Dependence of subject-specific parameters for a fast helical CT respiratory motion model on breathing rate: an animal study. *Physics in Medicine & Biology.* 2018;63(4):04NT04.

35. Heinrich MP, Jenkinson M, Brady M, Schnabel JA. MRF-based deformable registration and ventilation estimation of lung CT. *IEEE transactions on medical imaging.* 2013;32(7):1239-1248.

36. Heinrich MP, Jenkinson M, Bhushan M, et al. MIND: Modality independent neighbourhood descriptor for multi-modal deformable registration. *Medical image analysis.* 2012;16(7):1423-1435.

37. Heinrich MP, Jenkinson M, Papież BW, Brady M, Schnabel JA. Towards realtime multimodal fusion for image-guided interventions using self-similarities. Paper presented at: International conference on medical image computing and computer-assisted intervention2013.

38. Vishnevskiy V, Gass T, Szekely G, Tanner C, Goksel O. Isotropic total variation regularization of displacements in parametric image registration. *IEEE transactions on medical imaging.* 2016;36(2):385-395.

39. Fu Y, Wu X, Thomas AM, Li HH, Yang D. Automatic large quantity landmark pairs detection in 4DCT lung images. *Medical physics.* 2019;46(10):4490-4501.

40. McClelland JR, Hawkes DJ, Schaeffter T, King AP. Respiratory motion models: a review. *Medical image analysis.* 2013;17(1):19-42.

41. Low DA, Nystrom M, Kalinin E, et al. A method for the reconstruction of four-dimensional synchronized CT scans acquired during free breathing. *Medical physics.* 2003;30(6):1254-1263.

42. Werner R, White B, Handels H, Lu W, Low DA. Development of a tidal volume surrogate that replaces spirometry for physiological breathing monitoring in 4D CT. *Medical physics.* 2010;37(2):615-619.

43. Ionascu D, Jiang SB, Nishioka S, Shirato H, Berbeco RI. Internal-external correlation investigations of respiratory induced motion of lung tumors. *Medical physics.* 2007;34(10):3893-3903.

44. Bhagat N, Fidelman N, Durack JC, et al. Complications associated with the percutaneous insertion of fiducial markers in the thorax. *Cardiovascular and interventional radiology.* 2010;33(6):1186-1191.

45. Fayad H, Pan T, François Clement J, Visvikis D. Correlation of respiratory motion between external patient surface and internal anatomical landmarks. *Medical physics.* 2011;38(6Part1):3157-3164.

46. Vedam S, Kini V, Keall P, Ramakrishnan V, Mostafavi H, Mohan R. Quantifying the predictability of diaphragm motion during respiration with a noninvasive external marker. *Medical physics.* 2003;30(4):505-513.

47. Mageras GS, Yorke E, Rosenzweig K, et al. Fluoroscopic evaluation of diaphragmatic motion reduction with a respiratory gated radiotherapy system. *Journal of applied clinical medical physics.* 2001;2(4):191-200.

48. Korreman S, Mostafavi H, Le Q, Boyer A. Comparison of respiratory surrogates for gated lung radiotherapy without internal fiducials. *Acta Oncologica.* 2006;45(7):935-942.

49. Chi PCM, Balter P, Luo D, Mohan R, Pan T. Relation of external surface to internal tumor motion studied with cine CT. *Medical physics.* 2006;33(9):3116-3123.

50. Li G, Arora NC, Xie H, et al. Quantitative prediction of respiratory tidal volume based on the external torso volume change: a potential volumetric surrogate. *Physics in Medicine & Biology.* 2009;54(7):1963.

51. Li G, Wei J, Olek D, et al. Direct comparison of respiration-correlated four-dimensional magnetic resonance imaging reconstructed using concurrent internal navigator and external bellows. *International Journal of Radiation Oncology* Biology* Physics.* 2017;97(3):596-605.

52. Hoisak JD, Pawlicki T. The role of optical surface imaging systems in radiation therapy. Paper presented at: Seminars in radiation oncology2018.

53. Schaerer J, Fassi A, Riboldi M, Cerveri P, Baroni G, Sarrut D. Multi-dimensional respiratory motion tracking from markerless optical surface imaging based on deformable mesh registration. *Physics in Medicine & Biology.* 2011;57(2):357.

54. Li G, Wei J, Huang H, et al. Characterization of optical-surface-imaging-based spirometry for respiratory surrogating in radiotherapy. *Medical physics.* 2016;43(3):1348-1360.

55. Koch N, Liu HH, Starkschall G, et al. Evaluation of internal lung motion for respiratory-gated radiotherapy using MRI: Part I—correlating internal lung motion with skin fiducial

motion. *International Journal of Radiation Oncology* Biology* Physics.* 2004;60(5):1459-1472.

56. Cai J, Chang Z, Wang Z, Paul Segars W, Yin FF. Four-dimensional magnetic resonance imaging (4D-MRI) using image-based respiratory surrogate: a feasibility study. *Medical physics.* 2011;38(12):6384-6394.

57. Chowdhury SR, Dutta J. Higher-order singular value decomposition-based lung parcellation for breathing motion management. *Journal of Medical Imaging.* 2019;6(2):024004.

58. Lu W, Low DA, Parikh PJ, et al. Comparison of spirometry and abdominal height as four-dimensional computed tomography metrics in lung. *Medical physics.* 2005;32(7Part1):2351-2357.

59. Lauria M, Navaratna R, O'Connell D, Santhanam A, Lee P, Low DA. Investigating internal–external motion correlation using fast helical CT. *Medical physics.* 2021;48(4):1823-1831.

60. Sterzing F, Engenhart-Cabillic R, Flentje M, Debus J. Image-guided radiotherapy: a new dimension in radiation oncology. *Deutsches Aerzteblatt International.* 2011;108(16):274.

61. Dawson LA, Sharpe MB. Image-guided radiotherapy: rationale, benefits, and limitations. *The lancet oncology.* 2006;7(10):848-858.

62. Jaffray DA. Image-guided radiotherapy: from current concept to future perspectives. *Nature reviews Clinical oncology.* 2012;9(12):688-699.

63. Brock KK. Adaptive radiotherapy: moving into the future. Paper presented at: Seminars in radiation oncology2019.

64. Scarfe WC, Farman AG. What is cone-beam CT and how does it work? *Dental Clinics of North America.* 2008;52(4):707-730.

65. Jaffray DA, Drake DG, Moreau M, Martinez AA, Wong JW. A radiographic and tomographic imaging system integrated into a medical linear accelerator for localization of bone and soft-tissue targets. *International Journal of Radiation Oncology* Biology* Physics.* 1999;45(3):773-789.

66. Jaffray DA, Siewerdsen JH, Wong JW, Martinez AA. Flat-panel cone-beam computed tomography for image-guided radiation therapy. *International Journal of Radiation Oncology* Biology* Physics.* 2002;53(5):1337-1349.

67. Purdie TG, Bissonnette J-P, Franks K, et al. Cone-beam computed tomography for on-line image guidance of lung stereotactic radiotherapy: localization, verification, and intrafraction tumor position. *International Journal of Radiation Oncology* Biology* Physics.* 2007;68(1):243-252.

68. Sajja S, Lee Y, Eriksson M, et al. Technical principles of dual-energy cone beam computed tomography and clinical applications for radiation therapy. *Advances in Radiation Oncology.* 2020;5(1):1-16.

69. Bryce-Atkinson A, De Jong R, Marchant T, et al. Low dose cone beam CT for paediatric image-guided radiotherapy: Image quality and practical recommendations. *Radiotherapy and Oncology.* 2021;163:68-75.

70. Boas FE, Fleischmann D. CT artifacts: causes and reduction techniques. *Imaging Med.* 2012;4(2):229-240.

71. Srinivasan K, Mohammadi M, Shepherd J. Applications of linac-mounted kilovoltage Cone-beam Computed Tomography in modern radiation therapy: A review. *Polish journal of radiology.* 2014;79:181.

72. Li T, Xing L, Munro P, et al. Four-dimensional cone-beam computed tomography using an on-board imager. *Medical physics.* 2006;33(10):3825-3833.

73. Sonke JJ, Zijp L, Remeijer P, Van Herk M. Respiratory correlated cone beam CT. *Medical physics.* 2005;32(4):1176-1186.

74. Wang J, Gu X. High-quality four-dimensional cone-beam CT by deforming prior images. *Physics in Medicine & Biology.* 2012;58(2):231.

75. Lau BK, Reynolds T, Keall PJ, et al. Reducing 4DCBCT imaging dose and time: exploring the limits of adaptive acquisition and motion compensated reconstruction. *Physics in Medicine & Biology.* 2022;67(6):065002.

76. Wang J, Gu X. Simultaneous motion estimation and image reconstruction (SMEIR) for 4D cone-beam CT. *Medical physics.* 2013;40(10):101912.

77. Huang X, Zhang Y, Wang J. A biomechanical modeling-guided simultaneous motion estimation and image reconstruction technique (SMEIR-Bio) for 4D-CBCT reconstruction. *Physics in Medicine & Biology.* 2018;63(4):045002.

78. Zhang Y, Huang X, Wang J. Advanced 4-dimensional cone-beam computed tomography reconstruction by combining motion estimation, motion-compensated reconstruction, biomechanical modeling and deep learning. *Visual Computing for Industry, Biomedicine, and Art.* 2019;2(1):1-15.

79. Huang X, Zhang Y, Chen L, Wang J. U-net-based deformation vector field estimation for motion-compensated 4D-CBCT reconstruction. *Medical physics.* 2020;47(7):3000-3012.

80. Mo Y, Liu J, Li Q, et al. Joint Motion Estimation and Compensation for Four-Dimensional Cone-Beam Computed Tomography Image Reconstruction. *IEEE Access.* 2021;9:147559-147569.

81. Riblett MJ, Christensen GE, Weiss E, Hugo GD. Data-driven respiratory motion compensation for four-dimensional cone-beam computed tomography (4D-CBCT) using groupwise deformable registration. *Medical physics.* 2018;45(10):4471-4482.

82. Sauppe S, Kuhm J, Brehm M, Paysan P, Seghers D, Kachelrieß M. Motion vector field phase-to-amplitude resampling for 4D motion-compensated cone-beam CT. *Physics in Medicine & Biology.* 2018;63(3):035032.

83. Guo M, Chee G, O'Connell D, et al. Reconstruction of a high-quality volumetric image and a respiratory motion model from patient CBCT projections. *Medical physics.* 2019;46(8):3627-3639.

84. Feldkamp LA, Davis LC, Kress JW. Practical cone-beam algorithm. *Josa a.* 1984;1(6):612-619.

85. Andersen AH, Kak AC. Simultaneous algebraic reconstruction technique (SART): a superior implementation of the ART algorithm. *Ultrasonic imaging.* 1984;6(1):81-94.

86. Rit S, Wolthaus JW, van Herk M, Sonke JJ. On-the-fly motion-compensated cone-beam CT using an a priori model of the respiratory motion. *Medical physics.* 2009;36(6Part1):2283-2296.

87. Zhang Q, Hu YC, Liu F, Goodman K, Rosenzweig KE, Mageras GS. Correction of motion artifacts in cone-beam CT using a patient-specific respiratory motion model. *Medical physics.* 2010;37(6Part1):2901-2909.

88. Yamamoto T, Langner U, Loo Jr BW, Shen J, Keall PJ. Retrospective analysis of artifacts in four-dimensional CT images of 50 abdominal and thoracic radiotherapy patients. *International Journal of Radiation Oncology* Biology* Physics.* 2008;72(4):1250-1258.

89. Antony R, Lonski P, Ungureanu E, et al. Independent review of 4DCT scans used for SABR treatment planning. *Journal of applied clinical medical physics.* 2020;21(3):62-67.

90. Rit S, Oliva MV, Brousmiche S, Labarbe R, Sarrut D, Sharp GC. The Reconstruction Toolkit (RTK), an open-source cone-beam CT reconstruction toolkit based on the Insight Toolkit (ITK). Paper presented at: Journal of Physics: Conference Series2014.

91. Tian F-B, Dai H, Luo H, Doyle JF, Rousseau B. Fluid–structure interaction involving large deformations: 3D simulations and applications to biological systems. *Journal of computational physics.* 2014;258:451-469.

92. Luo H, Mittal R, Zheng X, Bielamowicz SA, Walsh RJ, Hahn JK. An immersed-boundary method for flow–structure interaction in biological systems with application to phonation. *Journal of computational physics.* 2008;227(22):9303-9332.

93. Wall WA, Rabczuk T. Fluid–structure interaction in lower airways of CT-based lung geometries. *International Journal for Numerical Methods in Fluids.* 2008;57(5):653-675.

94. Yin Y, Choi J, Hoffman EA, Tawhai MH, Lin C-L. Simulation of pulmonary air flow with a subject-specific boundary condition. *Journal of biomechanics.* 2010;43(11):2159-2163.

95. Qi S, Li Z, Yue Y, van Triest HJ, Kang Y. Computational fluid dynamics simulation of airflow in the trachea and main bronchi for the subjects with left pulmonary artery sling. *Biomedical engineering online.* 2014;13(1):85.

96. Hasse K, Neylon J, Santhanam AP. Feasibility and quantitative analysis of a biomechanical model-guided lung elastography for radiotherapy. *Biomedical Physics & Engineering Express.* 2017;3(2):025006.

97. Ilegbusi O, Seyfi B, Neylon J, Santhanam AP. Analytic intermodel consistent modeling of volumetric human lung dynamics. *Journal of biomechanical engineering.* 2015;137(10).

98. Seyfi B, Santhanam AP, Ilegbusi OJ. A biomechanical model of human lung deformation utilizing patient-specific elastic property. *Journal of Cancer Therapy.* 2016;7(6):402-415.

99. Seyfi Noferest B, Santhanam AP, Ilegbusi OJ. Effect of gravity on subject-specific human lung deformation. *Mathematical and Computer Modelling of Dynamical Systems.* 2018;24(1):87-101.

100. Nowak N, Kakade PP, Annapragada AV. Computational fluid dynamics simulation of airflow and aerosol deposition in human lungs. *Annals of biomedical engineering.* 2003;31(4):374-390.

101. Lin C-L, Tawhai MH, McLennan G, Hoffman EA. Characteristics of the turbulent laryngeal jet and its effect on airflow in the human intra-thoracic airways. *Respiratory physiology & neurobiology.* 2007;157(2-3):295-309.

102. Walters DK, Burgreen GW, Lavallee DM, Thompson DS, Hester RL. Efficient, physiologically realistic lung airflow simulations. *IEEE transactions on biomedical engineering.* 2011;58(10):3016-3019.

103. Isaacs KK, Schlesinger R, Martonen TB. Three-dimensional computational fluid dynamics simulations of particle deposition in the tracheobronchial tree. *Journal of aerosol medicine.* 2006;19(3):344-352.

104. Ilegbusi OJ, Li Z, Seyfi B, et al. Modeling airflow using subject-specific 4DCT-based deformable volumetric lung models. *International journal of biomedical imaging.* 2012;2012.

105. Pieper S, Halle M, Kikinis R. 3D Slicer. Paper presented at: 2004 2nd IEEE international symposium on biomedical imaging: nano to macro (IEEE Cat No. 04EX821)2004.

106. Cignoni P, Callieri M, Corsini M, Dellepiane M, Ganovelli F, Ranzuglia G. Meshlab: an open-source mesh processing tool. Paper presented at: Eurographics Italian chapter conference2008.

107. Lorensen WE, Cline HE. Marching cubes: A high resolution 3D surface construction algorithm. *ACM siggraph computer graphics.* 1987;21(4):163-169.

108. Weibel ER, Cournand AF, Richards DW. *Morphometry of the human lung.* Vol 1: Springer; 1963.

109. Soni B, Aliabadi S. Large-scale CFD simulations of airflow and particle deposition in lung airway. *Computers & Fluids.* 2013;88:804-812.

110. Walters DK, Luke WH. Computational fluid dynamics simulations of particle deposition in large-scale, multigenerational lung models. *Journal of biomechanical engineering.* 2011;133(1).

111. Lesage D, Angelini ED, Bloch I, Funka-Lea G. A review of 3D vessel lumen segmentation techniques: Models, features and extraction schemes. *Medical image analysis.* 2009;13(6):819-845.

112. Miyawaki S, Tawhai MH, Hoffman EA, Wenzel SE, Lin C-L. Automatic construction of subject-specific human airway geometry including trifurcations based on a CT-segmented airway skeleton and surface. *Biomechanics and modeling in mechanobiology.* 2017;16(2):583-596.

113. Sazonov I, Nithiarasu P. Semi-automatic surface and volume mesh generation for subject-specific biomedical geometries. *International Journal for Numerical Methods in Biomedical Engineering.* 2012;28(1):133-157.

114. Marchandise E, Crosetto P, Geuzaine C, Remacle J-F, Sauvage E. Quality open source mesh generation for cardiovascular flow simulations. In: *Modeling of Physiological Flows.* Springer; 2012:395-414.

115. Marchandise E, Geuzaine C, Remacle J-F. Cardiovascular and lung mesh generation based on centerlines. *International journal for numerical methods in biomedical engineering.* 2013;29(6):665-682.

116. Lauria M, Singhrao K, Stiehl B, et al. Automatic triangulated mesh generation of pulmonary airways from segmented lung 3DCTs for computational fluid dynamics. *International Journal of Computer Assisted Radiology and Surgery.* 2021:1-13.

117. *ImageJ* [computer program]. 1997.

118. Doel T. Pulmonary Toolkit. In:2017.

119. Lee T-C, Kashyap RL, Chu C-N. Building skeleton models via 3-D medial surface axis thinning algorithms. *CVGIP: Graphical Models and Image Processing.* 1994;56(6):462-478.

120. Huang H, Wu S, Cohen-Or D, et al. L1-medial skeleton of point cloud. *ACM Trans Graph.* 2013;32(4):65:61-65:68.

121. Crespo AJ, Domínguez JM, Rogers BD, et al. DualSPHysics: Open-source parallel CFD solver based on Smoothed Particle Hydrodynamics (SPH). *Computer Physics Communications.* 2015;187:204-216.

122. Lind S, Stansby P, Rogers B, Lloyd P. Numerical predictions of water–air wave slam using incompressible–compressible smoothed particle hydrodynamics. *Applied Ocean Research.* 2015;49:57-71.

123. Caballero A, Mao W, Liang L, et al. Modeling left ventricular blood flow using smoothed particle hydrodynamics. *Cardiovascular engineering and technology.* 2017;8(4):465-479.

124. Mittleman FBJ, Silva HRC, Taubin G. The ball-pivoting algorithm for surface reconstruction. *IEEE Transactions on Visualization and Computer Graphics.* 1999;5(4).

125. Guennebaud G, Gross M. Algebraic point set surfaces. In: *ACM SIGGRAPH 2007 papers.*2007:23-es.

126. Fang Q, Boas DA. Tetrahedral mesh generation from volumetric binary and grayscale images. Paper presented at: 2009 IEEE International Symposium on Biomedical Imaging: From Nano to Macro2009.

127. Fabri A, Pion S. CGAL: The computational geometry algorithms library. Paper presented at: Proceedings of the 17th ACM SIGSPATIAL international conference on advances in geographic information systems2009.

128. Eslami P, Hartman EM, Albaghadai M, et al. Validation of Wall Shear Stress Assessment in Non-invasive Coronary CTA versus Invasive Imaging: A Patient-Specific Computational Study. *Annals of Biomedical Engineering.* 2021;49(4):1151-1168.

129. Nousias S, Zacharaki EI, Moustakas K. AVATREE: An open-source computational modelling framework modelling Anatomically Valid Airway TREE conformations. *PloS one.* 2020;15(4):e0230259.

130. Faizal W, Ghazali N, Khor C, et al. Computational fluid dynamics modelling of human upper airway: a review. *Computer methods and programs in biomedicine.* 2020:105627.

131. Molony D, Park J, Zhou L, et al. Bulk flow and near wall hemodynamics of the rabbit aortic arch and descending thoracic aorta: A 4D PC-MRI derived computational fluid dynamics study. *Journal of biomechanical engineering.* 2019;141(1).

132. Foteinos PA, Chrisochoides NP. High quality real-time image-to-mesh conversion for finite element simulations. *Journal of Parallel and Distributed Computing.* 2014;74(2):2123-2140.

133. Gerig G, Koller T, Székely G, Brechbühler C, Kübler O. Symbolic description of 3-D structures applied to cerebral vessel tree obtained from MR angiography volume data. Paper presented at: Biennial International Conference on Information Processing in Medical Imaging1993.

134. Ghaffari M, Tangen K, Alaraj A, Du X, Charbel FT, Linninger AA. Large-scale subject-specific cerebral arterial tree modeling using automated parametric mesh generation for blood flow simulation. *Computers in biology and medicine.* 2017;91:353-365.

135. Schumann C, Neugebauer M, Bade R, Preim B, Peitgen H-O. Implicit vessel surface reconstruction for visualization and CFD simulation. *International Journal of Computer Assisted Radiology and Surgery.* 2008;2(5):275-286.

136. Barthe L, Cani M-P. Implicit Blending Revisited.

137. Mohan V, Sundaramoorthi G, Tannenbaum A. Tubular surface segmentation for extracting anatomical structures from medical imagery. *IEEE transactions on medical imaging.* 2010;29(12):1945-1958.

138. Wang Y, Narayanaswamy A, Roysam B. Novel 4-D open-curve active contour and curve completion approach for automated tree structure extraction. Paper presented at: CVPR 20112011.

139. Vida J, Martin RR, Varady T. A survey of blending methods that use parametric surfaces. *Computer-Aided Design.* 1994;26(5):341-365.

140. Xu G, Zhang Q. G2 surface modeling using minimal mean-curvature-variation flow. *Computer-Aided Design.* 2007;39(5):342-351.

141. Yuan X, Hongfan J, Yu W. A neural network approach to surface blending based on digitized points. *Journal of Materials Processing Technology.* 2002;120(1-3):76-79.

142. Barrecheguren M, Miravitlles M. COPD heterogeneity: implications for management. In. Vol 11: BioMed Central; 2016:1-2.

143. Valipour A, Shah PL, Gesierich W, et al. Patterns of emphysema heterogeneity. *Respiration.* 2015;90(5):402-411.

144. Labaki WW, Martinez CH, Martinez FJ, et al. The role of chest computed tomography in the evaluation and management of the patient with chronic obstructive pulmonary disease. *American journal of respiratory and critical care medicine.* 2017;196(11):1372-1379.

145. Ju J, Li R, Gu S, et al. Impact of emphysema heterogeneity on pulmonary function. *PLOS one.* 2014;9(11):e113320.

146. Cooper J, Trulock E, Triantafillou A, et al. Bilateral pneumectomy (volume reduction) for chronic obstructive pulmonary disease. *The Journal of Thoracic and Cardiovascular Surgery.* 1995;109(1):106-119.

147. Weinmann GG, Hyatt R. Evaluation and research in lung volume reduction surgery. *American journal of respiratory and critical care medicine.* 1996;154(6):1913-1918.

148. Shah PL, Herth FJ, van Geffen WH, Deslee G, Slebos D-J. Lung volume reduction for emphysema. *The Lancet Respiratory Medicine.* 2017;5(2):147-156.

149. DeCamp Jr MM, McKenna Jr RJ, Deschamps CC, Krasna MJ. Lung volume reduction surgery: technique, operative mortality, and morbidity. *Proceedings of the American Thoracic Society.* 2008;5(4):442-446.

150. Criner GJ, Sue R, Wright S, et al. A multicenter randomized controlled trial of Zephyr endobronchial valve treatment in heterogeneous emphysema (LIBERATE). *American journal of respiratory and critical care medicine.* 2018;198(9):1151-1164.

151. Labarca G, Uribe JP, Pacheco C, et al. Bronchoscopic lung volume reduction with endobronchial zephyr valves for severe emphysema: a systematic review and meta-analysis. *Respiration.* 2019;98(3):268-278.

152. Weinmann GG, Chiang Y-P, Sheingold S. The National Emphysema Treatment Trial (NETT) A Study in Agency Collaboration. *Proceedings of the American Thoracic Society.* 2008;5(4):381-384.

153. Davey C, Zoumot Z, Jordan S, et al. Bronchoscopic lung volume reduction with endobronchial valves for patients with heterogeneous emphysema and intact interlobar fissures (the BeLieVeR-HIFi study): a randomised controlled trial. *The Lancet.* 2015;386(9998):1066-1073.

154. Kemp SV, Slebos D-J, Kirk A, et al. A multicenter randomized controlled trial of Zephyr endobronchial valve treatment in heterogeneous emphysema (TRANSFORM). *American journal of respiratory and critical care medicine.* 2017;196(12):1535-1543.

155. Dooms C, Blondeel A, Ceulemans LJ, et al. Lung volume reduction in emphysema: a pragmatic prospective cohort study. *ERJ open research.* 2021;7(2).

156. Vinogradskiy Y. CT-based ventilation imaging in radiation oncology. *BJR| Open.* 2019;1(xxxx):20180035.

157. Porra L, Degrugilliers L, Broche L, et al. Quantitative imaging of regional aerosol deposition, lung ventilation and morphology by synchrotron radiation CT. *Scientific Reports.* 2018;8(1):1-10.

158. Bailey DL, Roach PJ. A brief history of lung ventilation and perfusion imaging over the 50-year tenure of the editors of Seminars in Nuclear Medicine. Paper presented at: Seminars in Nuclear Medicine2020.

159. Wechalekar K, Garner J, Gregg S. Pre-surgical evaluation of lung function. Paper presented at: Seminars in nuclear medicine2019.

160. Guerrero T, Sanders K, Noyola-Martinez J, et al. Quantification of regional ventilation from treatment planning CT. *International Journal of Radiation Oncology* Biology* Physics.* 2005;62(3):630-634.

161. Eslick EM, Bailey DL, Harris B, et al. Measurement of preoperative lobar lung function with computed tomography ventilation imaging: progress towards rapid stratification of lung cancer lobectomy patients with abnormal lung function. *European journal of cardio-thoracic surgery.* 2016;49(4):1075-1082.

162. Kipritidis J, Tahir BA, Cazoulat G, et al. The VAMPIRE challenge: a multi-institutional validation study of CT ventilation imaging. *Medical physics.* 2019;46(3):1198-1217.

163. Watkins WT, Li R, Lewis J, et al. Patient-specific motion artifacts in 4DCT. *Medical physics.* 2010;37(6Part1):2855-2861.

164. Doel T, Matin TN, Gleeson FV, Gavaghan DJ, Grau V. Pulmonary lobe segmentation from CT images using fissureness, airways, vessels and multilevel B-splines. Paper presented at: 2012 9th IEEE International Symposium on Biomedical Imaging (ISBI)2012.

165. Castillo E, Castillo R, Vinogradskiy Y, et al. Robust CT ventilation from the integral formulation of the Jacobian. *Medical physics.* 2019;46(5):2115-2125.

166. Castillo E, Castillo R, Vinogradskiy Y, Guerrero T. The numerical stability of transformation-based CT ventilation. *International journal of computer assisted radiology and surgery.* 2017;12(4):569-580.

167. Vaz S, Falkmer T, Passmore AE, Parsons R, Andreou P. The case for using the repeatability coefficient when calculating test–retest reliability. *PloS one.* 2013;8(9):e73990.

168. Scharm SC, Vogel-Claussen J, Schaefer-Prokop C, et al. Quantification of dual-energy CT-derived functional parameters as potential imaging markers for progression of idiopathic pulmonary fibrosis. *European Radiology.* 2021;31(9):6640-6651.

169. Feng A, Shao Y, Wang H, et al. A novel lung-avoidance planning strategy based on 4DCT ventilation imaging and CT density characteristics for stage III non-small-cell lung cancer patients. *Strahlentherapie und Onkologie.* 2021;197(12):1084-1092.

170. Hasse K, O'Connell D, Min Y, Neylon J, Low DA, Santhanam A. Estimation and validation of patient-specific high-resolution lung elasticity derived from 4DCT. *Medical physics.* 2018;45(2):666-677.

171. Stiehl B, Lauria M, O'Connell D, et al. A quantitative analysis of biomechanical lung model consistency using 5DCT datasets. *Medical physics.* 2020;47(11):5555-5567.

172. Hasse K, Neylon J, Min Y, et al. Feasibility of deriving a novel imaging biomarker based on patient-specific lung elasticity for characterizing the degree of COPD in lung SBRT patients. *The British journal of radiology.* 2019;92(1094):20180296.

173. Boes JL, Hoff BA, Bule M, et al. Parametric response mapping monitors temporal changes on lung CT scans in the subpopulations and intermediate outcome measures in COPD Study (SPIROMICS). *Academic radiology.* 2015;22(2):186-194.

174. Pompe E, van Rikxoort EM, Schmidt M, et al. Parametric response mapping adds value to current computed tomography biomarkers in diagnosing chronic obstructive pulmonary disease. *American journal of respiratory and critical care medicine.* 2015;191(9):1084-1086.

175. Matsuoka S, Yamashiro T, Washko GR, Kurihara Y, Nakajima Y, Hatabu H. Quantitative CT assessment of chronic obstructive pulmonary disease. *Radiographics.* 2010;30(1):55-66.

176. Labaki WW, Gu T, Murray S, et al. Voxel-wise longitudinal parametric response mapping analysis of chest computed tomography in smokers. *Academic radiology.* 2019;26(2):217-223.

177. Russi E, Bloch K, Weder W. Functional and morphological heterogeneity of emphysema and its implication for selection of patients for lung volume reduction surgery. *European Respiratory Journal.* 1999;14(1):230-236.

178. Slebos D-J, Klooster K, Ernst A, Herth FJ, Kerstjens HA. Bronchoscopic lung volume reduction coil treatment of patients with severe heterogeneous emphysema. *Chest.* 2012;142(3):574-582.

179. Faught AM, Miyasaka Y, Kadoya N, et al. Evaluating the toxicity reduction with computed tomographic ventilation functional avoidance radiation therapy. *International Journal of Radiation Oncology* Biology* Physics.* 2017;99(2):325-333.

180. Vinogradskiy Y, Rusthoven CG, Schubert L, et al. Interim analysis of a two-institution, prospective clinical trial of 4DCT-ventilation-based functional avoidance radiation therapy. *International Journal of Radiation Oncology* Biology* Physics.* 2018;102(4):1357-1365.

181. Abadi E, Sanders J, Samei E. Patient-specific quantification of image quality: an automated technique for measuring the distribution of organ Hounsfield units in clinical chest CT images. *Medical physics.* 2017;44(9):4736-4746.

182. Santhanam AP, Stiehl B, Lauria M, et al. An adversarial machine learning framework and biomechanical model-guided approach for computing 3D lung tissue elasticity from end-expiration 3DCT. *Medical Physics.* 2021;48(2):667-675.

183. Stiehl B, Lauria M, Singhrao K, et al. Scalable quorum-based deep neural networks with adversarial learning for automated lung lobe segmentation in fast helical free-breathing CTs. *International Journal of Computer Assisted Radiology and Surgery.* 2021:1-10.

184. O'Connell D, Ruan D, Thomas D, et al. A prospective gating method to acquire a diverse set of free-breathing CT images for model-based 4DCT. *Physics in Medicine & Biology.* 2018;63(4):04NT03.

185. Kubo T, Lin P-JP, Stiller W, et al. Radiation dose reduction in chest CT: a review. *American journal of roentgenology.* 2008;190(2):335-343.

186. Hasse K, Hsieh SS, O'Connell D, et al. Systematic feasibility analysis of performing elastography using reduced dose CT lung image pairs. *Medical Physics.* 2020.

187. Balakrishnan G, Zhao A, Sabuncu MR, Guttag J, Dalca AV. VoxelMorph: a learning framework for deformable medical image registration. *IEEE transactions on medical imaging.* 2019;38(8):1788-1800.

188. Westcott A, Capaldi DP, McCormack DG, Ward AD, Fenster A, Parraga G. Chronic obstructive pulmonary disease: thoracic CT texture analysis and machine learning to predict pulmonary ventilation. *Radiology.* 2019;293(3):676-684.

189. Zhang S, Li X, Zong M, Zhu X, Cheng D. Learning k for knn classification. *ACM Transactions on Intelligent Systems and Technology (TIST).* 2017;8(3):1-19.